

PROCEEDINGS

OF 14TH INTERNATIONAL CONFERENCE ON
COMMUNICATIONS, ELECTROMAGNETICS AND MEDICAL
APPLICATIONS (CEMA'19)



Organized by:



FACULTY OF TELECOMMUNICATIONS
TECHNICAL UNIVERSITY OF SOFIA, BULGARIA

NATIONAL TECHNICAL UNIVERSITY OF ATHENS, GREECE,
SCHOOL OF ELECTRICAL AND COMPUTER ENGINEERING

NATIONAL TECHNICAL
UNIVERSITY OF ATHENS,
GREECE



SCHOOL OF ELECTRICAL
AND COMPUTER
ENGINEERING

Sofia, Bulgaria
17th - 19th October, 2019

KING 2001, Sofia

Edited by Prof. Dr. Eng. **Dimiter Tz. Dimitrov**

All rights reserved. This book, or parts there of, may not be reproduced in any form or by any means, electronic or mechanical, including photocopying or any information storage and the retrieval system now known or to be invented without written permission from the Publisher.

ISSN: 1314-2100

SCOPUS Indexing

<http://suggestor.step.scopus.com/progressTracker>, ID: 6B4F77263D276412.

Printed in Bulgaria
KING 2001, Sofia



P. Frangos



D. Dimitrov



K. Dimitrov

Dear Colleagues,

It is our privilege to thank all of you for your contributions submitted at 14th regular International Conference on 'Communication, Electromagnetic and Medical Applications' CEMA'19. This is a conference which should help future collaboration in the area of engineering, especially in the area of communication technologies and medical applications. This is an important scientific event not only in Balkan region, but in Europe, also. The International Conference on Communication, Electromagnetism and Medical Applications CEMA'19 is dedicated to all essential aspects of the development of global information and communication technologies, and their impact in medicine, as well. The objective of Conference is to bring together lecturers, researchers and practitioners from different countries, working on the field of communication, electromagnetism, medical applications and computer simulation of electromagnetic field, in order to exchange information and bring new contribution to this important field of engineering design and application in medicine. The Conference will bring you the latest ideas and development of the tools for the above mentioned scientific areas directly from their inventors. The objective of the Conference is also to bring together the academic community, researchers and practitioners working in the field of Communication, Electromagnetic and Medical Applications, not only from all over Europe, but also from America and Asia, in order to exchange information and present new scientific and technical contributions.

Many well known scientists took part in conference preparation as members of International Scientific Committee or/and as reviewers of submitted papers. We would like to thank all of them for their efforts, for their suggestions and advices.

On behalf of the International Scientific Committee, we would like to wish you successful presentations of your papers, successful discussions and new collaborations for your future scientific investigations.

Engineering and medicine should provide high level of living for all people.

D. Dimitrov
Conference Chairman

P. Frangos
Conference Vice Chairman

K. Dimitrov
Conference Vice Chairman

INTERNATIONAL SCIENTIFIC COMMITTEE

Chairman:

D. TZ. DIMITROV, Technical University of Sofia, Bulgaria

Vice Chairmen:

P. FRANGOS, National Technical University of Athens, Greece

K. L. DIMITROV, Technical University of Sofia, Bulgaria

Members

N. AMPILOVA,	University of Petersburg, Russia
T. AVOYAGI,	Tokyo Institute of Technology, Japan
A. BEKJARSKY,	Technical University of Sofia, Bulgaria
E. BOEMO,	University Autonomoma, Barcelona, Spain
R. BRUZGIENE,	Kaunas University of Technology, Lithuania
N. DIB,	Jordan University of Science and Technology, Aman, Jordan
V. DUMBRAVA,	Kaunas University of Technology, Litvania
N. ESCUDEIRO,	ISEP, Porto, Portugal
E. GAGO-RIBAS,	University of Oviedo, Spain
V. GEORGIEVA,	Technical University of Sofia, Bulgaria
G. GOUSSETIS,	Heriot - Watt University, United Kingdom
S. V.HOEYE,	University of Oviedo, Spain
I. ILIEV,	Technical University of Sofia, Bulgaria
F. KLETT,	Franhofer Institute, Ilmenau, Germany
G. KLIROS,	Hellenic Air-Force Academy, Athens, Greece
V. KUKENSKA,	Technical University of Gabrovo, Bulgaria
L. LUBIH,	Technical University of Sofia, Bulgaria
G. MALLET,	University "Sophia Antipolis", Nice, France
G. MATSOPOULOS,	National Technical University of Athens, Greece
M. MARTINS,	Academia Militar da Amadora, DCEE, Portugal
M.- J. MORALES-GONZALES,	University of Valladolid, Spain
L. NARBUTAITE,	Kaunas University of Technology, Lithuania
K. NIKITA,	National Technical University of Athens, Greece
M. NIKOLOVA,	High Naval School, Varna, Bulgaria
A. PANAGOPOULOS,	National Technical University of Athens, Greece
J. PETROVSKA,	Medical University of Sofia, Bulgaria
H. ROTH,	University of Siegen, Germany
S. SAUTBEKOV,	Euroasian University, Astana, Kazakhstan
A. SAVOV,	Medical University of Sofia, Bulgaria
S. SAVOV,	Technical University of Varna, Bulgaria
H.-P. SCHADE,	Technical University of Ilmenau, Germany
I. SOLOVIEV,	University of St. Petersburg, Russia
L. SONG,	Technical University of Harbin, China
G. STAMATAKOS,	National Technical University of Athens, Greece
A. USHEVA,	University of Boston, USA
R. VERDONE,	University of Bologna, Italy

REVIEWERS

BALZANO, Q.	University of Maryland, USA
BEHARI, J.	Jawaharlal Nehru University ,New Delhi, India
BOEMO, E.	Technical University of Madrid, Spain
DIMITROV, D.	Technical University of Sofia, Bulgaria
DONTSHEWA, M.	University of Applied Sciences, Dornbirn, Austria
GOUSSETIS, G.	Heriot - Watt University, United Kingdom
MALLET, G.	University "Sophia Antipolis", Nice, France
PETROVSKA, J.	Medical University of Sofia, Bulgaria
PRATO, F.	University of Western Ontario, Canada
ROTH, H.	University of Siegen, Germany
SAVOV, A.	Medical University of Sofia, Bulgaria
SCHADE, H-P.	Technical University of Ilmenau, Germany
SONG, L.	Technical University of Harbin, China
USHEVA, A.	University of Boston, USA

REGISTRATION

October, 17th, 09h 30min - 16h

The conference registration desk will be at:
Building of Library, fourth floor
Technical University of Sofia, Bulgaria

CONFERENCE PROGRAM

17th October

OPENING CEREMONY

10h - 10h 30min

The conference registration desk will be at:
Building of Library, fourth floor
Technical University of Sofia, Bulgaria

SCIENTIFIC PROGRAM

17th October

FIRST SESSION

10h 30min - 12h

Building of Library, fourth floor
Technical University of Sofia, Bulgaria

*Chairman: Prof. P. Frangos, School of Electrical and Computing Engineering,
National Technical University of Athens, Greece*

1. FREQUENCY DEPENDENCY OF MULTIPATH FADING OVER THE SEA UNDER DUCTING. PART I: SIMULATION RESULTS FOR REFRACTIVITY PROFILES' PARAMETERS INFLUENCE

Irina SIRKOVA, Laser Radars Lab, Institute of electronics, Bulgarian Academy of Sciences, Bulgaria

2. FREQUENCY DEPENDENCY OF MULTIPATH FADING OVER THE SEA UNDER DUCTING. PART II: SIMULATION RESULTS FOR SEA SURFACE ROUGHNESS INFLUENCE

Irina SIRKOVA, Laser Radars Lab, Institute of electronics, Bulgarian Academy of Sciences, Bulgaria

3. IMPROVING THE PERFORMANCE OF TURBULENT FREE SPACE OPTICAL LINK BY USING A FOURIER FILTER

Jassim Mohammed Jassim, R. N. Ali, A. B. Sharba, Mariam Kadhim Jawad, and Khalid Mahdi Jasim, College of Science for Women/Laser Physics Depart./University of Babylon/Iraq

4. METHODOLOGY AND ARCHITECTURE OF A COMPUTER-BASED INTERACTIVE TIMING SYSTEM FOR APPLICATIONS IN MEDICINE

Maria Angelova, Technical University – Sofia, Kalin Dimitrov, Technical University – Sofia, Stefan Valyukov, Therapist, Bulgaria

5. INNOVATIVE BIOMONITORING SYSTEMS IN THE AEROSPACE INDUSTRY

Evgeni Andreev, Veselka Radeva, Mariya Nikolova, "N. Y. Vaptsarov" Naval Academy, Varna, Bulgaria

6. X-RAY IMAGE PROCESSING FOR TISSUE INVOLVEMENT-BASED CARIES DETECTION

Veska Georgieva, Technical University of Sofia, Bulgaria, Plamen Petrov, Technical University of Sofia, Bulgaria, Barna Iantovics, University of Medicine, Pharmacy, Sciences and Technology, of Targu Mures, Romania

Lunch

12h - 13h30min

SECOND SESSION

13h 30min - 15h

Building of Library, fourth floor
Technical University of Sofia, Bulgaria

Chairman: Prof. V. Georgieva, Faculty of Telecommunication, Technical University of Sofia, Bulgaria

1. SEA STATE DETERMINATION USING NORMALIZED EXPERIMENTAL ONE - DIMENSIONAL RADAR SIGNATURES AT X - BAND AND FRACTAL TECHNIQUES

G. Pouraimis, A. Kotopoulis*, N. Ampilova**, I. Soloviev**, E. Kallitsis* and P. Frangos*, School of Electrical and Computing Engineering, National Technical University of Athens, Greece* Computer Science Department, St. Petersburg State University, Russia***

2. ON THE APPLICATION OF MULTIFRACTAL METHODS FOR THE ANALYSIS OF SEA SURFACE IMAGES RELATED TO SEA STATE DETERMINATION

N. Ampilova, I. Soloviev*, Apostolos Kotopoulis**, George Pouraimis**, Panayiotis Frangos**, Computer Science Department, St. Petersburg State University, Russia*, School of Electrical and Computer Engineering, National Technical University of Athens, Greece***

3. ANALYSIS OF IMAGES OBTAINED BY CAPILLARY DYNAMOLYSIS METHOD

I. Murenin, N. Ampilova, Computer Science Department, St. Petersburg State University, Russia

4. MODELING OF THE DYNAMICS OF CHANGED PARTICLES USING UNITY ENGINE

M. Syasko, I. Soloviev, Computer Science Department, St. Petersburg State University, Russia

5. IMPROVED ALGORITHM FOR CALCULATING GEOMETRIC CHARACTERISTICS FROM OPTICAL IMAGES CORRODED OBJECT'S CROSS-SECTION

Borislav Bonev, Anna Stoyanova*, Antonio Shopov**, Department of Microelectronics*, Department of Strength of materials**, Technical University of Sofia*

6. WILD ANIMALS POPULATION ESTIMATION FROM THERMOGRAPHIC VIDEOS USING TENSOR DECOMPOSITION

Ivo Draganov, Rumen Mironov, Nikolay Neshov, Agata Manolova, Radiocommunications and Videotechnologies Dept., Faculty of Telecommunications, Technical University of Sofia

Break

15h – 15h 30min

THIRD SESSION

15h 30min – 17h

Building of Library, fourth floor
Technical University of Sofia, Bulgaria

Chairman: Prof. N. Ampilova, St. Petersburg State University, St. Petersburg, Russia

1. SIGNAL PROCESSING AND STORING OF HIGH DYNAMIC RANGE ACOUSTIC DATA FOR KNOWLEDGE DISCOVERY

I. Simeonov, T. Trifonov*, T. Georgieva-Trifonova**, Vasil Levski National Military University, Veliko Tarnovo, Bulgaria*, Cyril and St. Methodius University of Veliko Tarnovo, Faculty of Mathematics and Informatics, Veliko Tarnovo, Bulgaria***

2. AN EXPERIMENTAL STUDY OF IMPROVING SOUND INSULATION INDEX OF HOLLOW BRICK WALL BY USING WALL LINING PANELS FOR ACOUSTIC SENSITIVE ROOMS IN HOSPITAL

Snezhana Pleshkova, Aleksandar Vasilev Kirechev, Faculty of Telecommunications, Technical University of Sofia, Bulgaria

3. COMPARISON BETWEEN APPLICATION OF GIRDLE COIL AND SEVERAL LOCAL INDUCTORS IN MAGNETOTHERAPY

Dimitar Dimitrov, Faculty of Telecommunications, Technical University of Sofia, Bulgaria

4. SOME POSSIBILITIES FOR OPTIMISATION OF APPLICATION OF GIRDLE COIL IN MAGNETOTHERAPY

Sasho Guergov, Atanas Dimitrov, Technical University of Sofia, Bulgaria

5. ONE APPLICATION OF INFLUENCE OF LOW FREQUENCY MAGNETIC FIELD ON THE HEAD

Atanas Dimitrov, Sasho Guergov, Technical University of Sofia, Bulgaria

CLOSING CONFERENCE SESSIONS

17h – 17h 30min

Building of Library, fourth floor
Technical University of Sofia, Bulgaria

SOCIAL PROGRAM

- **Conference Dinner**, 19h, October, 17th
- **Trip**, October, 18th.

More information regarding Conference dinner and trip will be provided during the first day of the Conference (October 17th)

CONTACT US:

<http://rcvt.tu-sofia.bg/CEMA/eth.html>

Prof. Dr. Dimiter Dimitrov

Faculty of Telecommunication
Technical University of Sofia
8, Kliment Ohridsky str.
1756 Sofia, Bulgaria
Phone: ++359 2 9652278
Fax: ++359 2 9652278
E-mail: dcd@tu-sofia.bg

Prof. P. Frangos

National Technical University of Athens
School of Electrical and Computer Engineering
9, Iroon Polytechniou Str. ,
157 73 Zografou, Athens, Greece
Phone : 00 30 210 772 3694
Fax : 00 30 210 772 2281
E-mail: pfrangos@central.ntua.gr

TABLE OF CONTENTS

1. FREQUENCY DEPENDENCY OF MULTIPATH FADING OVER THE SEA UNDER DUCTING. PART I: SIMULATION RESULTS FOR REFRACTIVITY PROFILES' PARAMETERS INFLUENCE	1
<i>Irina Sirkova</i>	
2. FREQUENCY DEPENDENCY OF MULTIPATH FADING OVER THE SEA UNDER DUCTING. PART II: SIMULATION RESULTS FOR SEA SURFACE ROUGHNESS INFLUENCE	6
<i>Irina Sirkova</i>	
3. IMPROVING THE PERFORMANCE OF TURBULENT FREE SPACE OPTICAL LINK BY USING A FOURIER FILTER.....	10
<i>Jassim Mohammed Jassim, R. N. Ali, A. B. Sharba, Mariam Kadhim Jawad, Khalid Mahdi Jasim</i>	
4. METHODOLOGY AND ARCHITECTURE OF A COMPUTER-BASED INTERACTIVE TIMING SYSTEM FOR APPLICATIONS IN MEDICINE.....	14
<i>Maria Angelova, Kalin Dimitrov, Stefan Valyukov</i>	
5. INNOVATIVE BIOMONITORING SYSTEMS IN THE AEROSPACE INDUSTRY	17
<i>Evgeni Andreev, Veselka Radeva, Mariya Nikolova</i>	
6. X-RAY IMAGE PROCESSING FOR TISSUE INVOLVEMENT-BASED CARIES DETECTION	22
<i>Veska Georgieva, Plamen Petrov, Barna Iantovics</i>	
7. SEA STATE DETERMINATION USING NORMALIZED EXPERIMENTAL ONE - DIMENSIONAL RADAR SIGNATURES AT X - BAND AND FRACTAL TECHNIQUES.....	27
<i>G. Pouraimis, A. Kotopoulis, N. Ampilova, I. Soloviev, E. Kallitsis, P. Frangos</i>	
8. ON THE APPLICATION OF MULTIFRACTAL METHODS FOR THE ANALYSIS OF SEA SURFACE IMAGES RELATED TO SEA STATE DETERMINATION.....	32
<i>N. Ampilova, I. Soloviev, Apostolos Kotopoulis, George Pouraimis, Panayiotis Frangos</i>	
9. ANALYSIS OF IMAGES OBTAINED BY CAPILLARY DYNAMOLYSIS METHOD	36
<i>I. Murenin, N. Ampilova</i>	
10. MODELING OF THE DYNAMICS OF CHANGED PARTICLES USING UNITY ENGINE.....	41
<i>M. Syasko, I. Soloviev</i>	

11. IMPROVED ALGORITHM FOR CALCULATING GEOMETRIC CHARACTERISTICS FROM OPTICAL IMAGES CORRODED OBJECT'S CROSS-SECTION	46
<i>Borislav Bonev, Anna Stoynova, Antonio Shopov</i>	
12. WILD ANIMALS POPULATION ESTIMATION FROM THERMOGRAPHIC VIDEOS USING TENSOR DECOMPOSITION	52
<i>Ivo Draganov, Rumen Mironov, Nikolay Neshov, Agata Manolova</i>	
13. SIGNAL PROCESSING AND STORING OF HIGH DYNAMIC RANGE ACOUSTIC DATA FOR KNOWLEDGE DISCOVERY	58
<i>I. Simeonov, T. Trifonov, T. Georgieva-Trifonova</i>	
14. AN EXPERIMENTAL STUDY OF IMPROVING SOUND INSULATION INDEX OF HOLLOW BRICK WALL BY USING WALL LINING PANELS FOR ACOUSTIC SENSITIVE ROOMS IN HOSPITAL.....	63
<i>Snezhana Pleshkova, Aleksandar Vasilev Kirechev</i>	
15. COMPARISON BETWEEN APPLICATION OF GIRDLE COIL AND SEVERAL LOCAL INDUCTORS IN MAGNETOTTEHRAPY.....	68
<i>Dimitar Dimitrov</i>	
16. SOME POSSIBILITIES FOR OPTIMISATION OF APPLICATION OF GIRDLE COIL IN MAGNETOTHERAPY	72
<i>Sasho Guergov, Atanas Dimitrov</i>	
17. ONE APPLICATION OF INFLUENCE OF LOW FREQUENCY MAGNETIC FIELD ON THE HEAD	76
<i>Atanas Dimitrov, Sasho Guergov</i>	

FREQUENCY DEPENDENCY OF MULTIPATH FADING OVER THE SEA UNDER DUCTING

Part I: SIMULATION RESULTS FOR REFRACTIVITY PROFILES' PARAMETERS INFLUENCE

Irina SIRKOVA

Laser Radars Lab, Institute of electronics
Bulgarian Academy of Sciences, Tzarigradsko chaussee 72, 1784 Sofia, Bulgaria

irina@ie.bas.bg

Abstract

Over water microwave propagation is often affected by the presence of evaporation duct. The tropospheric ducting is one of the major causes for multipath propagation. The ducting propagation mechanism is known to be highly frequency dependent whereas the prediction methods for multipath fading distribution suggest a rather slight dependence on frequency. In order to check this discrepancy, Part I of this work deals with the influence of the variations of important parameters of the evaporation duct log-linear refractivity profile on the frequency dependency of multipath fading. The refractivity profiles serve as input to the parabolic equation method which provides a full-wave solution to the path loss problem. Ten frequencies of microwave range are used in four hypothetical over the sea links. The results are presented in form of path loss standard deviation versus frequencies for fixed ranges.

1. INTRODUCTION

The propagation conditions in coastal and maritime regions are often complicated by changes in the tropospheric refractive index leading to formation of tropospheric ducts [1]. This peculiarity makes the preliminary assessment of microwave propagation in those regions difficult and subject to significant errors [2]. One of the consequences of the ducts' formation is the multipath propagation and, accordingly, the multipath fading [3]. The assessment of fading is an important part of performance predicting of radio communication links. To achieve the necessary accuracy in performance predicting, sophisticated propagation channel modelling methods are applied which account simultaneously for terrain irregularities, clear air propagation mechanisms, and antenna patterns. Among them the Parabolic Equation (PE) method [4] has become one of the most widely used to solve microwave propagation problems especially in complicated environments such as tropospheric ducting [4, 5]. Despite the variability of the marine boundary layer [6], for practical purposes one usually assumes lateral homogeneity for the refractivity and applies a single profile, approximated to account for the average behaviour of the modified refractivity $M(z)$ with height z , as environmental input to the PE. Special attention is paid to the modelling of $M(z)$ for evaporation duct due to its frequent occurrence and par-

ticular importance in coastal and maritime regions. Most often the evaporation duct is modelled by log-linear height profile of the modified refractivity M [7]:

$$M(z) = M_0 + c_0 \left[z - z_d \ln \left(\frac{z + z_0}{z_0} \right) \right], \quad (1)$$

where $M_0 = M(z = 0)$, z_0 is the aerodynamic roughness parameter usually taken to be 1.5×10^{-4} m [4], z_d is the duct height corresponding to the height at which $dM/dz = 0$, c_0 is the critical potential refractivity gradient [8] usually taken to be 0.13. The physics behind this profile, based on the Monin–Obukhov similarity theory, is explained in [4, 7]. With above values of parameters c_0 and z_0 , (1) has been obtained assuming thermally neutral troposphere stratification and does not account for the stability effects on the M profile. This most usual form of evaporation duct log-linear M profile is governed by one parameter - the duct height, z_d , which determines the other important duct parameter, the M -deficit, $\Delta M = M(z_d) - M_0$. Recently attempts at improving (1) have been made by changing the slope in different parts of the log-linear curve [8, 9], thus making it to better fit the experimental profiles and, hence, include the influence of tropospheric stability. In [8] the parameters of evaporation duct refractivity model (1) have been optimized using radio-sonde data. This study has shown that the best log-

linear model formulation would include, except for the most important duct parameter z_d , also duct curvature and mixed layer slope (mixed layer is the well-mixed by turbulent mixing layer above the duct). In (1) c_0 and z_0 are parameters responsible for the profile curvature (c_0 changes the radius of curvature surrounding the duct whereas z_0 changes the curvature below the duct only [8]). Those parameters influence also the M -deficit under the same z_d .

The ducting propagation mechanism is highly frequency dependent whereas the prediction methods for multipath fading distribution on line-of-sight links suggest a rather slight dependence on frequency [10, 11]. In order to check this discrepancy, this work studies how the parameters of profile (1) reflect on the frequency dependency of (large-scale) multipath fading in the case of microwave propagation over the sea under evaporation duct conditions. The evaporation duct model (1), with varying parameters z_d and c_0 , serves as input to the PE method [4] to compute the path loss' standard deviation in the areas of interests. Ten frequencies of microwave range are used in four hypothetical over the sea line-of-site links.

2. DESCRIPTION OF THE METHOD

The PE method is applied as implemented in "Advanced propagation model (APM) Computer software configuration item (CSCI) documents", Space and Naval Warfare Systems Center Tech. Doc. 3145, San Diego, CA, 2002. Those routines make use essentially of the 2D narrow-angle forward-scatter scalar PE, (2), which provides a full-wave solution to the path loss problem:

$$\frac{\partial u(x, z)}{\partial x} = \frac{i}{2k} \frac{\partial^2 u(x, z)}{\partial z^2} + \frac{ik}{2} (m^2(x, z) - 1) u(x, z). \quad (2)$$

Details on the derivation of (2), its validation and use for electromagnetic (EM) field calculations under tropospheric ducting conditions are largely reported in the literature [4, 5] and will not be repeated here. In (2) k is the free-space wave number, $m = M \times 10^{-6} + 1$ is the modified refractive index, $u(x, z)$ is a slow-varying along the preferred propagation direction, x , function related to the corresponding to the polarization transverse EM field component, x and z stay for range and altitude. The popularity of (2) is related to its easy numerical solution through marching algorithms. In addition to boundary condi-

tions, (2) requires knowledge of initial field [4]. The drawback of (2) is the neglect of backscattering. The studied microwave propagation problem is characterized by EM field variations over scales much larger than the wavelength, grazing incident angles, and smooth variation of the tropospheric refractive index with x ; under these conditions the forward-propagated field plays dominant role and this assures the applicability of (2).

The initial field required to start the calculations is provided by horizontally polarized Gaussian beam source with pattern factor given by (3) where θ_0 and θ_s are the half power beamwidth and the antenna elevation angle. Smooth perfect conducting underlying surface (sea) is assumed. The results are presented in the form of standard deviation of the path loss (PL in dB, see (4)) in the area of interest versus frequency for fixed range.

$$F(\theta) = \exp \left[\frac{\ln(0.707)(\theta - \theta_s)^2}{\left(\frac{\theta_0}{2}\right)^2} \right], \quad (3)$$

$$PL = 20 \log \left(\frac{4\pi r}{\lambda} \right) - PF. \quad (4)$$

In (4) λ is the free-space wavelength, r is the distance between the corresponding points and PF is the pattern propagation factor defined as the square of the ratio of the electric field amplitude E received at a given point under specific conditions to the amplitude of the electric field E_0 received under free-space conditions with the beam of the transmit antenna directed toward this given point [4].

3. RESULTS AND DISCUSSION

For every frequency the PL is calculated versus height for fixed ranges $R = 20$ km, $R = 40$ km for four hypothetical links: A) $z_t = 40$ m, $\theta_0 = 5^\circ$; B) $z_t = 15$ m, $\theta_0 = 5^\circ$; C) $z_t = 40$ m, $\theta_0 = 1^\circ$; D) $z_t = 15$ m, $\theta_0 = 1^\circ$, where z_t stays for the transmitter height. Three different values for c_0 are used: $c_0 = 0.13$, $c_0 = 0.11$ and $c_0 = 0.19$, the last two accounting for the deviation from the thermally neutral troposphere stratification. For all cases $\theta_s = 0^\circ$ in (3). The parameter z_0 is kept equal to 1.5×10^{-4} m in all reported examples. The receiver height is supposed to start from $z_r = 5$ m and go up to 150 m. This area of interest is divided in two parts: z_1 from 5 m to the

top of evaporation layer, defined here as $z_L = 2z_d$, see [8], and z_2 which ranges from the evaporation layer height z_L up to 150 m. The frequencies are shown in Table 1. Those frequencies belong to the ranges used for coastal and maritime radars (lower ranges) and fixed and mobile links (upper ranges). The results are presented in form of *PL* standard deviation versus frequencies.

Table 1. Frequencies used, GHz

2.4	3.1	4.5	5.6	7.1	8.4	9.3	13.4	15.4	19.7
-----	-----	-----	-----	-----	-----	-----	------	------	------

Figure 1 shows range-independent duct with $z_d = 35 \text{ m} = ct$ over the entire distance of $R = 20 \text{ km}$ for link A and the two areas of interest, z_1 and z_2 .

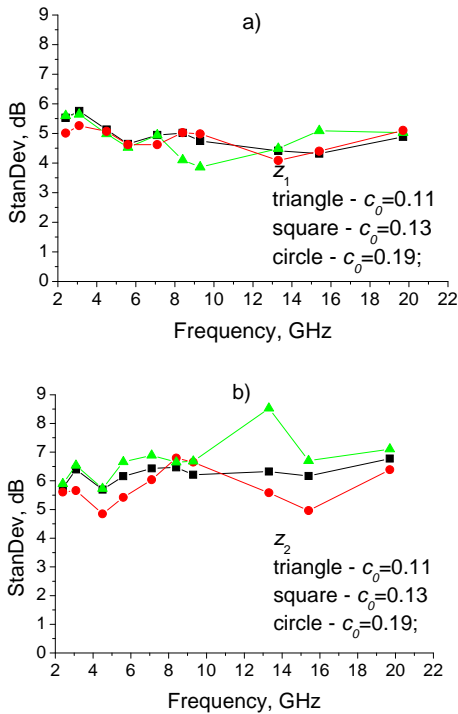


Figure 1. Range-independent duct: $z_d = 35 \text{ m}$, $R = 20 \text{ km}$, link A

Figure 2 reports similar results but for $z_d = 10 \text{ m} = ct$ and link B. On both figures one can see comparison for three different values of c_0 . On Fig. 3, which refers to link C, the *PL* standard deviation for $z_d = 35 \text{ m}$ duct is compared to standard troposphere conditions at distance $R = 40 \text{ km}$. As it is seen from Figs. 1-3, the frequency dependency of *PL* standard deviation is rather slight and has similar character for the three values of c_0 ; it is higher in area z_1 , especially for the lower frequencies, see Fig. 2a). This may be due to the fact that the lower frequencies are not well trapped in the thinner duct from Fig. 2. For the three Figs., both z_t and z_r are

submerged in the evaporation layer ($z_t, z_r < z_L$) which determines the more pronounced influence of the duct for area z_1 than for z_2 .

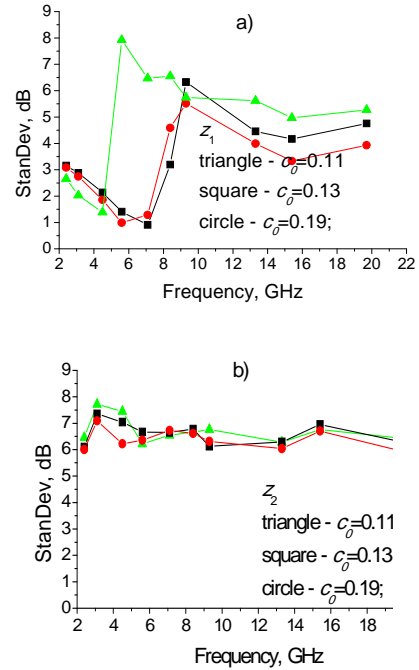


Figure 2. Range-independent duct: $z_d = 10 \text{ m}$, $R = 20 \text{ km}$, link B

Figure 3 differs from Fig. 1 through the greater distance ($R = 40 \text{ km}$) at which the *PL* is computed and the narrower antenna beam ($\theta_0 = 1^\circ$). The longer the distance, the higher the duct influence; on the other hand the larger antenna beam and shorter distance determine the predominant role of the reflections from the underlying surface - this could explain the "smoothed" frequency dependence on Fig. 3 compared to Fig. 1. All studied frequencies are well trapped and strongly guided in the "thick" duct on Fig. 3 which determines the lower scattering and, hence, the lower values of standard deviation for the ducting in area z_1 in comparison to standard troposphere case. As for z_2 on Fig. 3, in this area the slope of the *M* profile above z_L is (almost) the same for the duct and standard troposphere which determines closer values for standard deviation in both cases in z_2 .

The frequency dependency of standard deviation for range-dependent duct in sense that the start refractivity profile has $c_0 = 0.13$ which changes to $c_0 = 0.19$ at the mid path has also been studied; the results (not reported here) indicated (once again) the rather weak influence of the variation of c_0 (except for the lowest frequencies), especially in area z_2 .

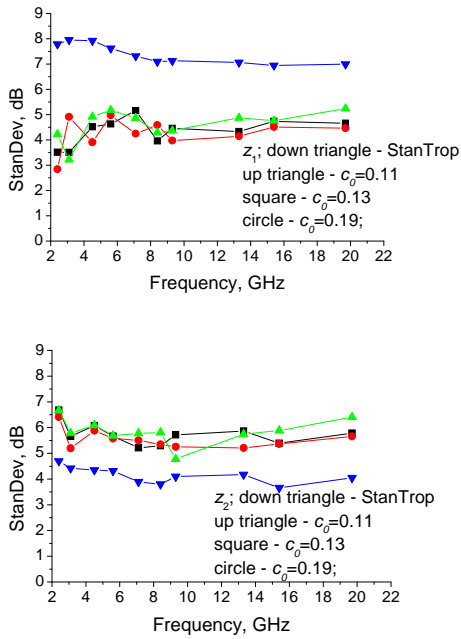


Figure 3. Range-independent duct: $z_d = 35$ m, $R=40$ km, link C

Further, on Fig. 4, another range-dependent case is demonstrated by changing the z_d parameter in the middle of the path from initial $z_d = 10$ m to $z_d = 15$ m, $c_0 = 0.19 = ct$, $R = 20$ km, link C. As expected, on Fig. 4 for the area z_1 the change in z_d almost does not reflect on the frequency dependency because z_t for link C is above evaporation layer z_L for both z_d values. The influence of increased z_d is higher in the area z_2 .

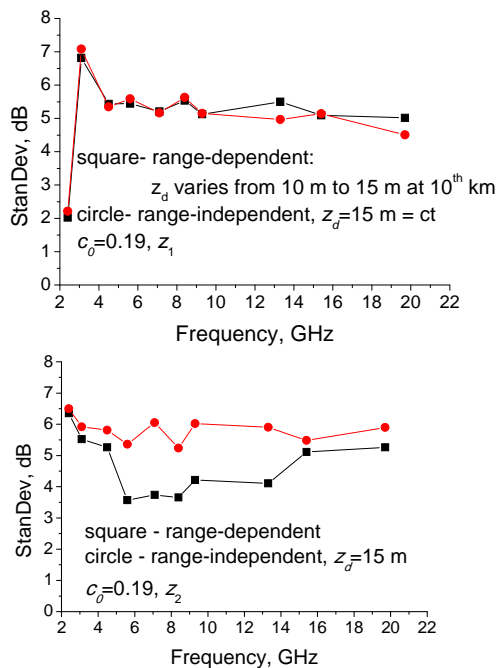


Figure 4. Comparison between range-dependent and range independent duct, $R = 20$ km, link C

4. CONCLUSION

On the basis of Figs. 1-4 the following concluding remarks may be drawn:

- in the studied limits, the results support the applicability of profile (1) with $c_0 = 0.13$;
- in general, the frequency dependency of multipath fading under ducting conditions modelled by (1) for smooth sea surface is rather slight and appears to be in accordance with the slight influence of the frequency dependent factor in widely applied prediction methods [2, 10, 11]. More attention is to be paid to lower frequencies when ducts with low z_d are present. The particular case when z_t is between z_d and evaporation layer z_L needs additional studies.

5. ACKNOWLEDGMENTS

This work was supported in part by the Ministry of Education and Science of Bulgaria under grant agreement № D01-151/2018.

REFERENCES

- [1] ITU-R P.453-9, "The Radio Refractive Index: its Formula & Refractivity Data", 2003.
- [2] R. L. Olsen and T. Tjelta, "Worldwide Techniques for Predicting the Multipath Fading Distribution on Terrestrial LOS Links: Background and Results of Tests", IEEE Trans, Vol. AP-47, No. 1, 1999, 157-170.
- [3] S. R. Saunders and A. Aragon-Zavala, Antennas and Propagation for Wireless Communication Systems, John Wiley & Sons, 2nd edition, 2007.
- [4] M. Levy, Parabolic Equation Methods for Electromagnetic Wave Propagation, IEE electromagnetic waves series 45, UK, 2000.
- [5] I. Sirkova, "Brief Review on PE Method Application to Propagation Channel Modeling in Sea Environment", CEJE, Vol. 2, No. 1, 2012, 19-38.
- [6] B. W. Atkinson and M. Zhu, "Coastal Effects on Radar Propagation in Atmospheric Ducting Conditions", Meteorological Applications, Vol. 13, 2006, 53-62.
- [7] R. A. Paulus, "Practical application of an evaporation duct model", Radio Sci., Vol. 20, 1985, 887-896.
- [8] J. T. Saeger, N. G. Grimes, H. E. Rickard, and E. E. Hackett, "Evaluation of Simplified Evaporation Duct Refractivity Models for Inversion Problems", Radio Sci., Vol. 50, No. 10, 2015, 1110-1130.
- [9] J.-P. Zhang, Z.-S. Wu, Q.-L. Zhu, and B. Wang, "A Four-Parameter M-profile Model for the Evaporation Duct Es-

timation from Radar Clutter", PIER, Vol. 114, 2011, 353-368.

[10] R.L. Olsen, T. Tjelta, L. Martin, and B. Segal, "World-wide Techniques for Predicting the Multipath Fading Distribution on Terrestrial LOS Links: Comparison with

Regional Techniques", IEEE Trans, Vol. AP-51, No. 1, 2003, 23-30.

[11] ITU-R P.530-9, "Propagation Data and Prediction Methods Required for the Design of Terrestrial Line-of-Sight Systems", 2001.

FREQUENCY DEPENDENCY OF MULTIPATH FADING OVER THE SEA UNDER DUCTING

Part II: SIMULATION RESULTS FOR SEA SURFACE ROUGHNESS INFLUENCE

Irina SIRKOVA

Laser Radars Lab, Institute of electronics
Bulgarian Academy of Sciences, Tzarigradsko chaussee 72, 1784 Sofia, Bulgaria

irina@ie.bas.bg

Abstract

The troposphere ducting and sea surface roughness make coastal and over water communication links among the most difficult to predict. Part I of this work studied the influence of evaporation duct log-linear modified refractivity profile parameters' variations on the frequency dependency of multipath fading assuming propagation over smooth sea. In Part II the influence of sea surface roughness is added to evaporation duct conditions. The sea surface roughness is modelled through two roughness reduction factors, one of them accounting for the shadowing. The same ten microwave frequencies and four hypothetical over the sea links as in Part I are used. The results are presented in form of path loss standard deviation versus frequencies for fixed ranges. The path loss is computed by the parabolic equation method.

1. INTRODUCTION

Anomalous propagation conditions due to tropospheric ducting are typical for coastal and maritime areas. They complicate the design and performance prediction of microwave radars and communications systems working in these areas [1]. The multipath fading is among the problems related to ducting propagation mechanism. The most common duct over large bodies of water is the evaporation duct. Part I of this work, [2], studied the influence of evaporation duct log-linear modified refractivity profile parameters' variations on the frequency dependency of multipath fading assuming propagation over smooth sea. Part II of this work combines the influence of sea surface roughness with the evaporation duct conditions as described in [2] in order to check whether a highly frequency dependent propagation mechanism as ducting may result in a rather slight dependence on frequency for multipath fading as suggested by some prediction methods [3, 4].

The correct modelling of electromagnetic propagation over rough sea surface is still an open issue due to the difficulties in implementing all scattering mechanisms in the electromagnetic model. A practical approximate solution is to account for the surface roughness effects by defining an "effective" reflection coefficient R_{eff} , see (1) in Section 2, representing the Fresnel reflection coefficient from flat

surface, R_F , multiplied by a roughness reduction factor (RRF) R_{rf} [5]. Two RRFs have been widely used in over-the-ocean microwave propagation: the Miller-Brown one [6] and Ament's RRF [7]. Comparisons of the propagation prediction results based on combination of these two RRFs with different propagation models to measurements' data do not allow concluding which of them is more accurate; a good discussion on this issue may be found in [8]. The propagation at very low grazing angles, typical for tropospheric ducting, is additionally complicated by shadowing effect due to sea surface waves [8, 9]. It is to be noted that both above mentioned RRFs affect only the magnitude of the complex Fresnel reflection coefficient and do not account for the shadowing. In order to go closer to the observed experimental results, theoretical efforts have been made to improve the RRF's accuracy by introducing the shadowing effect [8, 9].

In [2] the important parameters of evaporation duct log-linear modified refractivity profile have been briefly discussed and the parabolic equation (PE) method [5] used for path loss computation has been sketched out. For more information on those topics the reader is referred to [2] and the literature cited there. Part II makes use of the same ten frequencies of microwave range and four hypothetical over the sea line-of-site links as in [2]. On the basis of the "effective" reflection coefficient concept, the sea

surface roughness is modelled through two RRFs: the original Ament's roughness reduction factor [7] and modified Ament's RRF with shadowing effect included as proposed in [9] and implemented for ducting propagation in [10].

2. DESCRIPTION OF THE METHOD

To compute the path loss for the studied links, the log-linear M -profile (1) from [2] for evaporation duct is combined with the PE method. Equation (2) below presents the original Ament's roughness reduction coefficient R_A [7]. The R_{rf} from (3) is obtained in [9] using the same statistics (Gaussian statistics of sea surface heights and slopes) as the one assumed for the derivation of the original Ament's roughness reduction factor R_A . The R_{rf} from (3) accounts for the shadowing effect of the sea surface roughness by introducing a phase correction to R_A . In (2) and (3) k is the wave number in free space, φ is the plane wave grazing incidence angle to the rough surface, σ_ξ is the standard deviation of the surface height ξ , \tilde{m}_ξ and $\tilde{\sigma}_\xi$ are the mean value and standard deviation of the illuminated surface heights only (see [9] for details), $Q=2k\sin(\varphi)$.

$$R_{eff} = R_{rf} R_A \quad , \quad (1)$$

$$R_A = \exp\left[-2k^2\sigma_\xi^2\sin^2(\varphi)\right] \quad , \quad (2)$$

$$R_{rf} = \exp\left(-jQ\tilde{m}_\xi - \frac{Q^2\tilde{\sigma}_\xi^2}{2}\right) \quad (3)$$

The parameters σ_ξ , \tilde{m}_ξ , and $\tilde{\sigma}_\xi$ needed to compute (2) and (3) are taken for wind speed of 7 km/s, see [9, 10] for formulas and details.

3. RESULTS AND DISCUSSION

As in [2], for every frequency the path loss (PL) is calculated versus height for fixed ranges $R=20$ km, $R=40$ km for the same four hypothetical links: A) $z_t=40$ m, $\theta_0=5^\circ$; B) $z_t=15$ m, $\theta_0=5^\circ$; C) $z_t=40$ m, $\theta_0=1^\circ$; D) $z_t=15$ m, $\theta_0=1^\circ$, where z_t stays for the transmitter height, θ_0 and θ_s are the half power beamwidth and the antenna elevation angle of horizontally polarized Gaussian beam source used as transmitter, see [2], formula (3). Three different values for the critical potential refractivity gradient c_0 (which determines the curvature of the log-linear modified refractivity profile) are

used for neutral, stable and unstable troposphere, respectively: $c_0=0.13$, $c_0=0.11$ and $c_0=0.19$. For all cases $\theta_s=0^\circ$. The area of interests (determined by the possible receiver heights z_r) extends between 5 m and 150 m and is divided in the same two parts as in [2]: z_1 from 5 m to the top of evaporation layer, defined here as $z_L=2z_d$, see [2], and z_2 which ranges from the evaporation layer height z_L up to 150 m; z_d is the evaporation duct height.

On Figs. 1-4 are shown results for rough sea surface. Figure 1 shows the influence of the roughness reduction factor R_A from (2) for original Ament roughness reduction coefficient: the introduction of R_A increases the frequency dependency and leads to reduction of the standard deviation values for higher frequencies both in z_1 and z_2 areas. Figures 2-4 present comparison between smooth sea and rough sea modelled with R_A and R_{rf} from (3): Fig. 2 refers to link A) with $z_d=15$ m, $R=20$ km; Fig. 3 reports comparison between $c_0=0.11$ and $c_0=0.19$ for R_{rf} from (3) for link A) with $z_d=15$ m, $R=20$ km; Fig. 4 refers to link C) with $z_d=35$ m, $R=40$ km. The roughness with application of shadowing, (3), increases the frequency dependency in comparison to smooth sea and in z_1 often has opposite trend to that of the roughness introduced through R_A . In z_2 , for higher frequencies, the frequency dependency of PL standard deviation for R_{rf} from (3) follows that obtained for R_A but with higher values. In [10] it has been demonstrated that the introduction of the rough sea surface and, especially, of the roughness reduction factor given by (3), destroys the (guiding) duct structure and reduces the long-range ducted propagation. The electromagnetic energy is scattered by the roughness and this reduces the fading depths for all links and distances. The higher the frequency, the higher the depths reduction.

In area z_2 increases the difference in PL standard deviation frequency dependency between stable ($c_0=0.11$) and unstable ($c_0=0.19$) troposphere stratification, see Fig. 3.

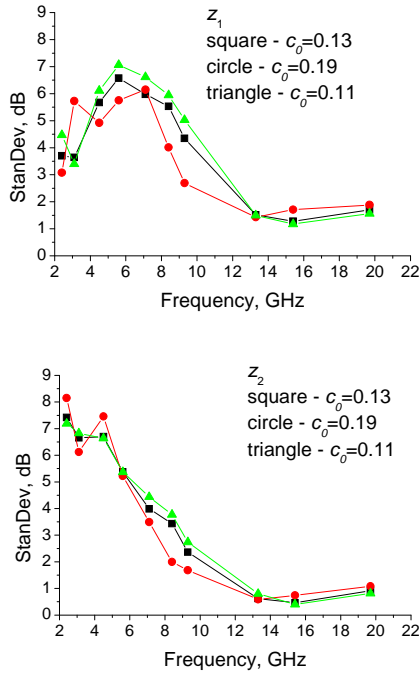


Figure 1. Rough sea surface: R_A from (2), $z_d = 35$ m, $R = 40$ km, link C

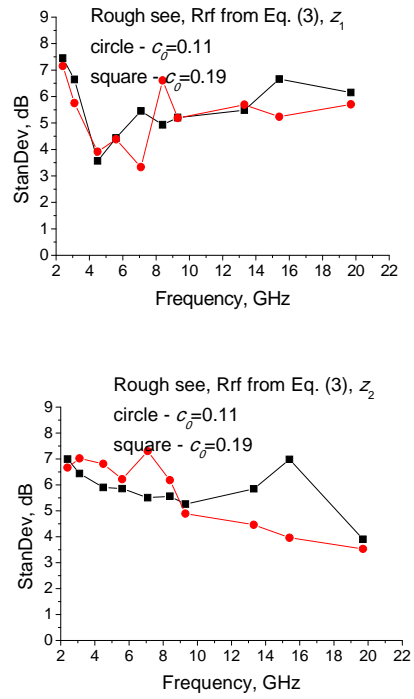


Figure 3. Comparison between $c_0 = 0.11$ & $c_0 = 0.19$ for R_{rf} from (3), link A, $z_d=15$ m, $R=20$ km

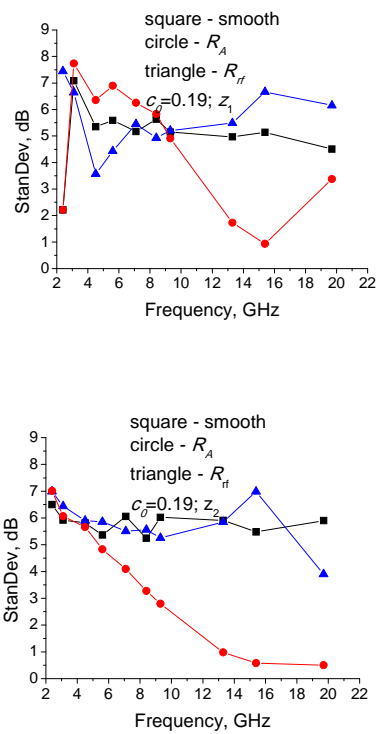
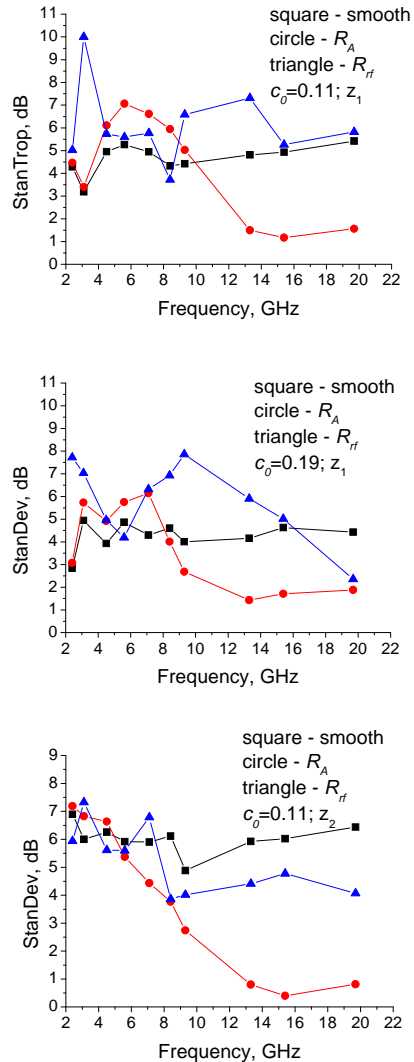


Figure 2. Comparison between smooth sea, original R_A , and R_{rf} from (3), link A, $z_d=15$ m, $R=20$ km



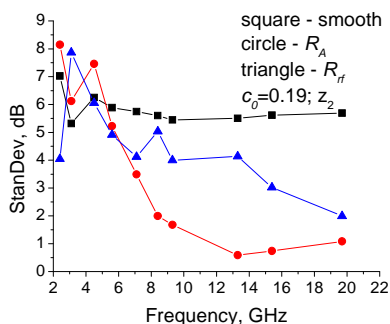


Figure 4. Comparison between smooth sea, original Ament R_A , and R_r from (3), link C, $z_0=35$ m, $R=40$ km

4. CONCLUSION

On the basis of Figs. 1-4 (as well as other results not reported here) the following concluding remarks may be drawn:

- the roughness introduced through R_A increases the frequency dependency of the PL standard deviation in the same time decreasing its values for higher frequencies;
- the introduction of shadowing effect influences both z_1 and z_2 regions, it modifies the tendency of the original Ament's roughness reduction factor to reduce the values of standard deviation for higher frequencies;
- in further investigations more attention should be paid on the combined effect of different from neutral troposphere stratification and sea surface roughness;
- the reported results for sea surface roughness influence on frequency dependent fading can not be assessed using traditional methods.

More investigations with application of different RRFs and corrections for shadowing (and, possibly, attraction of additional scattering mechanisms as diffraction) as well as further comparisons to measurement data are needed in order to substantiate the reported results.

5. ACKNOWLEDGMENTS

This work was supported in part by the Ministry of Education and Science of Bulgaria under grant agreement № D01-151/2018.

REFERENCES

- [1] D. E. Kerr, (Ed.) Propagation of Short Radio Waves, Peter Peregrinus, London, UK, 1987.
- [2] I. Sirkova, "Frequency Dependency of Multipath Fading over the Sea under Ducting. Part I: Simulation Results for Refractivity Profiles' Parameters Influence", CEMA, 2019.
- [3] R. L. Olsen, T. Tjelta, L. Martin, and B. Segal, "World-wide Techniques for Predicting the Multipath Fading Distribution on Terrestrial LOS Links: Comparison With Regional Techniques", IEEE Trans, Vol. AP-51, No. 1, 2003, 23-30.
- [4] ITU-R P.530-9, "Propagation Data and Prediction Methods Required for the Design of Terrestrial Line-of-Sight Systems", 2001.
- [5] M. Levy, Parabolic Equation Methods for Electromagnetic Wave Propagation, IEE electromagnetic waves series 45, UK, 2000.
- [6] A. R. Miller, R. M. Brown, and E. Vegh, "New Derivation for the Rough Surface Reflection Coefficient and for the Distribution of Sea-Wave Elevations", IEE Proc.-H, Vol. 131, 1984, 114–116.
- [7] W. S. Ament, "Toward a Theory of Reflection by a Rough Surface", Proc. IRE, Vol. 41, No. 1, 1953, 142–146.
- [8] D. E. Freund, N. E. Woods, H.-CH. Ku, and R. S. Awadallah, "The Effects of Shadowing on Modeling Forward Radar Propagation over a Rough Sea Surface", Waves in Random and Complex Media, Vol. 18, No. 3, 2008, 387–408.
- [9] V. Fabbro, C. Bourlier, and P. F. Combes, "Forward Propagation Modeling above Gaussian Rough Surfaces by the Parabolic Wave Equation: Introduction of the Shadowing Effect", Progress in Electromagnetics Research, Vol. 58, 2006, 243–269.
- [10] I. Sirkova, "Propagation Factor and Path Loss Simulation Results for Two Rough Surface Reflection Coefficients Applied to the Microwave Ducting Propagation over the Sea", Progress in Electromagnetics Research M, Vol. 17, 2011, 151–166.

IMPROVING THE PERFORMANCE OF TURBULENT FREE SPACE OPTICAL LINK BY USING A FOURIER FILTER

Jassim Mohammed Jassim, R. N. Ali, Ahmed. B. Sharba,
Mariam Kadhim Jawad and Khalid Mahdi Jasim

College of Science for Women/Laser Physics Depart./University of Babylon/Iraq

Abstract

In the free space terrestrial optical communication (FOSC) the laser beam, as an information carrier, is subject to degradation due to atmospheric turbulence. In this work, the decrease in the signal to noise ratio (SNR) and the increase in the value of the bit-error rate (BER), due to this turbulence, are experimentally investigated. In addition, a pin-hole, as a Fourier low-pass filter, has been utilized to suppress turbulence noise. The results show a dramatic improvement in the received optical signal, and hence the link BER. The values of the SNR have been enhanced from (18.8940 dB), to (46.1365 dB) by reducing the pin-hole diameter. The value of BER has been also reduced from (0.7246×10^{-5}) to (5.6×10^{-12}) in a strong turbulent environment.

Keywords: FSO link, Atmospheric turbulence, Laser beam, Signal-to-noise ratio, Bit-error-rate, Fourier Optics Filter Pinhole.

1. INTRODUCTION

The free space terrestrial optical communication (FSOC) systems have very promising applications for its very well-known advantages such as the large bandwidth, flexibility and low-cost investment [1]. However, the FSOC technology has major weaknesses to be overcome, namely the presence of attenuation and fluctuations in intensity. The attenuation is caused by absorption and scattering due to various gases and particles in atmospheric propagation medium. The fluctuation of intensity is caused by atmospheric turbulence due to the temporal and spatial temperature variation of the atmosphere [2] and [3].

In an optical communication system, the bit error rate BER is greatly affected by these losses due to attenuation and atmospheric turbulence. The atmospheric attenuation and turbulence lead to degrade the signal-to-noise ratio (SNR) and increase the (BER), i.e., increase the probability of errors in the received signal [4]. In addition to the attenuation, there are three effects of atmosphere turbulence: scintillation, laser beam spreading, and laser beam wander. Scintillation is due to variation in the refractive index structure of air, so if the laser beam travels through scintillation, it will experience intensity fluctuations. The SNR and BER depend on atmospheric turbulence and geometric losses represented by scintillation. Therefore, FOS systems should be designed to minimize the effects of scintillation.

In this work we present an experimental investigation on a technique that can be utilized to suppress optical signal noise. In this technique a circular

pinhole is used as a low-pass spatial filter. The circular aperture of the receiver optics diffracts the laser beam forming an Airy pattern. The information signals concentrate at the central disc with low spatial frequencies, while noise signal is usually characterized by its high spatial frequencies. Therefore a pinhole rejects the high frequencies, hence improves the optical signal at the receiver focal plane. In other words using the pinhole enhances the BER of the optical communication system.

2. THEORY

The SNR and the BER are the main parameters that characterize the quality of communication systems. BER depends on the SNR which in turn depends on the scintillation strength, the beam spreading and the average received power [5]. The active area of the optical detector, in the receiver unit, is assumed to be large enough so that the SNR value includes the scintillation effects. The scintillation index σ_I^2 describes the intensity fluctuation as the normalized difference of the intensity fluctuations. The strength of scintillation can be measured in terms of the variation of the beam amplitude or the irradiance σ_I^2 which can be expressed as follows [6]:

$$\sigma_I^2 = \frac{\langle I^2 \rangle}{\langle I \rangle^2} - 1 \quad (1)$$

where I : is the irradiance of signal (or intensity).

For weak fluctuation regime (scintillation index less than 1), the scintillation index is proportional to the

Rytov variance of a plane wave, which is given by [7]:

$$\sigma_i^2 = 1.23 C_n^2 k^{7/6} l^{11/6}$$

From this equation we can find the value of C_n^2 as follows:

$$C_n^2 = \frac{\sigma_i^2}{1.23 k^{7/6} l^{11/6}} \quad (2)$$

where: C_n^2 is the refractive index structure parameter, k is the optical number, and l is the length of the transmission path.

The first feature of a FSO communication system is the SNR. Based on Kolmogorov's theory, the SNR and BER from turbulence were expressed as follows [8][9]:

$$SNR = (0.31 C_n^2 k^{7/6} l^{11/6})^{-1} \quad (3)$$

and

$$BER = \frac{\exp(-SNR/2)}{(2\pi SNR)^{0.5}} \quad (4)$$

To suppress the turbulence noise and improve the BER, a pinhole is used as a spatial low-pass filter. The noise signals are usually characterized by their high spatial frequencies while the information signal has low spatial frequencies.

3. EXPERIMENTAL SET-UP

Figure (1) shows the schematic diagram of the turbulence cell. This cell is designed and built in the laboratory to accomplish the simulation of turbulence. The setup includes a He-Ne laser source with an appropriate collimating lens, a turbulence cell, variable size pinholes (0.2, 0.4, 0.6, 1, 1.5) mm, a 10 cm focal length lens, and an oscilloscope.

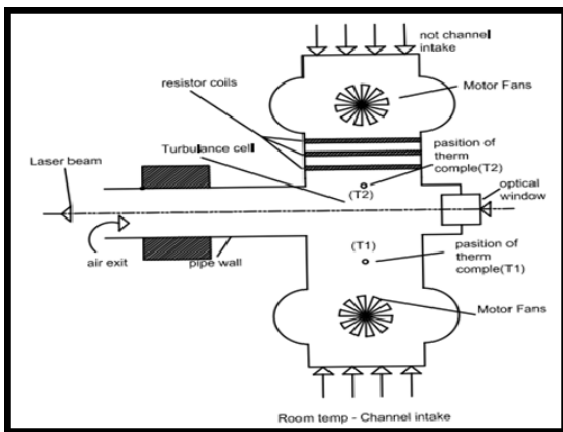


Figure 1: Schematic diagram of a turbulence cell

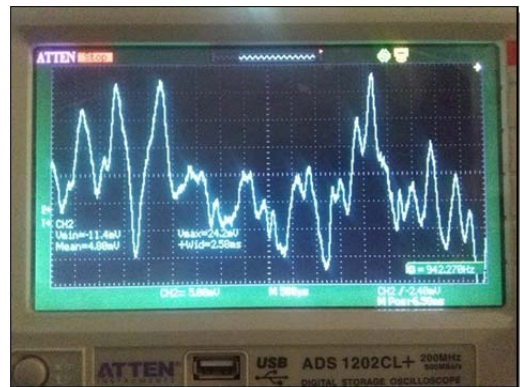
3.1. Results and Discussion

A controllable pseudo-turbulent weather has been created in the lab by using the design described in the previous section. The refractive index structure parameter ($C_n^2 \sim 10 \cdot 10^{-9} m^{-2/3}$) is measured at a temperature difference ($\Delta T |T1-T2| = 47.5 K$) and flow speed of ($V=3.4 m/s$) for a short range link ($l=1.6 m$).

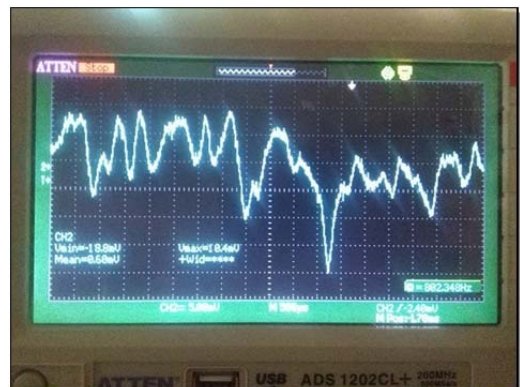
The values of scintillation, SNR, and the BER are measured under different conditions, where a pinhole aperture of variable diameters (0.2 mm, 0.4 mm, 0.6 mm, 1 mm, and 1.5 mm) have been used as Fourier spatial filters. Figures (2 a, b, c, d, and e) show the real time fluctuations with different aperture size.

The measured values for signal intensity and the scintillation are shown in figures (3) & (4).

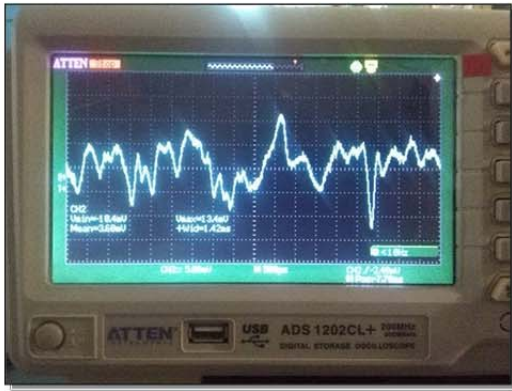
As shown the turbulence effect, due to the refractive index structure parameter has been reduced from ($0.5 \cdot 10^{-9} m^{-2/3}$) to ($0.2 \cdot 10^{-9} m^{-2/3}$). Accordingly, the (S/N) ratio has increased from ($0.7 \cdot 10^{-5}$) to ($5.6 \cdot 10^{-12}$) as shown in figures (5) & (6). These results are in a good agreement with those in Refs. [10][11].



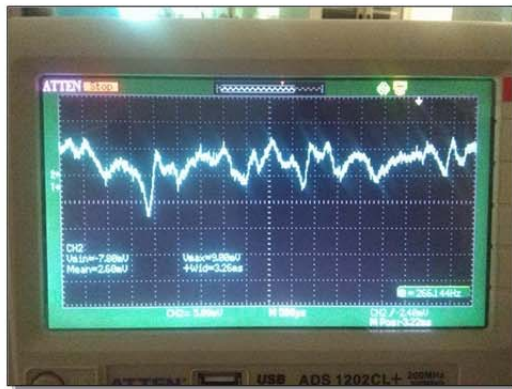
a)



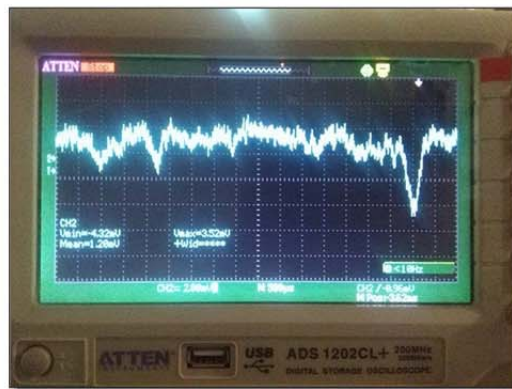
b)



c)



d)



e)

Figure 2: The effect of aperture size on signal variation

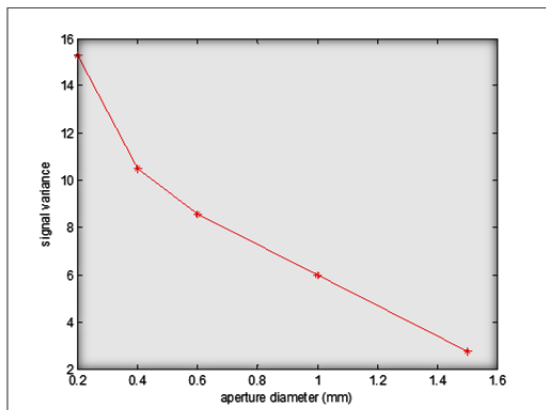


Figure 3: The effect of changing the aperture diameter on signal variance

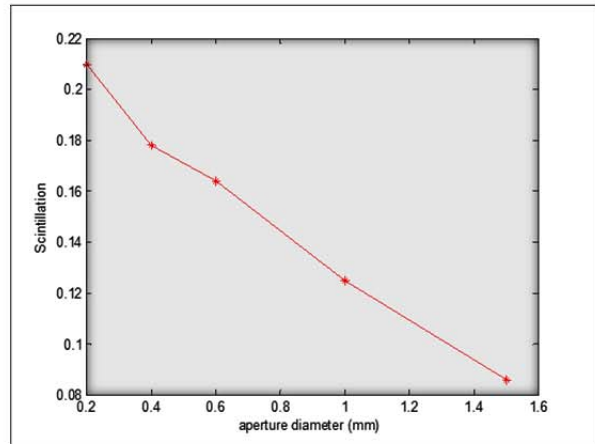


Figure 4: The effect of aperture diameter on the scintillations

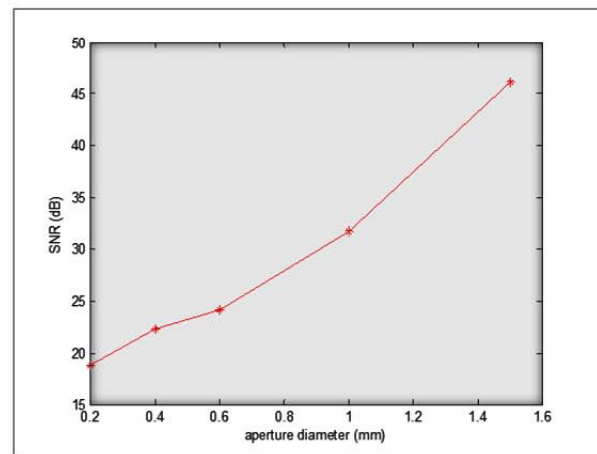


Figure 5: The effect of aperture diameter on the SNR

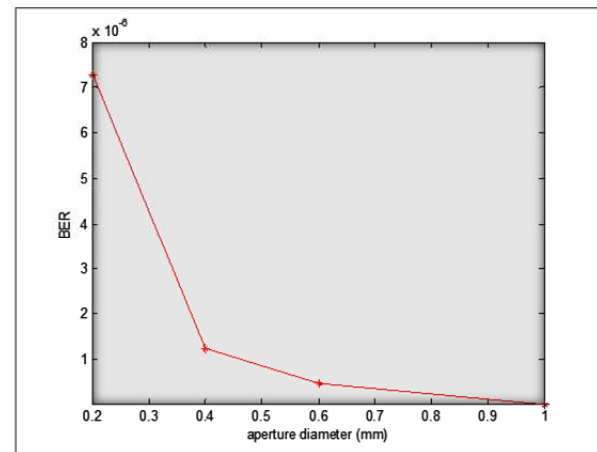


Figure 6: The effect of aperture diameter on the BER

The calculated value of the signal spot size is about (15 μm) while the optimum signal is obtained by utilizing a (1.5 mm) aperture spatial filter. This discrepancy is due to beam wandering, where the average received signal power covers an area of (2.5*2.6 mm²) as shown in figure (7).

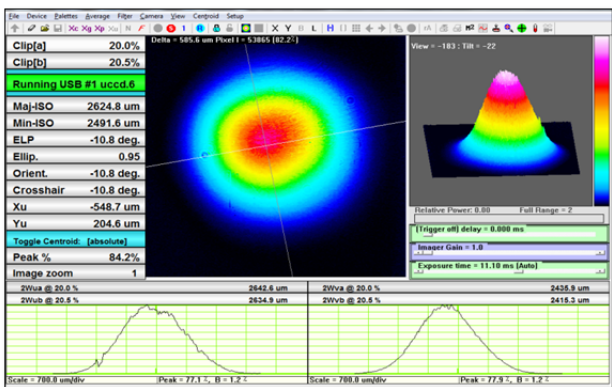


Figure 7: Laser beam profile under high turbulence

Table 1: The effect of aperture diameter on the SNR and BER values

aperture diameter (mm)	σ_i^2	$C_n^2 (m^{-2/3})$	SNR	BER
0.2	0.21	0.4958×10^{-9}	18.88	0.728×10^{-5}
0.4	0.178	0.42×10^{-9}	22.279	0.1228×10^{-5}
0.6	0.164	0.3872×10^{-9}	24.18	0.455×10^{-6}
1	0.125	0.2951×10^{-9}	31.725	0.9×10^{-8}
1.5	0.086	0.2×10^{-9}	46.1125	5.6×10^{-12}

4. CONCLUSION

Both SNR and BER are clearly affected by atmospheric turbulences. When the turbulence is low, the value of the SNR increases, hence the values of BER reduces.

The proper spatial filter aperture size that gives the optimum performance, for this specific system, is about (1.5 mm).

REFERENCES

- [1] Davis, Christopher C., Igor I. Smolyaninov, and Stuart D. Milner., "Flexible optical wireless links and networks.", IEEE Communications Magazine, Vol. 41, No. 3, pp. 51-57, 2003.
- [2] Henniger, Hennes., "Transmission performance analysis of free-space optical communications using gilbert-erasure channel.", IEEE Transactions on Communications, Vol. 60, No. 1, pp. 55-61, 2012.
- [3] R. N. Ali, Jassim, Jassim Mohammed, and Hawraa Hassaball Khribet, "Determine the optical turbulence parameter (C_n^2) in Babylon City-Iraq.", International Journal of Current Engineering and Technology, Vol. 5, No. 1, pp. 221-226, 2015.
- [4] Jassim, Jassim Mohammed. "Experimental Study on the Atmospheric Attenuation Effective on Audio Signals In Free Space Laser Communication Links.", International Journal of Engineering and Innovative Technology (IJEIT), Vol. 3, No. 4, pp. 53-57, 2013.
- [5] A. Chaman Motlagh, V. Ahmadi, Z. Ghassemlooy and K. Abedi, " The Effect of Atmospheric Turbulence on the Performance of the Free Space Optical Communications", In Communication Systems, Networks and Digital Signal Processing, CNSDSP, 6th International Symposium on Communication Systems., IEEE, pp. 540-543, July 2008.
- [6] Zhang, Yixin, Tuo Zhu, and Chunkan Tao., "Aperture-averaging effects for weak to strong scintillations in turbulent atmosphere", Chinese Optics Letters, Vol. 2, No. 7, pp. 373-375, 2004.
- [7] Andrews, Larry C., Ronald L. Phillips, and Cynthia Y. Hopen. "Laser beam scintillation with applications.", Vol. 99. SPIE press, 2001.
- [8] Altowij, Khaleel S., Abdulsalam Alkholidi, and Habib Hamam., "Effect of clear atmospheric turbulence on quality of free space optical communications in Yemen", Frontiers of Optoelectronics in China, Vol. 3, No. 4, pp. 423-428, 2010.
- [9] Xu, G., Zhang, X., Wei, J., and Fu, X., "Influence of atmospheric turbulence on FSO link performance.", In Asia-Pacific Optical and Wireless Communications, International Society for Optics and Photonics, pp. 816-823, May 2004.
- [10] Babu, P. Latsa, and B. Srinivasan. "Characterizing the atmospheric effects on laser beam propagation for free space optical communication." Proc. National Conf. Commun., pp. 332-334, 2008.
- [11] Priambodo, Purnomo Sidi, Ucuk Darusalam, and Eko Tjpto Rahardjo, "Free-space optical propagation noise suppression by Fourier optics filter pin-hole.", International Journal of Optics and Applications, Vol. 5, No. 2, pp. 27-32, 2015.

METHODOLOGY AND ARCHITECTURE OF A COMPUTER-BASED INTERACTIVE TIMING SYSTEM FOR APPLICATIONS IN MEDICINE

Maria Angelova

Technical University – Sofia
1000, 8 Kl. Ohridski Blvd, Sofia
maria@tu-sofia.bg

Kalin Dimitrov

Technical University – Sofia
1000, 8 Kl. Ohridski Blvd, Sofia
kld@tu-sofia.bg

Stefan Valyukov

Therapist
1000, 39 Vladimir Vazov Blvd, Sofia
svalyukov@gmail.com

Abstract

This article describes the design and realization of an Interactive Timing System. Such systems are used in the therapy of children who have learning and attention issues. The concept is that people can “retrain their brain” to focus and work more efficiently. The matching of different beats can help the brain work more efficiently and become more organized.

A similar existing system is observed and a methodology and architecture of a computer program which performs interactive timing is proposed. Open-source software environment is used for the practical realization of the program. Some results of the program functioning are shown.

1. INTRODUCTION

Interactive timing is a computer-based therapy that trains people to match various beats. Concentrating and keeping a beat eventually stimulate the growth of important connections in the brain. This would help children improve their skills. Those skills might include focus, making sense of information, reading, movement and controlling impulsive or aggressive behaviour. Children listen to a beat while wearing headphones. They are asked to clap their hands or tap their feet to the beat. The computer then tells them how well they are doing. The goal is for children to get better at matching various beats over repeated sessions.

Conditions such as ADHD (Attention-Deficit Hyperactivity Disorder), dyslexia, autism, Parkinson’s disease, auditory processing disorders, and other issues are often the result of problems that occur within the brain [9, 10, 11, 12, 14]. Some researchers believe these problems in the brain also impact the brain’s internal clock. Interactive Timing Systems work by addressing these issues in timing [1, 2, 3, 5, 13].

In our observation of existing Interactive Systems we discovered one major product. Interactive Metronome® [4, 6, 7, 8] is an assessment and training tool that measures and improves the synchronization of neural impulses within key brain networks. It helps to improve the cognitive, communicative, sensory and motor performance. As the individual activates a trigger in time with a steady auditory beat, IM technology provides real-time visual feedback for millisecond timing. Knowing whether he is hitting before, after, or exactly in sync with the beat to the millisecond allows the individual to make immediate, online corrections to improve timing over the course of training. It is a well known timing system which requires payment for regular usage.

2. SYSTEM ARCHITECTURE

Figure 1 depicts all components of the system. Before the system starts its operation, it is necessary to set the basic characteristics of the regular beats. This is the time interval in which these beats will be generated and the number of beats per minute. This is usually done by the therapist. The next step is to start the computer program and to ana-

lyze the beats generated by the user. The process of time matching between the two beats (t_i and $t_{\text{click}, i}$) is made by the computer program algorithm. The obtained result R_i is recorded for each beat. The user is able to see his/her current results and the general evaluation after the end of the set time period. The final result is given as an average estimate of the gap between the beats in milliseconds and the percentage of delays and early clicks of the user. Based on this assessment, a change in the user achievements can be traced over time.

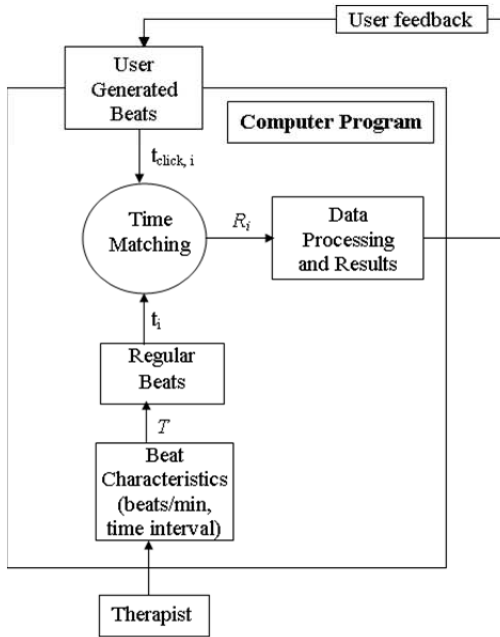


Figure 1. Interactive Time Matching System Architecture

The computer program is meant to be used for children but it is possible to use it for all kinds of patients who want to train their brain timing.

3. TIME MATCHING ALGORITHM

Each result obtained should measure the time gap between the regular and the user beats. It is important to determine when the gap will be considered a delay and when it will be considered as an early click. Figure 2 shows how the Interactive Time Matching System solves this problem.

It applies the following rules:

If the user click occurs before the the middle of the period between the regular beats, the result is considered to be a delay for the current beat and is calculated by formula (1):

$$R_i = t_{\text{click}, i} - t_i \quad (1)$$

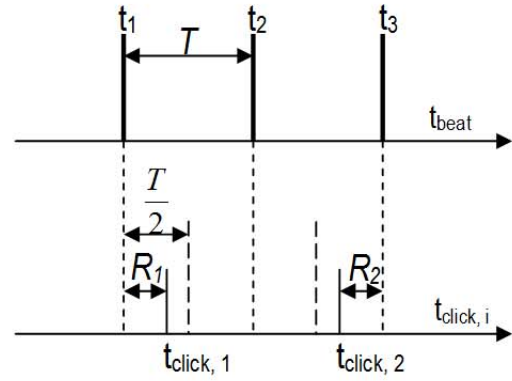


Figure 2. Distribution of user clicks

If the user click occurs after the middle of the period between the regular beats, the result is considered to be an early click for the next regular beat and is calculated by formula (2):

$$R_{i+1} = t_{\text{click}, i} - t_i - T \quad (2)$$

4. COMPUTER PROGRAM INTERFACE

The computer program was created with the free visual object-oriented Lazarus platform. The interface includes all the tools needed to set the initial settings and to track the results (Figure 3). It is possible to use it free of charge and to document the patients' results. Figure 3. Computer Program Interface

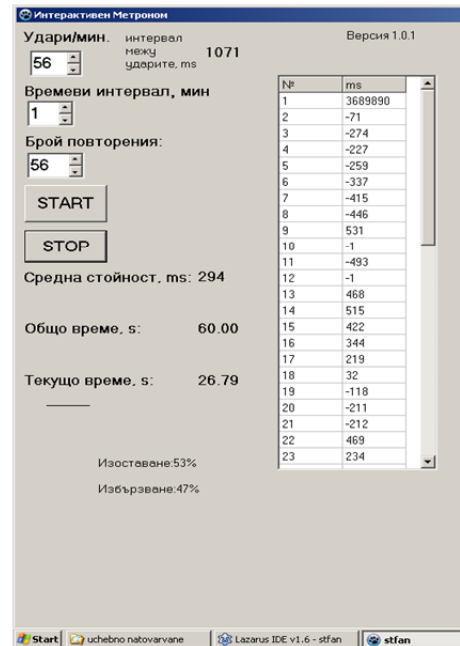


Figure 3. Computer Program Interface

A timer is used to create the regular beats in the program. For the introduction of user beats, a sensor generating OnClick() event is needed. The tim-

ing is done by taking ticks from the Operating System Clock.

After the end of the training process a therapist can evaluate the user results and give directions how to improve the brain timing process.

5. CONCLUSION

Some children and adults experience problems related to malfunction of the internal brain clock. Interactive timing therapy is a good starting point in the effort to help these people. The repetitive training sessions are supervised by therapists who give directions to the patients how to properly conduct their treatment. In order to do so they need reliable tools. The Interactive Timing System described in this article is such a tool. It can assess the user results and trace their achievements over time. The system has a user-friendly and intuitive interface and is developed in an open-source programming environment. It is free of charge and it can reduce the cost of otherwise expensive treatment.

ACKNOWLEDGMENTS

The authors would like to thank the Research and Development Sector at the Technical University of Sofia for the financial support.

REFERENCES

- [1] Lewis, P., "Finding the timer", *Trends in Cognitive Sciences*, 6(5), pp. 195-196, 2002.
- [2] Lewis, P. A., & Miall, R. C., "Remembering the time: a continuous clock", *Trends in Cognitive Sciences*, 10(9), pp. 401-406, 2006.
- [3] Lewis P. & Walsh, V., "Time perception: Components of the brains clock", *Current Biology*, 24, pp. 389-391, 2005.
- [4] Libkuman, T. M. & Otani, H., "Training in timing improves accuracy in golf", *Journal of General Psychology*, 129, pp. 77-96, 2002.
- [5] Rammsayer, T. & Brandler, S., "Performance on temporal information processing as an index of general intelligence", *Intelligence*, 35(2), pp. 123-139, 2007.
- [6] Ritter, M., Colson, K. A., & Park, J., "Reading intervention using Interactive Metronome in children with language and reading improvement: A preliminary investigation", *Communications Disorders Quarterly*, 34(2), pp. 106-119.
- [7] Shaffer, R. J., Jacokes, L. E., Cassily, J. F., Greenspan, R.F., Tuchman, P.J., & Stemmer, P.J., "Effect of interactive metronome training on children with ADHD", *American Journal of Occupational Therapy*, 55, pp. 155-161, 2001.
- [8] Nelson, L., "Effects of Interactive Metronome on cognition and electrocortical functioning in recovery from blast related brain injury (BRBI)", *Presentation at Interactive Metronome Professional Conference*, San Antonio, Texas, 2012.
- [9] McGrew, K., & Vega, A., "The efficacy of rhythm - based (mental timing) treatments with subjects with a variety of clinical disorders: A brief review of theoretical, diagnostic, and treatment research", *Institute for Applied Psychometrics Research Report*, No. 9, 2009.
- [10] Taub, G. E., McGrew, K. S., & Keith, T. Z., "Improvements in interval time tracking and effects on reading achievement", *Psychology in the Schools*, 44(8), pp. 849-863, 2007.
- [11] Mauk, M., & Buonomano, D., "The neural basis of temporal processing", *Annual Review of Neuroscience*, 27, pp. 207-340, 2004.
- [12] Kane, M. J., & McVay, J. C., "What mind wandering reveals about executive - control abilities and failures", *Current Directions in Psychological Science*, 21(5), pp. 348-354, 2012.
- [13] Hunt, E., *Human intelligence*, Cambridge, NY: Cambridge University Press, 2011.
- [14] Guergov, S. Acupressure in magneto therapy environment, *Series on Biomechanics, Peer-reviewed Journal Edited by Bulgarian Academy of Science*, Vol.32, No.1 (2018), p.16-19

INNOVATIVE BIOMONITORING SYSTEMS IN THE AEROSPACE INDUSTRY

Evgeni Andreev¹, Veselka Radeva², Mariya Nikolova³

N. Y. Vaptsarov NAVAL ACADEMY
73 V. Drumev St.
Varna 9026, BULGARIA

E-mail: e.andreev@naval-acad.bg¹; veselka.radeva@gmail.com²; mpn@abv.bg³

Abstract

The article presents the development of space telemedicine. The main biomedical parameters of astronauts from the International Space Station (ISS) are presented. The results of a project for a space medical center at a space airport of students from Nikola Vaptsarov Naval Academy - Varna and Medical University - Varna were discussed. The project was presented at the international competition Student aerospace challenge, the European Space Agency (ESA). Particular attention is paid to the innovative Astroskin Bio-Monitor system. The report proposes the creation of: a medical satellite system, Medical Data, Artificial Intelligence (AI) software, and surgical robots to permanently monitor, diagnose, and make decisions on astronaut health. A block diagram of the interaction between the "healing system (artificial intelligence + physician) and the astronaut patient" is presented.

1. INTRODUCTION

The up-to-date problem of the application of innovative biomonitoring systems in the aerospace industry stems from:

- The large number of ISS-related projects requiring astronauts to stay in space for a longer period of time;
- Space programs are being developed to: create moon bases; to launch and develop space tourism.

This requires a very rapid development of the methods and means of space telemedicine.

2. SPACE TELEMEDICINE

Telemedicine has been and will be vital to space travel, as astronauts must have access to treatment by a doctor even though they are thousands of kilometers away from the Earth.

NASA's first space-based telemedicine connection was created as part of Spacelab's ten-day mission in the 1990s. Then, for the first time, doctors from the Mission Control Center could explore images of the astronaut's heart. Today, thanks to improvements [6] in satellite communications, space agencies have expanded the applications of space telemedicine. In our time, astronaut medical services combine preventive, therapeutic and diagnostic assistance.

Innovation in space medicine is growing thanks to the commercialization of new space companies such as Richard Branson's Virgin Galactic. In August 2017, SpaceX transported the TechShot processor for advanced spacecraft experiments for regenerative medicine at the International Space Station (ISS).

2.1. Medical problems solved by the methods of space telemedicine

Radiation and microgravity affect the physical and psychological state of astronauts. This requires continuous medical control of their health and employability. Telemedicine is an important component in the medical service of astronauts at the ISS. Space Telemedicine enables preventive, diagnostic and therapeutic care for many months in space and ideally allows permanent care for the crew before and after space missions [2, 4].

Telemedicine combines medical equipment with a well-planned and tested communication system that enables the safe transfer of medical data, other information and expertise from the ISS to the Earth and vice versa, if necessary.

When a crew member has a medical problem, the first action is a video link to a surgeon.

A case is known [1] in which a member of the ISS crew with a history of knee trauma (no pre-mission symptoms) received severe knee pain while training with a nursing device. In an organized private medi-

cal conference, the physician from the Earth asks for an ultrasound of the affected joint. After reviewing the full set of images (downloaded from the ISU within an hour), the radiologist has confirmed the problem and prescribed treatment. The astronaut has seamlessly accomplished the mission.

Astronauts are now undergoing longer missions onboard the space station, which provide important data on long-term physiological effects in microgravity. Other challenges for the crew in space are: physiological adaptations to microgravity, radiation exposure, extreme temperatures and vacuum, and psychosocial reactions to the space flight. Ten dozen years ago, doctors noticed that crew members returned with marked structural changes in their eyes. The condition is called Space flight-associated neuro-ocular syndrome (SANS) [3].

2.2. Innovative astronaut condition monitoring systems

Some of the astronauts' health problems are solved by ultrasound review. Ultrasound is mounted to be able to send data efficiently by means of a limited and stable planned connection to ground control and using water instead of ultrasonic gel, which would be one more thing to be delivered to the station regularly. But it has also been changed to be as user-friendly as possible by non-medical professionals who have gone through the process from a remote targeting team.

A portable vital signs monitor Tempus Pro has been developed [11]. He conducted telemedicine via satellite, helping the medics to study the state of ESA astronauts on landing.

For exploration of the Space flight-associated neuro-ocular syndrome, NASA delivers a special scanner, an optical device for coherent tomography to the ISS station.

The intelligent clothing Astroskin [9, 10] is at trial. It brings together data from Earth and Space health studies. Astroskin includes the most modern monitoring of blood pressure, pulse oximetry, 3-channel ECG, breathing, skin temperature and activity sensors for 48 hours continuous real-time monitoring. The system includes iOS for iPhone and iPad, data synchronization software, and web dashboard. It is already in use at ISS (2018).

WHAT ASTROSKIN MONITORS?

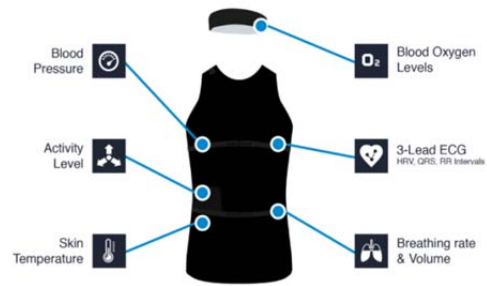


Figure 1. ASTROSKIN [10]

Robots are helping the astronauts. After NASA's Robonaut, Interactive Robot CIMON (Crew Interactive MOBILE Companion) [8] first appeared on the ISS in 2018 and has artificial intelligence.



Figure 2. CIMON (Crew Interactive MOBILE Companion) [8]

„Flying Brain“, as Simon is called by his creators, has established visual contact with an astronaut, shot it and recorded a video. But it is not used to establish medical indices.

On June 13, 2019, NASA and ESA astronauts completed the final stage of the Airway Monitoring experiment [9]. The purpose of this experiment is to investigate the influence of circulating dust in space on astronaut's lung health.

3. PROPOSALS TO EXPAND THE CAPABILITIES OF SPACE TELEMEDICINE

Teachers and students from the Naval Academy „N. Vaptsarov“ – Varna have been working on various space issues for several years in NASA [5] and ESA projects. Students from the Naval Academy have traditionally participated in the international competition of the European Space Agency Student aerospace challenge [7]. For the first time this year a team of students from our Academy and the Medical University – Varna participated in this competition. They have prepared a space medical space project for a space airport that will provide medical assistance to future space travelers. The project

was honored by over a hundred proposals and attracted great interest in the final conference of the competition in June 2019 at the ESA Aerospace Center in France. One of the problems that the team has developed has been related to the possibilities of space telemedicine and the expansion of its capabilities.



Figure 3. Telemedicine for space travellers [7]

Particular attention is paid to the device astroskin. Astroskin could be upgraded and developed from the existing type of "jingle" to the options: "t-shirt – shorts" and/or "long pants – sweater without hood". For additional diagnosis, "we suggest adding a forehead or an astroshade strip consisting of metallic threads with special sensors and brain condition monitoring transmitters. It is of utmost importance for each space agency to use the medical data on the Earth in a computer before flight (pre-flight comparison data), astroskin for continuous observation, ultrasound for medical critical situation and and Tempus Pro on landing. The data are collected in the Medical Database. Artificial Intelligence in the ISS makes an analysis if there is a difference in the indicators in the Medical Data Base, decides to consult with a doctor on duty and co-ordinates with it a decision for possible treatment; provides medical information and recommendations to an on-board robot-surgeon.

We also offer a system of LEO medical satellites at a height of 100 to 500 km to collect and store ISS data as well as to make contact with Earth doctors in a more sophisticated medical case.

Another proposal is to extend the Robonaut robot functions. Surgical functions are added (Figure 4). We suggest that the robot walk around a rail around the astronaut's bed and perform an operation (if necessary).

We plan to develop "smart glasses" to prevent the impact of cosmic rays on astronaut's eyes. In addition, in their design, we propose to incorporate sensors to monitor the state of the internal organs like iris diagnostics. In this way, initial eye changes could be diagnosed as a result of the lack of gravity



Figure 4. Robonaut – with advanced medical manipulation capabilities [12]

We propose a block diagram of the interaction between the "healing system (artificial intelligence + physician) and the astronaut patient" – Figure 5.

The robot with an artificial intelligence must have self-learning features by receiving information from the Internet. AI can view and analyze video footage by self-learning and creating instruction for preparation, the materials needed to do so, and whether it is possible for himself / herself to perform the steps he / she has analyzed and recorded. The robot can analyze the success rate of human-made operations and assess the possible success rate of a possible operation.

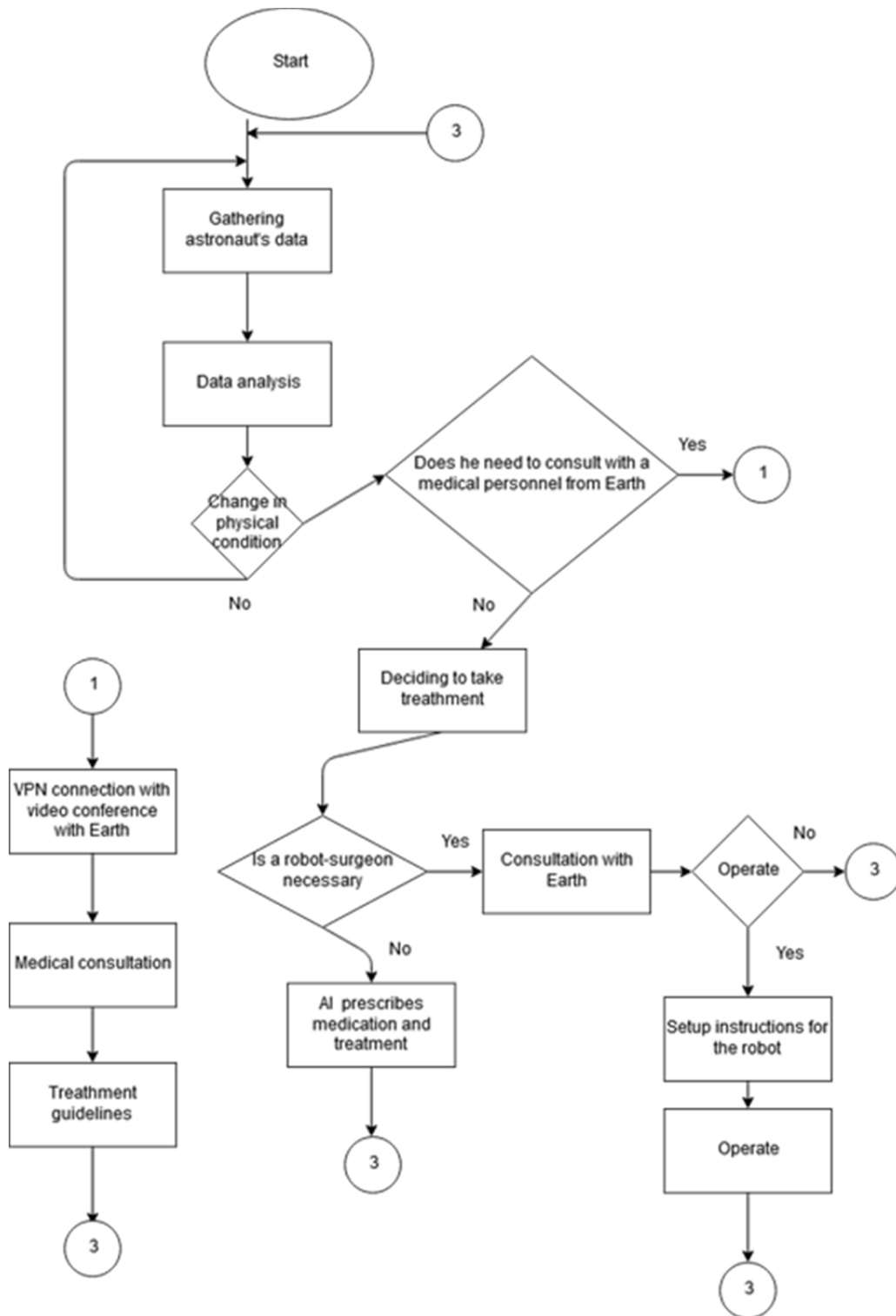


Figure 5. Block diagram of the interaction between the "healing system (artificial intelligence + physician) and the astronaut patient"

The robot with an artificial intelligence must have self-learning features by receiving information from the Internet. AI can view and analyze video footage by self-learning and creating instruction for preparation, the materials needed to do so, and whether it is possible for himself / herself to perform the steps he / she has analyzed and recorded. The robot can analyze the success rate of human-made opera-

tions and assess the possible success rate of a possible operation.

4. CONCLUSION

The role of space telemedicine is growing with the rapid development of space flight technology for people. The suggestions made by the authors are applicable to existing and future space centers.

Innovations such as artificial intelligence robot-surgeons will greatly enhance the quality of life and work of astronauts. They are the basis of the future cosmic telemedicine, which will be the key to the success of the acquisition of the near and far space.

REFERENCES

- [1] A. Menon, S. Moynihan, K. Garcia, A. Sargsyan, "How NASA Uses Telemedicine to Care for Astronauts in Space", *TECHNOLOGY*, Harvard Business Review, 2017.
- [2] A. Nicogossian, D. F. Pober, S. A. Roy, Evolution of telemedicine in space programs and applications on earth, *Telemedicine Journal and e-Health* Vol. 7, No. 1, 2004.
- [3] A. Lee, T. H. Mader, C. Robert Gibson, T. J. Brunstetter, and William J. Tarver, Space flight-associated neuro-ocular syndrome (SANS), *Eye*. The Royal College of Ophthalmologists, 2018.
- [4] B. HEALEY, Telemedicine is vital in space, but soon Earthlings will benefit too, *Health*, 2017.
- [5] E. Andreev, M. Nikolova, V. Radeva, and G. Bochev, Creating Moon port and spaceship simulations in a virtual environment, *AIP Conference Proceedings*, Volume 2048, Issue 1, 2018, <https://doi.org/10.1063/1.5082046>
- [6] P. Andreeva, M. Karev and Ts. Kovacheva, Decision making in prioritization of required operational capabilities, *AIP Conference Proceedings* 1684, 110001 (2015); <https://doi.org/10.1063/1.4934344>
- [7] Project "Space Medical Center", Student Aerospace Challenge, ESA Student Contest, France, 2019.
- [8] <https://www.airbus.com/newsroom/press-releases/en/2018/02/hello--i-am-cimon-.html>
- [9] https://www.esa.int/Our_Activities/Human_and_Robotic_Exploration/International_Space_Station/Lung_health_algae_and_radiation_research_on_Space_Station
- [10] <https://www.hexoskin.com/blogs/news/astroskin>
- [11] <http://www.asc-csa.gc.ca/eng/sciences/bio-monitor.asp>
- [12] <https://www.theverge.com/2012/2/16/2802290/nasa-robot-human-robot-handshake-iss>

X-RAY IMAGE PROCESSING FOR TISSUE INVOLVEMENT-BASED CARIES DETECTION

Veska Georgieva, Plamen Petrov

Technical University of Sofia, Bulgaria
Sofia 1000, 8 Kl. Ohridski Blvd.
T. +359 (2) 965-3293;
E. vesg@tu-sofia.bg, ppetrov@tu-sofia.bg

Barna Iantovics

University of Medicine, Pharmacy, Sciences and Technology, of Targu Mures, Romania
Targu Mures, 540139, Gh. Marinescu 38,
T. +40265215551
E. barna.iantovics@umsft.ro

Abstract

X-ray images improvement is very important for early detection of dental caries, which prevents in some cases more futures complications. The low quality of these images is caused by low spatial resolution and the presence of artefacts and noise. This paper presents an effective approach for X-ray image processing for tissue involvement-based caries detection. It is based on contrast enhancement and noise suppression based on modified homomorphic wavelet filter. It uses adaptive wavelet packet shrinkage decomposition and adaptive threshold of wavelet coefficients to reduce noise components and to eliminate non-uniformity luminance distribution. For better visual observation of the detected caries the split and merge segmentation is applied.

1. INTRODUCTION

An accurate dental diagnosis will result in treatment, which will potentially use the benefit of non-invasive types of treatment at an earlier stage of caries development. X-ray images are most used for detecting caries, determining the depth of involvement and identifying the caries status. The "artifact" in diagnostic X-ray images can be presented as light or dark spots, lines, fogging, speckles, etc. [1]. The quantum noise is dominant and comes from the quantization of energy into photons. Photon noise results from the statistical nature of electromagnetic waves, which include visible light, x-rays and γ -rays with a probability distribution that is a Poisson distribution. It is not independent of the signal nor is it additive [1]. Metal artifacts severely degrade the image quality, particularly near metal surfaces [2].

X-ray image processing can help to obtain better results in caries detection.

The most enhancement methods, which are reported in the literature include classical homomorphic filtering, adaptive contrast stretching, and adaptive morphological transformation to obtain the enhanced image with a uniform illumination [3,4]. The algorithms based on combination of sharpening and enhancement method are used to overcome these

problems. Three types of proposed compound algorithms are used: sharp adaptive histogram equalization (SAHE), sharp median adaptive histogram equalization (SMAHE) and sharp contrast adaptive histogram equalization (SCLAHE) [5]. They are useful applied on the detection of only three types of dental pathology, which are periapical radiolucency, widen periodontal ligament space and loss of lamina dura [6]. Wavelet discrete transform (WDT) and wavelet shrinkage are used to restore the blurred image getting better visual and statistical properties of images [7]. The wavelet thresholding scheme [8,9], recognizes that by performing a wavelet transform of a noisy image, random noise will be represented principally as small coefficients in the high frequency sub-bands. They can be set to zero, and so will be eliminated much of the noise in the image. For optimizing diagnosis of dental caries another approach was proposed [10]. It uses contrast limited adaptive histogram equalization (CLAHE) and homomorphic wavelet filtering for eliminating of non-uniformity luminance distribution of image and noise reduction. It shows good results for detecting of cervical caries and root caries.

In the case of tissue involvement-based caries is important to obtain information about the area of enamel destruction and the depth of the structural defect. For these considerations, a pre-processed

stage, based on contrast enhancement and noise suppression based on modified homomorphic wavelet filter is first provided in the proposed approach, then for better visual observation of the detected caries, the split and merge segmentation is applied.

The rest of paper is organized as follows: In Section 2, the basics stages of the proposed approach are given; some experimental results and their interpretation are presented in Section 3 and in Section 4 - the Conclusion.

2. BASIC STAGES OF DENTAL X-RAY IMAGE PROCESSING

The flowchart of the main algorithm of the proposed approach is presented in Fig. 1.

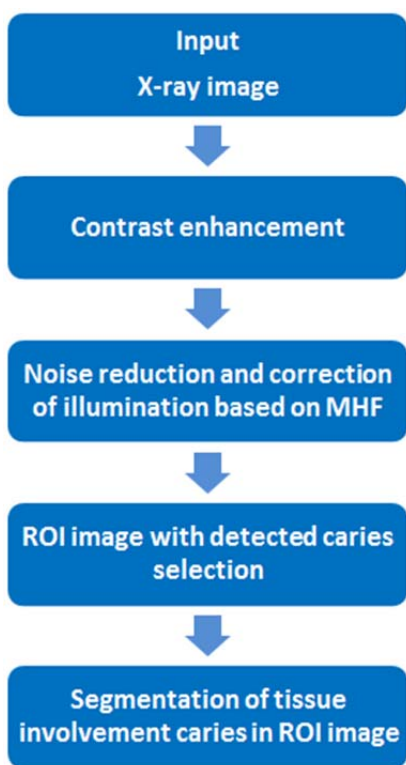


Figure 1. The flowchart of the main algorithm

The first step in the pre-processing stage is contrast enhancement. It includes CLAHE for contrast enhancement and morphological top & bottom hat operation for detail preservation capabilities [10]. The flowchart of this step is given in Fig. 2.



Figure 2. Flowchart of the contrast enhancement step

We propose to apply CLAHE to Y component of the X-ray image that is processing in YUV system as more effectiveness. We have chosen the form of histogram ('Distribution parameter') on the base of calculated PSNR and visually quality of the processed image in regard to obtain better diagnosis. Furthermore, the clip limit can be determined at the point with maximum on entropy curve of the image [11].

By using top-hat morphological operation, we can obtain details of the teeth as the edge, surface and size. An important application of top-hat transformation is in correcting some effects of non-uniform illumination. In this case, the background image is enhanced for better identification of the teeth and existing of caries. The bottom-hat operation aims to highlight the valleys of image [12]. In this case the objects are emphasized, which simplifies their segmentation from the background image. We propose to use an adaptive selection of the structuring element and its parameters for the morphological transform, which is based on calculated estimation parameters.

The next step includes noise reduction, based on modified homomorphic filter [10]. Using this filter, we convert the multiplicative Poisson noise model into additive. The modified homomorphic filter is based on wavelet packet transform (WPT). The WPT proposes more complete analysis and provides increased flexibility according to DWT. Based on the organization of the wavelet packet library, the decomposition was performed from a given orthogonal wavelets. As this number can be very large, it is important to find an optimal decomposition with respect to a conventional criterion. The classical entropy-based criterion is a common concept [13]. The Normal Shrink method is used for calculation the threshold value only of the detail sub-bands in the best shrinkage decomposition [14, 15]. This threshold can be adaptive calculated for the coefficients of each sub-bands in regard to reduce noise components and to eliminate non-uniformity luminance distribution.

The next stage is selection of region of interest (ROI), which is closed to the specific area with enamel destruction. It can be marked from the dentist.

As next, for better visual observation of the tissue involvement-based detected caries, the split and merge segmentation is applied.

3. EXPERIMENTAL RESULTS AND DISCUSSION

The formulated stages of processing are realized by computer simulation in MATLAB 8.1 environment by using IMAGE PROCESSING and WAVELET toolboxes. For the experiments, 20 X-ray images of teeth with size 1797x1441 pixels are used. The original images have been done in jpeg file format. By processing they are converted in bmp format. The images are from clinical praxis of caries superficial, caries media and deep caries (caries profunda).

Table 1 presents the obtained averaging results of processing of all images. It shows the values of the objective quantitative estimation parameters such as PSNR, Signal to noise ratio in the noised image (SNR_f), Signal to noise ratio in the filtered image (SNR_g), Effectiveness of filtration (E_{FF}).

Table 1. Experimental results in pre-processing stage

Steps of pre-processing	PSNR [dB]	SNR_f [dB]	SNR_g [dB]	E_{FF} [dB]
CLAHE	24.563	-	-	-
Morphological processing	26.268	10.235	11.887	1.652
Noise reduction	29.284	11.887	13.594	1.707

The best results for contrast enhancement using CLAHE are obtained by bell-shaped form of histogram (Rayleigh distribution).

For morphological processing (MP) with disk-shaped structuring element and especially a diamond-shaped structuring element can be obtained well-defined outlines of some tissues in the teeth, but the values of the noised components in the X-ray images are greater. We have obtained the best results with cross structuring element of size 7x7.

Our best results for noise reduction stage are obtained by Coiflet wavelet packet functions, adaptive shrinkage decomposition (best tree) on the base of the second level and minimum of the Shannon entropy criteria, when hard penalized threshold was used. By experiments, when we used Daubechies db2 [16] wavelet packet function, the log energy and energy criteria the obtained effectiveness of filtration was smaller.

The original and pre-processed X-ray images in the presence of caries superficial are shown in Fig. 3 and Fig. 4, respectively.



Figure 3. Original X-ray image with indication of caries superficial



Figure 4. Pre-processed X-ray image with indication of caries superficial

In Fig. 5 and Fig. 6 the original and pre-processed X-ray images with indication of caries media are given.



Figure 5. Original X-ray image with indication of caries media



Figure 6. Pre-processed X-ray image with indication of caries media

The same pre-processed X-ray image, but in the presence of caries profunda is shown in Fig. 7.



Figure 7. Pre-processed X-ray image with indication of caries profunda

We then apply split and merge segmentation to better visualize selected ROI images with these 3 types of caries. In Fig. 8 the selected ROI image with indication of caries superficial and its modification after segmentation is given.

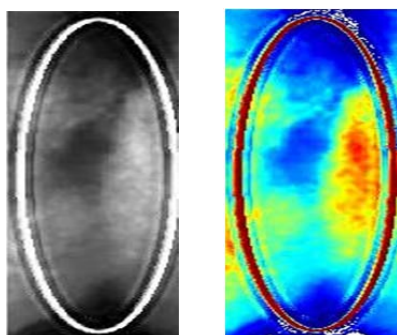


Figure 8. ROI image with caries superficial and its segmented modification

The selected ROI image with indication of caries media and its modification after segmentation is presented in Fig. 9.

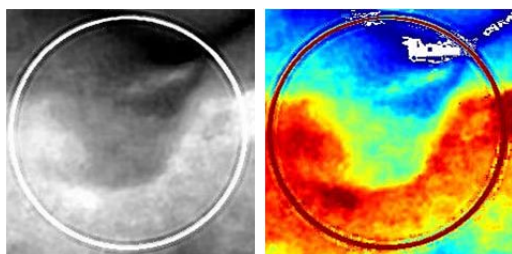


Figure 9. ROI image with caries media and its segmented modification

The indications of caries profunda in the selected ROI image and in its segmented modification are given in Fig.10.

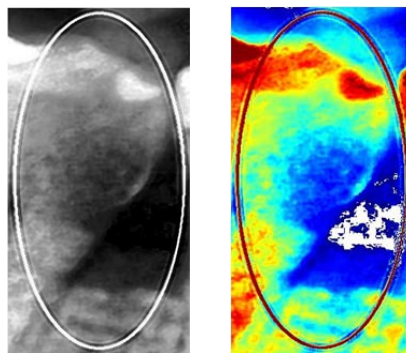


Figure 10. ROI image with indication of caries profunda and its segmented modification

We compare our experimental results with results, which are obtained by other methods for X-ray image enhancement and noise reduction, based on histogram equalization (HE), CLAHE and wavelet discrete transform (DWT) [17,18]. Table 2 contains the averaged simulation results by following methods: HE, following by morphological processing and noise reduction, based on WP transform (HE+MF+WPT); CLAHE, MF and noise reduction by homomorphic filter, based on DWT (CLAHE+MF+DWT). The compared results show, that the best results for image improvement are obtained by the proposed approach.

Table 2. Simulation results, obtained by different methods for dental image enhancement

Methods of processing	PSNR [dB]	SNR _f [dB]	SNR _g [dB]	E _{FF} [dB]
HE+MF+WPT	26.397	10.235	11.014	0.779
CLAHE+MF+DWT	27.586	10.235	12.280	2.045
Proposed method	29.284	10.235	13.594	3.359

These results have indicated that the application of the pre-processing stage visually increases the accuracy of observation the area of enamel destruction. The segmentation of the selected area can help the dentist to obtain more information about the progress of the carious process of tissue involvement-based caries.

4. CONCLUSION

In this paper, an effective approach for X-ray image processing of tissue involvement-based caries detection is proposed. The pre-processing stage, ba-

sed on contrast enhancement and noise suppression based on modified homomorphic wavelet filter is first provided. For better visual observation of the detected caries, the split and merge segmentation of selected ROI images with different type of carries is applied. The segmented area can give more information about the depth of the structural defect and the progress of the carious process.

The proposed approach can be applied for screening of early detected caries or in monitoring the disease progression. The obtained image database of detected caries can be easily used for classification, based on different classification systems.

5. ACKNOWLEDGMENTS

The authors gratefully thank Dr. Cristina Djambazova and Assist. Prof. Dr. Dimiter Alexandrov from Military Medical Academy in Sofia for the images and advices during the investigations.

REFERENCES

- [1] V. M. Castro, J. O. Katz, P. K. Hardman, A. G. Glaros, P. Spencer, "In vitro comparison of conventional film and direct digital imaging in the detection of proximal caries", *Dentomaxillofacial Radiology*, vol.36, pp. 138–142, 2007.
- [2] B. S. Enel, K. Kamburoglu, S.P. Yüksel, T. Özen and H. Avsever, "Diagnostic accuracy of different imaging modalities in detection of proximal caries", *Dentomaxillofacial Radiology*, vol. 39, pp.501–511, 2010.
- [3] P. Suetens, *Fundamentals of Medical Imaging*, Cambridge University Press, Second Edition, 2009.
- [4] G.Wang, T. Frei, M.Vannier, "A fast iterative algorithm for metal artifact reduction in x-ray CT", *Academic Radiology*, vol.7, pp.607-614, 2000.
- [5] E. Sela, S. Hartati, A. Harjoko, R. Wardoyo, M. S. Munakhir, "Segmentation on the dental periapical X-Ray images for osteoporosis screening", *International Journal of Advanced Computer Science and Applications*, vol. 4, No.7, pp.147-151, 2013.
- [6] E. Said, D. Nassar, G. Fahmy, H. Ammar, "Teeth segmentation in digitized dental X-ray films using mathematical morphology", *IEEE Trans. on Information Forensics and Security*, vol. 1, (2), pp.178-189, 2006.
- [7] P. Saputra, H. Tjandrasa, "Dental bitewing X-ray image segmentation for determining the types of teeth", in *Proc. 6th International Conference on Information & Communication Technology and Systems (ICTS)*, 2010, Surabaya Indonesia, pp.II-7-14, 2010.
- [8] S. Ahmad, M. Taib, N. Khalid, H. Taib, "An analysis of image enhancement techniques for dental X-ray image interpretation", *International Journal of Machine Learning and Computing*, vol. 2, No. 3, pp. 292-297, 2012.
- [9] D.Dimitrov, V. Georgieva, "Application of apparatus for magneto therapy in stomatology and computer treatment of X-ray images before and after therapy", *Elektronika ir elektrotehnika*, vol.3 (91), pp.39-42, 2009.
- [10] V.Georgieva, P.Petrov, A.Mihaylova, "An application of dental X-ray image enhancement", in *Proc. of 13th International Conference on Advanced Technologies, Systems and Services in Telecommunications (TELSIKS)*, IEEE Xplore Press, Nis Serbia, pp.447-450, 2017.
- [11] B. Min, D. Lim, S. Kim, J. Lee, "A novel method of determining parameters of CLAHE based on image entropy", *International Journal of Software Engineering and Its Applications*, vol.7, no.5, pp.113-120, 2013.
- [12] J. Serra, *Image Analysis and Mathematical Morphology*. Academic Press, 1988
- [13] R. Coifmann, M. Wickerhauser, "Entropy based algorithms for best basis selection", *IEEE Transaction on information theory*, vol.38, pp.713-718, 1992.
- [14] L. Kaur, S., Gupta, R. Chauhan, "Image denoising using wavelet thresholding", *Journal of Medical Engineering Technology*, vol.29, pp.208-214, 2006
- [15] M. Vetterli, S.Chang, B. Yu, "Adaptive wavelet thresholding for image denoising and compression", *IEEE Transactions on Image Processing*, vol. 9, no.9, pp. 1532–1546, 2000.
- [16] I. Cetiner, A. Var, H. Cetiner, "Classification of knot defect types using wavelets and KNN", *Elektronika ir elektrotehnika*, vol.22, no.6, pp.67-72, 2016.
- [17] N. R. Parven, M. Sathik, "Enhancement of bone fracture by equalization methods," in *Proc. of the Conference on Computer Technology and Development*, IEEE Xplore Press, Kota Kinabalu, pp. 391-394, 2009.
- [18] H. Saleh, S. Ahmed, M. Nordin, "Improving diagnostic viewing of medical images using enhancement algorithms", *Journal of Computer Science*, vol. 7, no.12, pp. 1831-1838, 2011.

SEA STATE DETERMINATION USING NORMALIZED EXPERIMENTAL ONE – DIMENSIONAL RADAR SIGNATURES AT X – BAND AND FRACTAL TECHNIQUES

G. Pouraimis¹, A. Kotopoulos¹, N. Ampilova², I. Soloviev²,
E. Kallitsis¹ and P. Frangos¹

¹School of Electrical and Computing Engineering, National Technical University of Athens,
9, Iroon Polytechniou Str., 157 73 Zografou, Athens, Greece

Tel.: +30 210 772 3694; FAX: +30 210 772 2281; e-mail: pfrangos@central.ntua.gr

² St. Petersburg State University, Computer Science Department,

e-mail : n.ampilova@spbu.ru, i.soloviev@spbu.ru

Abstract

This paper presents a novel method of sea state characterization using the 'Variance σ^2 ' and 'Fractal Dimension - FD' criteria which are applied to experimental Synthetic Aperture Radar (SAR) one – dimensional signatures (range profiles) in frequency domain. The above approaches are applicable to normalized mean of backscattered signal from sea surface. This analysis is performed by using real recorded sea clutter radar data which provided to our research group by SET 215 Working Group on 'SAR radar techniques'. The Fractal Dimension criterion uses the 'blanket' technique providing sea state characterization from SAR radar range profiles. This method is based on the calculation of the area of a 'blanket', of normalized mean of range profile spectrum. The main idea concerning both 'Variance' and 'Fractal Dimension' proposed techniques is the fact that SAR radar range profiles corresponding to different sea states yield different values of variance and fractal dimension, namely 'turbulent sea' yields range profiles with larger variance in time and frequency domain and larger fractal dimension of signal spectrum because of the more 'anomalous behavior' of the range profiles in those cases. As a result, two sea state characterization techniques for two different sea states (turbulent and calm sea) are presented in this paper.

1. INTRODUCTION

Fractal geometry was introduced by Mandelbrot [1] and has been gaining importance in recent years as a mathematical model for different applications, such as image analysis and classification [2], applied electromagnetism etc. [3] - [7]. Fractals is a very effective method for describing physical objects with a high degree of geometrical complexity which have fine structures (details on arbitrarily small scales) and they are too irregular to be described by Euclidean geometry, appearing self-similarity at different scales [5]. The main characteristic of fractals is the self-similar structure at many different scales. Consequently, fractals can describe a variety of geometrical complexity of data and also finds applications in characterizing scattering from fractal surfaces [5].

Previous studies indicate that the fractal surfaces permit form expressions for the scattering coefficients under the Kirchhoff approximation [9] and using a fractal function a rough surface scattering can be modelled [7], [8]. For several years great effort has been devoted to the study of clutter anal-

ysis based on the fractal characterization of the signal [5], [6] and [9] - [11].

The main objective of this paper is to examine the sea state characterization problem using an analysis of real radar backscattered signals from the sea surface (sea clutter), aiming to estimate the sea state. This paper presents two methods for sea state characterization by using: first, the variance of the mean spectrum of the range profiles and, second, the calculation of the fractal dimension of the range profiles [11]. These methods have been applied in this paper to real experimental Synthetic Aperture Radar (SAR) data [11].

Previous studies used the same experimental one – dimensional radar signatures to provide useful information about sea state characterization [12]. The objective was to use the fractal dimension of the experimental radar signatures as an additional tool for sea surface characterization.

The sea clutter radar data that were used collected during the 'NEMO 2014' trials in Taranto, Italy, using an FFI (i.e. 'Norwegian Institute of Defense', Oslo, Norway) PicoSAR X-band radar as input to a

specific SET Working Group. The trial took place in the Taranto bay in southern Italy on 23 and 24 September 2014 where the first day the weather was quite windy, creating a turbulent sea, correlated to the second day, during which the sea surface was almost calm.

2. PROBLEM GEOMETRY AND STATEMENT

The geometry of sea state characterization problem is shown in Fig. 1. The helicopter flying vertically while maintaining its position on latitude and longitude fixed, used a PicoSAR radar transmitting to the sea, radar pulses and receiving data measurements. The experiment focused on up-wind direction towards the sea which means that the azimuth angle of the radar was with high sampling density in grazing angle.

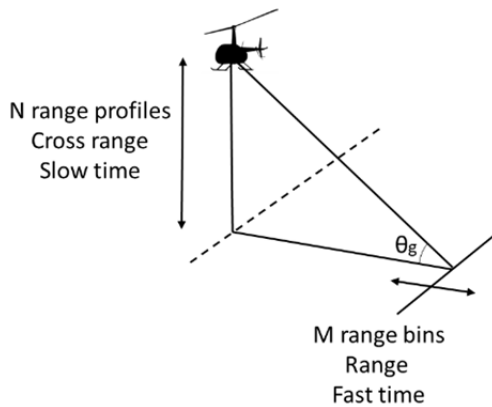


Figure 1. Geometry of the problem

The first day (23/9/2014) of the trial the wind speed was 10-12m/s. The radar azimuth (antenna beam) kept on the direction of the wind (upwind) within a 20° window in the horizontal (azimuthal) direction. The grazing angles as the helicopter was rising vertically ranged from 3° to 55° and the measurement time of the recorded grazing angle was approximately 5 minutes. For this reason it was assumed that the wind and sea conditions were almost constant during this short period.

The second day (24/9/2014) of the experiment, the wind speed was very low (1-2 m/s) and sometimes without wind. The sea clutter data was recorded for grazing angles from 4° to 54° with a slight drift in azimuth pointing angle of the bore sight of no more than 20 degrees.

For the data used in our analysis the PicoSAR radar have the following characteristics: pulse width 12μs, bandwidth 150 MHz, PRF 1 kHz and operating frequency $f_s = 9.4\text{GHz}$ (X Band). The range to

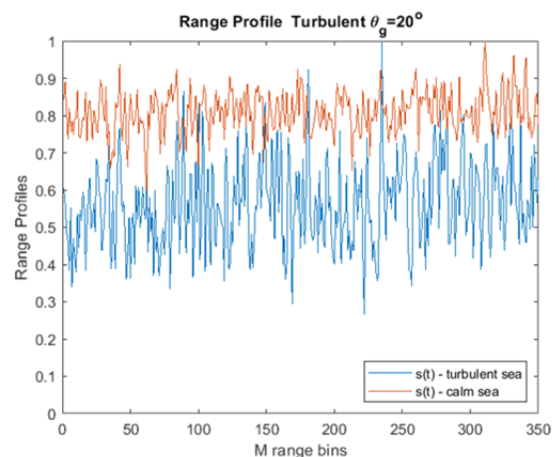
the scene center of the trial was 1850m for all grazing angles.

In our previous study of sea state characterization [12] we indicated a novel method of characterizing the sea surface using the 'Mean Fractal Length (MFL)' criterion which was applied to the same experimental Synthetic Aperture Radar (SAR) one – dimensional range profiles that we used in this research, applied on time domain.

However, several practical questions arise when dealing with our analysis to characterize a backscattered signal embedded in noise. To deal with this issue, we present an approach which initially implement averaging of the range profiles for avoiding noise. Determining how many samples of range profiles are required to derive a reasonably accurate estimate of the signal and after running simulations we chose N to be 50 range profiles to ensure that was quite enough to give an accurate result. Then, we normalized the mean signal range profile in range from 0 to 1 and transformed the backscattered signal in frequency domain.

In order to verify the validity of the sea state characterization method, we carried out several experiments in plenty of grazing angle from 5° to 32° as for angle greater than 32° it is noticed a strange behaviour of the signal, that may be caused by complicated physical phenomena and actual antenna beamwidth considerations.

Fig. 2 shows representative normalized mean radar backscattered radar signals for N=50 range profiles (1D radar signatures) in time domain as shown in figure on the top and frequency domain (power spectra) at bottom figure, for 'Day 1' (23-9-2014, 'turbulent sea') and 'Day 2' (24-9-2014, 'calm sea'), at grazing angle of $\theta_g = 20^\circ$.



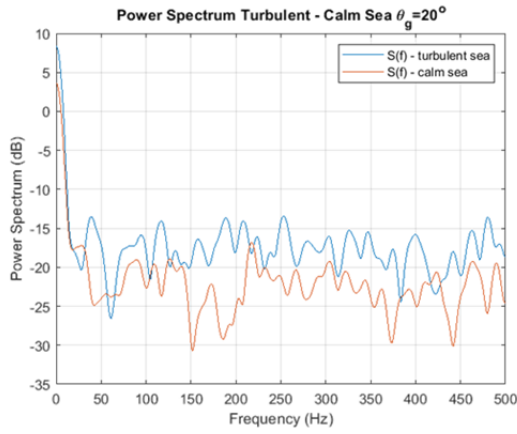


Figure 2. Representative PicoSAR radar range profiles at grazing angle $\theta_g = 20^\circ$ for Day 1 (turbulent sea) and Day 2 (calm sea): (i) time domain (ii) frequency domain

As follows from Fig. 2(i), on 23 September 2014 the range of the corresponding values is approximately from 0.3 to 1. The power spectrum of these signals was estimated to determine the power indices.

Moreover during the following day of 24 September 2014, for the same grazing angles of 20° , but for 'calm sea' in this case, the range of values of the range profiles is approximately from 0.6 to 1.

The 'Variance (σ^2)' criterion is used for the sea state determination, which computes the variance of the normalized mean signal in time and frequency domain, for turbulent and calm sea, and at grazing angles from 5° to 30° (increasing every 5°). The Variance (σ^2) is given by eq. (1):

$$\sigma^2 = \frac{1}{f_{max}} \int_{f=0}^{f_{max}} (S(f) - S_m)^2 df \quad (1)$$

The 'Fractal Dimension' criterion is the second method that used for the sea state estimation which computes the fractal dimension of the normalized mean range profile in frequency domain, for turbulent and calm sea, and at grazing angle from 5° to 30° as well. The 'Fractal Dimension' is calculated using the 'blanket technique' that has been described briefly in previous study [12].

This criterion was chosen as fractal dimension is a measure of how much space a geometrical set fills [5]. Fractal dimension is a characteristic for fractals description and classification [13] as it makes meaningful the measurement of metric parts of fractal curves, which one of them is their length. The 'blanket' technique provides useful information for SAR image classification [2] and sea state characterization [12].

The 'upper and lower curves' of the 'radar range profiles' are indicatively shown at Fig. 3, for iterations $\delta=20$ of the normalized mean of the backscattered signal on frequency domain (here for grazing angle $\theta_g=20^\circ$). To be noticed that, δ represents the 'iteration number', or, equivalently, the 'resolution'.

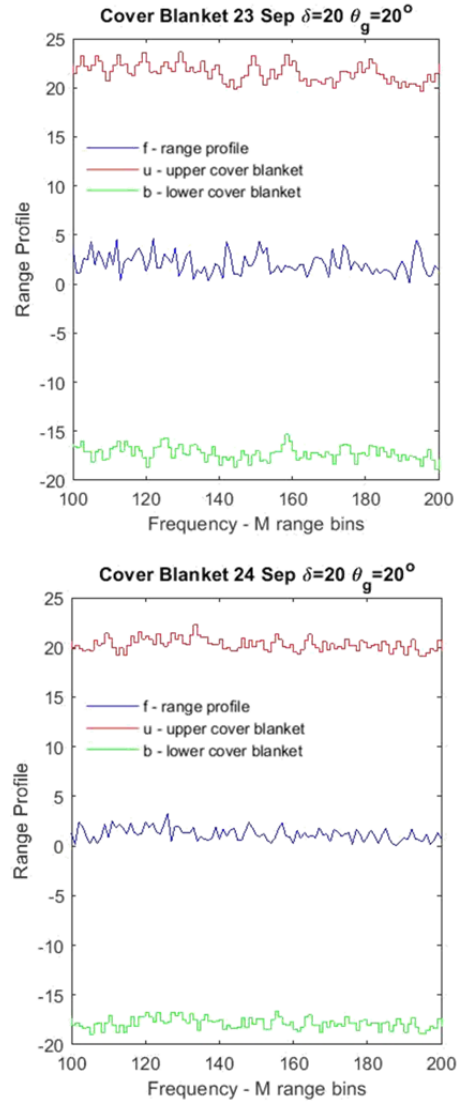


Figure 3. One-dimensional (1D) sea clutter signal and the 'upper' and 'lower' curves of the strip for iteration number $\delta=20$.

3. SEA STATE CHARACTERIZATION RESULTS

The 'Variance (σ^2)' and 'Fractal Dimension' criteria are used for characterization of the sea state. The 'Variance (σ^2)' criterion computes the variance of normalized mean signal in time and frequency domain of $N=50$ range profiles, according to eq. (1). Then, numerical calculations similar to the above were performed, and the results are presented at Table I.

TABLE I. Variance (σ^2) values results for different sea states and grazing angles

Day Angle	Frequency Do- main		Time Domain	
	Turb	Calm	Turb	Calm
5°	0.288	0.043	0.010	0.003
10°	0.455	0.061	0.015	0.003
15°	0.591	0.055	0.016	0.004
20°	0.386	0.044	0.014	0.003
25°	0.404	0.015	0.014	0.002
30°	0.362	0.023	0.013	0.002

The results of Table I show that the 'variance' values of the radar normalized mean of N=50 range profile in time and frequency domain spectra during the turbulent sea state are significantly larger than the corresponding values at calm sea.

The 'Fractal Dimension' criterion computes the fractal dimension of the normalized mean for N=50 range profiles in frequency domain, using 'blanket' technique as briefly described in our previous research [12]. The numerical calculations were performed, and the results are presented at Fig. 4 for grazing angles of 10° and 25°. Similar results measured for the grazing angles from 5° to 30°.

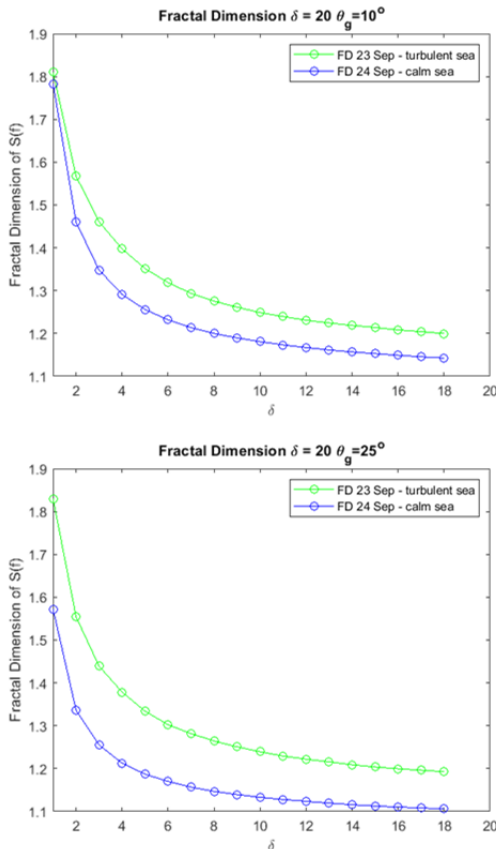


Figure 4. Fractal Dimension $F_D(\delta)$ as a function of resolution δ for grazing angles (i) 10° (upper figure) and (ii) 25° (lower figure).

The results of Fig. 4 show that the fractal dimension values of radar normalized mean of N=50 range profile spectra during the turbulent sea state are significantly larger than the corresponding values at calm sea.

Finally, the Sea State Index (SSI) is calculated for both 'Variance' and 'Fractal Dimension' criteria. The sea state indexes (SSI) use the values for calm sea as reference. The corresponding results for SSI are shown at Table II, below.

TABLE II. Sea State Index (SSI) for 'Variance' and 'Fractal Dimension' criteria for different grazing angles

Angle	Frequency Domain		Time Do- main
	Variance	Fractal Dimension	Variance
5°	6.604	1.033	2.965
10°	8.894	1.058	4.686
15°	10.645	1.034	3.813
20°	8.670	1.056	4.216
25°	25.508	1.111	6.590
30°	15.297	1.073	5.042

From the above numerical results we conclude that the 'variance' and 'fractal dimension' criteria are suitable for 'radar range profile data' in the frequency domain, while the 'variance' criterion only is suitable for sea state determination in the time domain.

4. CONCLUSIONS

This paper proposes the use of two criteria for the characterization of the sea state using *normalized* experimental 1D radar signatures (range profiles). The corresponding recorded sea clutter radar data were collected during the 'NEMO 2014' trials in Taranto, Italy, 23-24/9/2014. An X-band PicoSAR airborne radar was used for that purpose by FFI (i.e. 'Norwegian Institute of Defense', Oslo, Norway)

Concerning the 'Fractal Dimension' criterion, described above, the fractal geometry theory and, especially, the 'blanket' method was applied to the analysis of the sea clutter radar data that had been recorded from sea surfaces. The experiment measured back-scattered signals from sea surface for turbulent and calm sea. The sea clutter radar data initially implemented averaging for avoiding noise and then normalized and transformed in frequency domain.

The use of 'Variance σ^2 ' and 'Fractal Dimension' criteria described above were found to be suitable criteria for sea state determination, as described above.

5. FUTURE RESEARCH

In our future related research, we intend to establish the above criteria in a more accurate fashion. Furthermore, we intend to further establish more accurate sea state characterization techniques in a variety of sea state conditions, if possible.

6. ACKNOWLEDGMENT

The authors (GP, AK and PF) would like to thank SET-215 Working Group, and FFI Institute (i.e. 'Norwegian Institute of Defense', Oslo, Norway), in particular, for providing to us the real recorded sea clutter radar data which were collected during the 'NEMO 2014' trials in Taranto, Italy, and are shown in Figs. 2 above.

Furthermore, the authors acknowledge the support by the 'International Mobility Program', National Technical University of Athens (NTUA), Greece, which facilitated the scientific collaboration between the authors of this paper in the area of 'fractal techniques'.

REFERENCES

- [1] B. Mandelbrot, *The Fractal Geometry of Nature*, New York: W. H. Freeman and Company, 1977.
- [2] A. Malamou, C. Pandis, P. Stefanias, A. Karakasiliotis, D. Kodokostas and P. Frangos, "Application of the modified fractal signature method for terrain classification from synthetic aperture radar images," *Electronics and Electrical Engineering Journal*, vol. 20, no. 6, DOI:10.5755/j01.eee.20.6.7281, pp.118-121, 2014.
- [3] K. J. Falconer, *Fractal Geometry: Mathematical Foundations and*, West Essex: J. Wiley and Sons, 1990.
- [4] Y. Tang, H. Ma, D. Xi, X. Mao and C. Suen, "Modified fractal signature (MFS): a new approach to document analysis for automatic knowledge acquisition," *IEEE Trans. Knowledge and Data*, vol. 9, no. 5, DOI:10.1109/69.634753, p. 747-762, 1997.
- [5] T. Lo, H. Leung, J. Litva and S. Haykin, "Fractal characterisation of sea-scattered signals and detection of sea-surface targets," *IEE Proceedings F (Radar and Signal Processing)*, vol. 140, no. 4, DOI:10.1049/ip-f-2.1993.0034, p. 243 - 250, 1993.
- [6] D. Jaggard and X. Sun, "Scattering from fractally corrugated surfaces," *Journal of the Optical Society of America A*, vol. 7, no. DOI:10.1364/JOSAA.7.001131, pp. 1131-1139, 1990.
- [7] A. Kotopoulis, A. Malamou, G. Pouraimis, E. Kalitsis and P. Frangos, "Characterization of rough fractal surfaces from backscattered radar data," in *CEMA 2016*, Sofia, DOI:10.5755/j01.eie.22.6.17226, 2016.
- [8] G. Pouraimis, A. Kotopoulis, E. Kallitsis and P. Frangos, "Characterization of Three - Dimensional Rough Fractal Surfaces from Backscattered Radar Data," *Elektronika ir Elektrotechnika*, vol. 23, no. 4, DOI: 10.5755/j01.eie.23.4.18721, pp. 45-50, 2017.
- [9] Berizzi and Dalle Mese, "Fractal analysis of the signal scattered from the sea surface," *IEEE Trans. Antennas Propagat.*, vol. 50, no. DOI: 10.1109/8.761073, p. 324-338, 1999.
- [10] J. Chen, K. Lo, H. Leung and J. Litva, "The use of fractals for modeling EM waves scattering from rough sea surface," *IEEE Trans. on Geoscience*, vol. 34, no. 4, DOI:10.1109/36.508413, p. 966-972, 1996.
- [11] S. Peleg, J. Naor, R. Hartley and D. Avnir, "Multiple resolution texture analysis and classification," *IEEE Trans. Pattern Analysis and*, Vols. PAMI-6, no. 4, DOI:10.1109/TPAMI.1984.4767557, p. 518-523, 1984.
- [12] G. Pouraimis, A. Kotopoulis, T. Lympelopoulis, I. Soloviev, N. Ampilova and P. Frangos, "Sea State Characterization usng Experimental 1D Radar Signatures at X-Band and Fractal Techniques," in *CEMA'18 conference*, Sofia, <https://pure.spbu.ru/ws/portalfiles/portal/35296037/1.pdf>, 2018.
- [13] P. Maragos and F. Sun, "Measuring the Fractal Dimension of Signals: Morphological Covers and Iterative Optimization," *IEEE Transactions on Signal Processing*, vol. 41(1), no. DOI:10.1109/TSP.1993.193131, pp. 108-116, 1993.
- [14] D. Jaggard, A. Jaggard and P. Frangos, "Fractal electrodynamics: surfaces and superlattices," *IEEE Press - Frontiers in Electromagnetics*, vol. 709, pp. 1-47, 2000.
- [15] N. Ampilova, E. Gurevich and I. Soloviev, "Application of modified fractal signature and Regny spectrum methods to the analysis of biomedical preparation images," in *Int. Conf. CEMA*, Sofia, <http://diffjournal.spbu.ru/pdf/ampilova2.pdf>, 2011.

ON THE APPLICATION OF MULTIFRACTAL METHODS FOR THE ANALYSIS OF SEA SURFACE IMAGES RELATED TO SEA STATE DETERMINATION

N. Ampilova, I. Soloviev,

St. Petersburg State University, Comp. Sci. Dept.
n.ampilova@spbu.ru, i.soloviev@spbu.ru

Apostolos Kotopoulos, George Pouraimis, Panayiotis Frangos

School of Electrical and Computer Engineering
National Technical University of Athens, Greece

pfrangos@central.ntua.gr

Abstract

Digital images may register states of a process, and image analysis help us to study this process and its peculiarities. In spite of the fact that there are a lot of textbooks on techniques of image analysis, any new problem may requires a new method. Last decades fractal and multifractal methods are often used to analyze high resolution images having complex textures. In many cases fractal characteristics may be considered as classifying signs for further clustering. In this paper we present two multifractal methods. The first method allows us to obtain multifractal spectra and decompose an initial image into the union of nonintersecting sets. The second one is based on the transformation of an initial measure distribution under so called "direct multifractal transform" and calculation of information dimensions of measure supports. The examples of application of these techniques are given for various kinds of sea surface images.

1. INTRODUCTION

Now the methods of fractal and multifractal analysis are widely used to analyze images with complex structure. Such images are often fractals or multifractals. Fractal sets have a self-similarity property and may be described one numerical characteristic — fractal dimension. Multifractal sets are unions of several fractal subsets, which of them has its own fractal dimension, being these subsets are arranged in a complex intertwined manner. Hence a common characteristic for multifractals is multifractal spectrum — the set of fractal dimensions of its subsets. Our experience in analyzing biomedical preparation images (in [1] we calculated Rényi spectra for images of pharmacological solutions of Ag, and in [2,3] we applied such methods for sensitive crystallization images) testifies that the good separation of spectra results in successful classification of similar images.

In this work we consider two methods for calculation of multifractal characteristics for digital images: a method based on calculation so called density function, which is calculated for each pixel and characterizes intensity changes in its neighbourhood, and calculation of the set of information dimensions both for a given spectrum and its modi-

fied variants which are obtained by a renormalization of a given measure. Additionally, in this method we calculate the spectrum of averaged exponents of singularity. Thus to characterize an image we have 2 spectra. The combining of two methods increases the possibility for classification of images.

2. MULTIFRACTAL SPECTRUM BY USING DENSITY FUNCTION

We consider a special density function [4] to calculate the singularity power for every pixel. Then we combine all the pixels with close values of density function, which results in partition of the image on the subsets — so called level sets. For each level set we calculate its fractal dimension.

Let μ be a measure defined through pixel intensities for a given digital image. For $x \in R^2$ we denote $B(x, r)$ a square of length r with center x . Let $\mu(B(x, r)) = kr^{d(x)}$, where $d(x)$ is so called the local density function of x , and k some constant. Taking several values for r we have

$$d(x) = \lim_{r \rightarrow 0} \frac{\log \mu(B(x, r))}{\log r}$$

The density function measures the non-uniformity of the intensity distribution in the square $\mathbf{B}(\mathbf{x}, \mathbf{r})$. The set of all points \mathbf{x} with local density α is a level set $E_\alpha = \{\mathbf{x} \in \mathbf{R}^2: \mathbf{d}(\mathbf{x}) = \alpha\}$. In practice, not to increase the number of level sets, one really consider the sets $E(\alpha, \varepsilon) = \{\mathbf{x} \in \mathbf{R}^2: \mathbf{d}(\mathbf{x}) \in [\alpha, \alpha + \varepsilon]\}$.

The set of fractal dimensions of E_α is the multifractal spectrum $f(\alpha)$.

3. USING STATISTICAL SUM

It is usually assumed that an image is partitioned by cells with size l , the number of cells is $N(l)$ and the measure of i -th cell is $p_i(l) \sim l^{\alpha_i}$. Consider the statistical sum $(q, l) = \sum_{i=1}^{N(l)} p_i^q(l)$ and the sequence of measures $\mu(q, l) = \{\mu_i(q, l)\}$ generated from the initial measure by the direct fractal transform $\mu_i(q, l) = \frac{p_i^q(l)}{\sum_{i=1}^{N(l)} p_i^q(l)}$. The method was proposed in [5] and is based on the calculation of information dimension of a measure support M by the formula

$$\dim M = - \lim_{N \rightarrow \infty} \frac{\sum_{i=1}^N p_i \ln p_i}{\ln N}$$

The direct multifractal transform results in a transformation of the initial measure by using statistical sum, and hence it depends on q as well. For any measure from the generated sequence one may calculate the singularity power averaged over the measure and the fractal dimension of the support of the measure corresponding to this singularity power. Hence we obtain the averaged singularity spectrum $\alpha(q)$, and the fractal dimension of the support of the measure $f(q)$ as functions of the parameter q . Eliminating q one can obtain the relation between singularity values and fractal dimensions of corresponding subset.

For each measure $\mu(q, l)$ one can calculate information dimension of its support. As q changes, we have a set $f(q)$ of information dimensions of $\mu(q, l)$ supports, where

$$f(q) = \lim_{l \rightarrow 0} \frac{\sum_{i=1}^N \mu_i(q, l) \ln \mu_i(q, l)}{\ln l} = \lim_{l \rightarrow 0} \frac{f(q, l)}{\ln l}.$$

We also calculate averaging exponents over the measure $\mu(q, l)$, i.e.

$$\begin{aligned} \sum_{i=1}^N \alpha_i \mu_i(q, l) &= \frac{\sum_{i=1}^N \ln p_i(l) \mu_i(q, l)}{\ln l} \\ &= \frac{\alpha(q, l)}{\ln l}, \end{aligned}$$

and then the limit $\alpha(q)$ of these averagings when $l \rightarrow 0$. Hence, we obtain

$$\alpha(q) = \lim_{l \rightarrow 0} \frac{\alpha(q, l)}{\ln l}.$$

Such a method allows us to obtain the set of dimensions $f(q)$ and the set of averaging exponents $\alpha(q)$ as functions of the parameter q .

In practice, to obtain the above values we should do the following. For every q we take several values of variable l , calculate sets of points $(\ln l, f(q, l))$ and $(\ln l, \alpha(q, l))$ respectively. Then, by using the least square method, we determine the approximate values of $f(q)$ and $\alpha(q)$. Thus, we have the set of information dimensions of the supports of the measures that are obtained from the initial measure by the direct multifractal transform. We applied this method in [6], to analyze biomedical preparation images and in [7] to study crystallization images.

4. NUMERICAL EXPERIMENTS

Now we consider images of calm (1) and disturbed (2) sea surfaces.



(1) calm sea surface



(2) disturbed sea surface

Figure 1. Optical images of sea surface related to sea state determination

Values of density function lie in diapason [1.73, 2.23] for 1) and [1.52, 2.42] for 2). We note that wider interval corresponds to more complex structure of the image. Level sets were constructed with step 0.1. The graphs of multifractal spectra are given below.

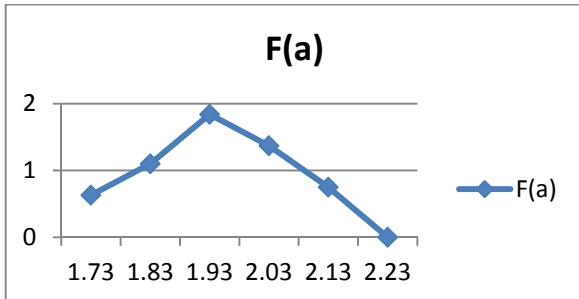


Figure 2 (a). Multifractal spectrum for image 1)

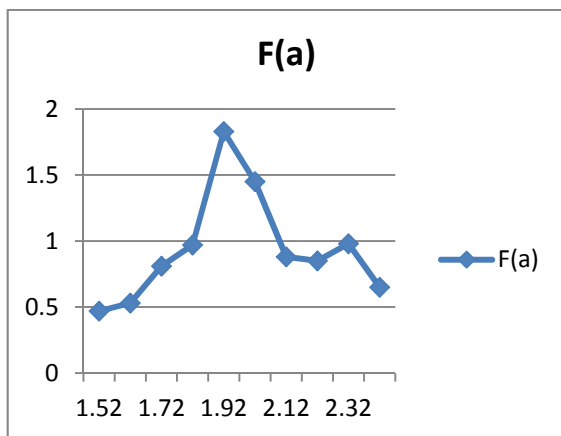
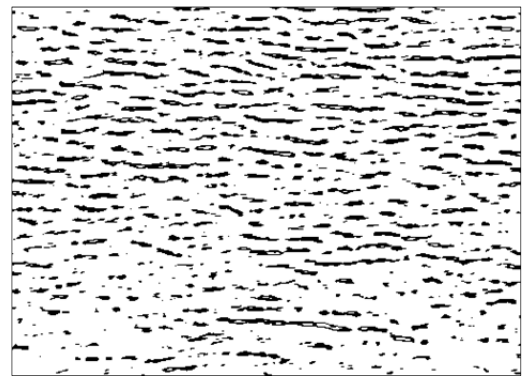


Figure 2 (b). Multifractal spectrum for image 2)

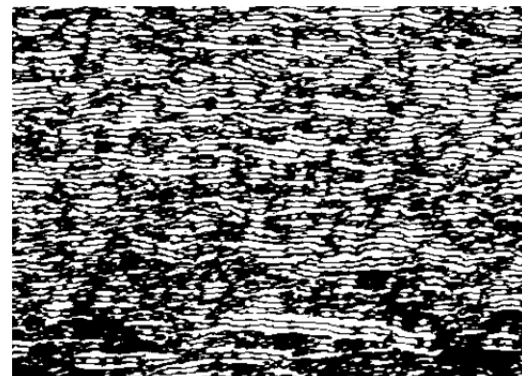
Level sets for image 1) are shown below. These sets illustrate a decomposition of an image on non-intersecting subsets. Each subset contains pixels having density function value in an interval $[a, a+0.1)$, where $a=1.73, 1.83, 1.93, 2.03, 2.13$. Thus the number of subsets shown equals the number of intervals between values on OX axis. We see that image c) has the most intensive density, and on the graph we see that this subset has the maximal fractal dimension.



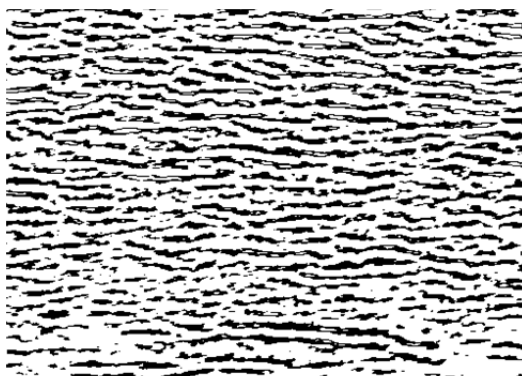
a)



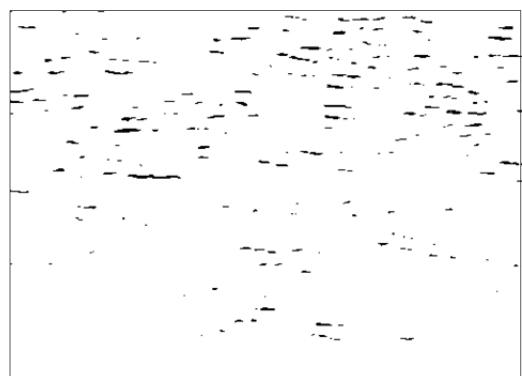
b)



c)



d)



e)

Figure 3. Level sets for image 1): the decomposition of the image on nonintersecting subsets

The corresponding graphic show values of fractal dimensions of these sets.

The application of the second method results in the graphics shown on Fig.4

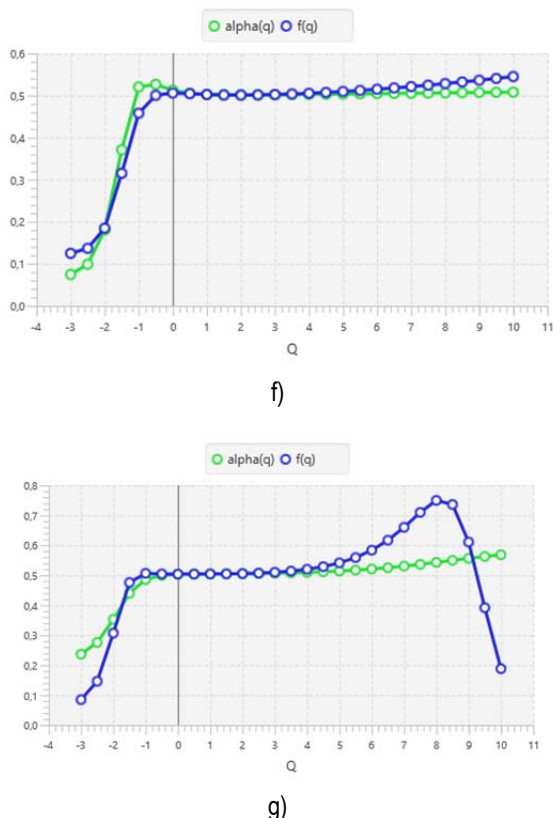


Figure 4. Graphs of singularity and information dimensions for calm sea (f) and disturbed sea (g)

5. CONCLUSION

The results of numerical experiments show that the methods applied may be useful for analysis of sea surface images and sea state determination, since graphs of multifractal spectra look quite different for different types of sea surfaces. In the near future the authors intend to investigate more precise criteria based on the methods described to determine sea states.

6. ACKNOWLEDGMENTS

The authors (Apostolos Kotopoulos, George Pouraimis and Panayiotis Frangos) would like to thank FFI

Institute of Oslo, Norway, for the two (2) optical images of the sea surface, related to sea state determination (images obtained by FFI during 'NEMO 2014' trials in Taranto, Italy, September 2014). Furthermore, the authors acknowledge the support by the 'International Mobility Program', National Technical University of Athens (NTUA), Greece, which facilitated the scientific collaboration between the authors of this paper in the area of 'fractal techniques'.

REFERENCES

- [1] E. Gurevich, N. Ampilova, I. Soloviev. On a natural-science investigation of the ultralow doses effect, Proc. 8 Int. Conf. CEMA13, 17-19 Oct. 2013, Sofia, Bulgaria. p. 85-88.
- [2] N. Ampilova, I. Soloviev. Fractal analysis methods in investigation of low doses effects. Proc. 12 Int. Conf. CEMA17, 12-14 Oct. 2017, Sofia, Bulgaria, p. 10-14. ISSN: 1314-2100, Pub. KING 2001, Sofia.
- [3] N. Ampilova, E. Kulikov, V. Sergeev, I. Soloviev. Fractal analysis methods in investigation of biomedical preparations images. Differential equations and control processes, 1, 2018, p. 109-125,
<http://www.math.spbu.ru/diffjournal/pdf/ampilova3.pdf> (in Russian)
- [4] Yong Xu, Hui Ji, Cornelia Fermuller, Viewpoint Invariant Texture Description Using Fractal Analysis, Int. J. Comp. Vis, 2009, 83, p. 85-100.
- [5] Ashvin B. Chhabra, Charles Meneveau, Roderick V. Jensen and K. R. Sreenivasan. Direct determination of the $f(\alpha)$ singularities spectrum and its application to fully developed turbulence — Physical Review A, Volume 40, Number 9, November 1, 1989. p. 5284-5294.
- [6] N. Ampilova, V. Sergeev, I. Soloviev. On some questions concerning to the multifractal spectra calculation, Proc. 10 Int. Conf. CEMA15, 15-17 Oct. 2015, Sofia, Bulgaria. p. 14-17.
- [7] N. Ampilova, I. Soloviev, J. Barth. Application of fractal analysis methods to images obtained by crystallization modified by an additive, Journal of Measurements in Engineering, Vol. 7, Issue 2, 2019, p. 48-57. <https://doi.org/10.21595/jme.2019.20436>.

ANALYSIS OF IMAGES OBTAINED BY CAPILLARY DYNAMOLYSIS METHOD

I. Murenin, N. Ampilova

St. Petersburg State University, Comp. Sci. Dept.

imurenin@gmail.com, n.ampilova@spbu.ru

Abstract

Now the methods of computational image analysis allow us to automate the techniques of routine analysis of digital images in various fields of research. The capillary dynamolysis method reflects the spectrum of organic matter in a biological sample. Last decades it is widely applied in ecology and food industry to study the properties of soil and products.

This paper presents an approach to the analysis and classification of soil samples obtained by capillary dynamolysis. Detectors of brightness differences help to define a special boundary curve on the image, and distances from the central point of the image to the points on the curve are the classifying signs for the image under study.

A set of 128 images is divided into 8 classes, which are used to assess the qualitative properties of soil samples. Computed features make it possible to distinguish samples of the soil of the worst quality and to compare images from different classes

1. INTRODUCTION

From the middle of the last century picture forming methods for investigating organic cultivation products are widely used. They are based on the inner structure of an explored sample which depends on biological processes under study. There are three classes of such methods: cupric chloride crystallization (called also biocrystallization), capillary dynamolysis, and circular chromatography. The main principle of the methods is to place some metal salts in water solution and perform the reaction with the substance to be analyzed. In the capillary dynamolysis method the reaction is taking place on vertically located filter paper with 0.5% solution of a metal salt, usually silver nitrate and ferrous sulfate. The paper absorbs the solution of the salt by capillary taking up, after which 0.1% sodium hydroxide solution with the sample extract is added. The filter paper then is dried and exposed by indirect sunlight. The result is the image with specific patterns and colors. Its characteristics allow us to make assumptions about the quality of samples and type of producing environment.

Picture forming methods have practical applications in the development of agriculture and estimation of plant food quality based on its organic properties. Also they provide an analysis of soil samples. Traditionally trained expert groups are involved in image analysis. They evaluate obtained images through approved criteria for describing differences between tested samples. But with growth of contemporary computational systems the necessity of applying

automatic image analysis methods arises. Expert evaluation requires significant practical experience and a lot of time. More than that, a unified methodology for estimating sample properties does not exist. In this way, computational image analysis is able to increase the objectivity and quality of the evaluation results and allow processing large volumes of data.

This article presents an approach to the analysis of images obtained by capillary dynamolysis method. It is based on the assessment of shape and geometrical properties of a specific region of an image considered. The main steps include the image filtering for noise reduction and retrieval of key information, searching for interest area by applying special detectors based on lines approximation, and forming a final feature set depending on the image geometrical properties. The obtained image signs allow us to create a unique description for each tested sample. The paper is structured as follows. Section 2 describes existing approaches to analysis of images obtained by the capillary dynamolysis and other picture forming methods. Section 3 presents major points of the proposed approach for target images analysis. Section 4 discusses results and directions of a future work.

2. RELATED WORKS

Visual evaluation and computational analysis are commonly used to investigate images obtained by capillary dynamolysis and other picture forming methods. Computational image analysis is a non-

trivial task, so it requires an individual line of attack which takes into account singularities of image formation.

The paper [11] describes key properties of images obtained by capillary dynamolysis and gives prescriptions for its visual interpretation. In [5] the authors present an approach to visual analysis of wheat images, which is derived from the experiments with capillary dynamolysis and biocrystallization. They use statistical methods for classifying target samples based on visually detected features. Several examples for image computational analysis are introduced for biocrystallization, but not for the capillary dynamolysis. The paper [4] discusses applications of capillary dynamolysis, biocrystallization and circular chromatography for analysis of quality and classification of grape and grape juice samples.

In [1] computational analysis methods are applied to examine impact effects of homeopathic drugs on plants. Images for source samples are generated through biocrystallization, their features are obtained by texture and variance analysis. Additionally, the authors use data representing physical properties of experiments.

The paper [7] presents an approach to visual and computational analysis of soil images acquired by the circular chromatography method. Areas of interest are selected randomly in central zone of an image which is previously transformed to grayscale, then the entropy of texture features in this area is computed. Results are combined with visual characteristics, and on this basis final image features are formed.

In [12] the authors describe a method based on neural networks to analyze images obtained by capillary dynamolysis. They notice that in literature there are no approaches to computational analysis of target images. The task of binary classification of organic and non-organic food images is considered. A source image is transformed to grayscale and convolved to a one-dimensional vector. To reduce the dimension of the vector the Gram-Charle coefficients are computed, which form the resultant feature set. It should be noted that at the moment there are few methods of computational image analysis, because visual interpretation acquires more wide using both experience and practical applications.

The papers [9,10] describe our previous results concerning to analysis of images obtained by the

capillary dynamolysis method. The proposed approach for feature selection was described in [9]. In paper [10] we presented the results of evaluation and clusterization on the dataset containing 31 images of soil.

3. THE ANALYSIS OF IMAGES OBTAINED BY THE CAPILLARY DYNAMOLYSIS METHOD

This method may be applied to obtain images when analyzing liquids, soils, food, plants [4,7]. One should note that digital images of different objects may have rather similar structures, which prevents us from visual comparing [11]. Besides that in practice we often have to deal with a small number of images. Our goal is to reveal characteristics of images obtained by the capillary dynamolysis method and use them as classifying signs of the objects under study. The proposed approach allows us to find the most informative areas on an image and define their geometric properties, such that these properties are unique for an object to a great extent. To find these areas and delete noise we use the filtration algorithms based on differential operators. We apply special detectors to find the points of the brightness difference, which helps to find the boundary of the area of interest. Then we calculate the distances from the centum of the image to the boundary. These distances are used as characteristics of the image. For testing the method, the experimental data consisting from 128 soil images obtained by capillary dynamolysis method [2] were used. All images have holes in the center and two areas – brawn and gray. The boundary of the fist area is smooth, and the second one has sharp edges. The example of an image obtained by the capillary dynamolysis method is shown on the Fig. 1.



Figure 1. Image of soil sample obtained by the capillary dynamolysis method

In experiments each image corresponds to one of metal salts: Ag, Au, Pb, Sn, Fe, Cu, Hg. To analyze biological preparation images one often apply spectral analysis [3] and statistical methods [6]. For data described above we calculated spectral signs and second order statistics. But the experiments showed that for different samples results differ on 10-20%, which is insufficient for further classification. Hence these methods should not be applied for unique identification of such objects. Thus, the demand arises to filter noise and reveal the most informative signs for classification. In [11] the methods of visual interpretations of chromatogram are described. They may be applied for analysis of soil images obtained by capillary dynamolysis. The author underlines the need to pay attention to rings between external and internal zones and to the edge of the external zone. Visual interpretation leads to the conclusion that the area of interest is inside of external gray zone, because the main change of intensities is concentrated on the boundary, and edge contours are not similar for different images. To localize the position of the contour and calculate numerical signs the following steps are performed:

- filtration by application of binarization (the threshold is defined experimentally) and the Sobel differential operator;
- finding the image center: we use "sliding line detectors" which searches a group of close white pixels inside the black contour;
- search the curve on the image. We construct the line from the image center with a given angular coefficient and take the point on the line, which is the point of the brightness difference, as approximation for the point on the curve. The process is repeated for the next angle value.

The obtained sequence of coordinate values is an approximation of the curve. The signs are the distances from the center of the image to the points on the curve. Thus, in the results of our transformation the closed curve (in polar coordinate system) turns into a curve in Cartesian coordinates, being all its geometrical properties are saved. It is easy to understand that the dimension of the obtained vector of signs depends on the step by the angle.

4. EXPERIMENTS AND DISCUSSION

For testing the proposed algorithm, we used the set of 128 soil images, obtained by the capillary dynamolysis method. These images were produced in four different laboratories with various conditions. Samples were taken from 7 distinct soil types, and NaOH sample was additionally included in the experiment. Dataset is supplemented by the information about the nature of soil samples such as id of sample environment (sampleID), dates of extraction and experiment and the laboratory identifier. The results of exploratory analysis clearly showed that initial parameters of experiments influence the inner structure of obtained samples. Therefore we performed the analysis of each group individually to reveal both generalizing and differentiating signs. We implemented three different clusterization techniques for analysis of each group of samples. Hierarchical clustering and Kohonen self organizing map (SOM) were preferred because of simple visual interpretation and lack of requirement to define initially the number of clusters. We acquired results of both methods for each laboratory and compared the fragmentation obtained with the information about the nature of soils. In this case the conclusions about the suitability of features were drawn basing on the quantity of soil samples from single environment (SampleID).

Besides that the attention was paid to the differences in results of SOM and hierarchical clustering. The distribution of objects from single sampleID turned up into one cluster (for one of four laboratories) is shown in Table 1. Two numbers written in a table through a slash are the number of images from one sampleID in one cluster and total amount of objects in target sampleID respectively.

Table 1. The results of clusterizations

	Kmeans	Hierarch	Som
12-1	3/5	4/5	3/5
12-2	3/6	4/6	3/6
67-1	3/7	4/7	2/7
67-2	4/6	4/6	3/6
91-1	3/6	3/6	1/6
91-2	3/6	4/6	6/6
91-3	3/6	6/6	4/6

Table 2. Cross-correlation between 12-1 and 67-2 SampleIDs

	12-1	12-2	67-1	67-2
12-1	0.524	0.453	0.424	0.459
12-2	0.418	0.381	0.329	0.274
67-1	0.361	0.288	0.456	0.256
67-2	0.325	0.283	0.389	0.548
91-1	0.323	0.356	0.380	0.440
91-2	0.343	0.380	0.403	0.442
91-3	0.488	0.386	0.422	0.466
NaOH	0.281	0.256	0.248	0.148

Table 3. Cross-correlation between 91-1 and NaOH SampleID

	91-1	91-2	91-3	NaOH
12-1	0.351	0.343	0.384	0.267
12-2	0.224	0.355	0.397	0.237
67-1	0.336	0.381	0.404	0.235
67-2	0.392	0.478	0.327	0.252
91-1	0.493	0.415	0.288	0.238
91-2	0.312	0.517	0.488	0.260
91-3	0.454	0.430	0.553	0.266
NaOH	0.263	0.267	0.256	0.502

Further we propose to estimate the ability of extracted features to differentiate the objects of one class from the objects of another (without regard for the conditions of the experiment). Tables 2 and 3 show values of cross-correlation coefficients between randomly select objects in each class.

It is a standard method to estimate the degree of correlation between two series. This characteristic is invariant regarding rotation (for example 2 similar chromatograms may be rotated by different ways). Values close to 1 imply high degree of similarity between objects, values close to 0 signify no dependencies. For assessment we can use Chaddock scale, that make weak connections for correlation between 0.1 and 0.3, moderate for values between 0.3 and 0.5 and noticeable between 0.5 and 0.7. It is clear that the correlation between NaOH class and all other classes is weak in terms of the Chaddock scale. This allows us to assume that obtained features help to detect samples with the worst soil quality.

Hierarchical clustering shows the best results and collects more the half of objects from same samples into one class. But evaluation of final split seems not to be accurate enough to clearly distinguish samples from one laboratory. The directions of future work will include an exploring of new additional features that could be combined with existing ones and demonstrate a higher degree of similarity between objects from one class.

5. CONCLUSION

In this work we proposed an approach to the analysis of images obtained by the capillary dynamolysis method. It is based on the estimation of the image form and geometrical properties of the boundary curve. The main goal is to find key characteristics which may be used as classification signs. As such a sign we considered the vector of distances from the image center to the points on the boundary curve. The method was tested on the set of 128 soil images. To estimate the effectiveness of these signs the clusterization was performed, and cross-correlations between different classes were calculated. This method may be considered as a promising tool for further investigations

ACKNOWLEDGEMENT

The authors wish to thank Montserrat Trio Maseda from Instituto Geológico y Minero de España for images of soil and many useful discussions.

REFERENCES

- [1] Baumgartner S., Doesburg P., Scherr C., Andersen J. Development of a Biocrystallisation. Assay for Examining Effects of Homeopathic Preparations Using Cress Seedlings, EvidenceBased Complementary and Alternative Medicine, 2012. doi:10.1155/2012/125945
- [2] Capillary dynamolysis images dataset. Available: https://www.dropbox.com/sh/iq81pe4o6_vbnbu/AAB-g6ntL8C6OACmGk_LU5Da?dl=0
- [3] Cointault F., Journaux L., Gouton P. Statistical methods for texture analysis applied to agronomical images, Image Processing: Machine Vision Applications, 2008. doi: 10.1117/12.768649
- [4] Fritz J., Athmann M., Meibner G., Kopke U. Quality characterisation via image forming methods differentiates grape juice produced from integrated, organic or biodynamic vineyards in the first year after conversion, Biological Agriculture and Horticulture, 2017. doi: 10.1080/01448765.2017.1322003
- [5] Fritz J., Athmann M., Kautz T., Kopke U. Grouping and classification of wheat from organic and conventional production systems by combining three image forming methods, Biological Agriculture and Horticulture, 2011, Vol. 27, pp. 320-336.
- [6] Garini Y., Young I., McNamara G. Spectral imaging: principles and applications, International Society for Analytical Cytology, 2006, vol. 69(8), pp. 735-747.
- [7] Kokornaczyk M., Primavera F., Luneia R., Baumgartner S., Betti L. Analysis of soils by means of Pfeiffer's circu-

lar chromatography test and comparison to chemical analysis results, Biological Agriculture and Horticulture , 2016. doi: 10.1080/01448765.2016.1214889

- [8] Lia B., Vitality and Quality as Seen Through Picture Forming Methods, Biodynamics, 2016.
- [9] Murenin I., Ampilova N. On the analysis of images obtained by capillary dynamolysis method. Proc LXXI Int. Conf. "Herzen readings-2018", p. 234 – 238.(in Russian)
- [10] Murenin I., Ampilova N. On a classification of soil images obtained by capillary dynamolysis method. Proc. XVI

St.Petersburg Int.Conf. "Region Informatics RI-2018", 24-26 Oct. 2018, p. 545-547. (in Russian)

- [11] Pfeiffer E. Chromatography Applied to Quality Testing, Biodynamic Farming and Gardening Association, 1984. ISBN:9780938250210
- [12] Unluturk M., Unluturk S., Pazir F., Abdollahi F. Capillary Dynamolysis Image Discrimination Using Neural Networks, Journal of Information Technology and Software Engineering, 2011. doi: 10.4172/2165-7866.1000101

MODELLING THE DYNAMICS OF CHARGED PARTICLES USING UNITY ENGINE

M. Syasko, I. Soloviev

St. Petersburg State University, Comp. Sci. Dept.

st024504@student.spbu.ru, i.soloviev@spbu.ru

Abstract

The problem of computer modelling and visualization of low frequency electromagnetic fields is in the area of interest of such directions as education, research activity, medicine and industry. Visualization helps better understanding the influence of magnetic fields on various physical environments, and a clarifying the physical and mathematical models that are used. In industry visualization is often applied in the tools for non-destructive testing and in magnetic inspection systems. In medicine these fields are traditionally used in magnetotherapy, and at the moment computer modelling and visualization are often the only practical approach to the studying the influence magnetic fields on a living organism. In this work we demonstrate a computer tool both for modelling a magnetic field distribution and the motion of a charged particle in this field. The algorithms are implemented in a special environment Unity. That allows the combining calculations and visualization and results in considerable reducing run-time and the development of a flexible application that may be easily used by physicians. The results of experiments are given.

1. INTRODUCTION

Computer modelling and visualization of low frequency electromagnetic fields are of interest to education, research activities, medical practice and industry. Visualization furnishes insights into the nature of the influence of magnetic fields on various physical environments, reveals peculiarities of emerging phenomena and in many cases helps to clarify the physical and mathematical models that are used. In industry such a visualization is often applied when elaborating tools for non-destructive testing [6]. Low frequency magnetic fields are also used in magnetic inspection systems.

Of special interest is the application of the methods of computer modelling and visualization in biology and medicine [1,5]. Experimental data show that low frequency electromagnetic fields may have a beneficial effect on the processes occurring in living systems. Over the past 20 years magnetobiology [4] is progressing rapidly. This branch of biology originates from biophysics and contributes to the elaboration of the methods of treatment of various deceases. In particular, in medicine the magnetotherapy method is widely used, and in this case the modelling and visualization of magnetic fields help to set and control the device parameters. That results in increasing effectiveness and safety of curative sessions.

Computer modelling and visualization of low frequency magnetic field in a magnetotherapy device

was performed in [2, 7], where the calculations were made for a given configuration of coils in 3D space. The calculation of magnetic induction was performed in the points of a given space grid, and to obtain the induction value in an arbitrary point various methods of interpolation were used. In view of the large volume of calculation several types of optimization were implemented. Basing on the obtained results the authors of [3,9] developed an application for modelling the motion of a charged particle in the low frequency magnetic field generated by a given configuration of coils. In all the papers visualization was performed with using Para-view software, which complicated the technology considerably.

Thus at the moment there is a program software for calculation and visualization of the magnetic field generated by different configurations of coils used in magnetotherapy devices, and the modelling of the motion of a charged particle in this field. The main problem is the authors used specialized graphic packages to visualize the results of calculation. Such an approach complicates the practical using of the software implemented, because a user has to organize file transfer between different program systems "by hand".

In this work we present a more flexible variant of the solving the problem above, which combines both all the calculations and visualization in one environment. Besides that, a new algorithm for calculation and visualization of low frequency magnetic

field is designed and implemented. It is based on the fact that in any point of the field the magnetic induction vector lies on the tangent to a magnetic field line. So, we do not use a predefined space configuration for the lattice of points, but being in a given point we obtain the next point for calculation by moving along the tangent on a small distance h . On this approach we do not need to use an interpolation, which leads to a reducing run-time.

In our study we have implemented an approach where the calculation of the field and trajectories of charged particles and the visualization of the results are performed in a uniform programming environment — the cross-platform software package Unity [10,11]. This environment is widely used for design of the projects with step-by-step improvement, for example in the cycles of prototyping or testing. There is a wide range of tools for the editing objects in the built-in editor and tuning the editor by using a scenario which adds new functional peculiarities and control elements.

Unity applications can be deployed to any desktop or mobile platform with little optimization and minor changes in code. This technique allowed us to optimize resource-intensive mathematical operations, which led to an optimization as a whole.

The system assumes further development. It is planned to visualize the motion of a charged particle in various physical environments, to improve the interface, the editor for the environment, coils and charged particles. The implemented program product may be easily used by physicians for study the results of magnetotherapy for various parameters of physiotherapy devices.

The paper is organized as follows. The next section contains a brief description of the mathematical model and algorithms for its solving. In section 3 the description of Unity environment is given. The last section shows the results of experiments.

2. MATHEMATICAL DESCRIPTION OF THE MODEL

2.1. Magnetic field calculation

Our model includes the calculation of the low-frequency magnetic field generated by one or several coils which are placed in the space according to a given configuration and the modelling of the motion of a charged particle in this field. The first problem is well known model task, and the calculation

is performed in the cylindrical system of coordinates by the formulas using elliptic integrals. In the process of calculation we have to use the Cartesian coordinates, so the transitions between two systems are performed. The magnetic field is traditionally calculated in the points of a given space grid, so in an arbitrary point an interpolation is performed. This way of solving was due to the fact that for visualization a special software was used, which required the array of values of magnetic inductions in a lattice given. This approach was implemented in our previous works [2,3,7,9]. In this paper we propose a new method in which we construct the grid on a section plane. Each vector of magnetic induction in a point M lies on the tangent to the magnetic field line passing through M, hence we start from a point of the grid, calculate the magnetic induction and obtain the next point as the point on the tangent on a given distance from the initial point M. The implementation of such an algorithm became possible in the special environment which unites calculations and visualization.

In the modelling of the charged particle motion we use the second law of Newton, being the Lorentz force acts on the particle. We use the second order system of difference equations which is obtained by application of the method of central differences for derivatives. Such an approach leads to more effective results and does not require using software packages. As these tasks were discussed in papers [2,3] in details, we give here only main formulas for easier understanding.

The scheme for calculation of magnetic field for one contour of a coil is shown on Fig.1.

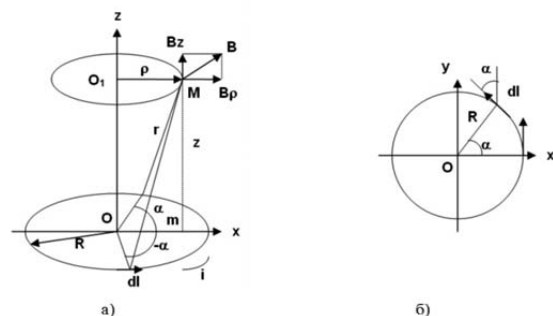


Figure 1. Calculation of magnetic induction in a point M on a contour

Here magnetic field lines are in the plane passing through the axis Oz . The magnetic induction vector \vec{B}_M in a point M is defined by scalar components $B_\rho = rot_\rho A$ and $B_z = rot_z A$, (as $B_\alpha = 0$) and are calculated as

$$B_\rho = \frac{\mu_0 i}{2\pi} \frac{z}{\rho \sqrt{(R+\rho)^2 + z^2}} \left(\frac{R^2 + \rho^2 + z^2}{(R-\rho)^2 + z^2} L - K \right), \quad (1)$$

$$B_z = \frac{\mu_0 i}{2\pi} \frac{1}{\sqrt{(R+\rho)^2 + z^2}} \left(\frac{R^2 - \rho^2 - z^2}{(R-\rho)^2 + z^2} L + K \right). \quad (2)$$

where L and K are elliptic integrals of the first and second type.

For an arbitrary configuration of coils the value of magnetic induction in a point M is calculated as the sum of magnetic induction taken over all the contours (using formulas 1,2) of all the coils, and all needed coordinate transformations are performed. All these actions are collected in a program block (procedure) *MagnIndPoint()*.

2.2. Visualization of magnetic field

The algorithm for calculation of magnetic induction is the follows.

- Chose a plane containing OZ axis and orthogonal the plane XY.
- Construct a lattice of points (M_i) in the given part of this plane and calculate the magnetic inductions vectors B_{M_i} .
- Let $M(x, y, z)$ be a point of the lattice and B_M be the magnetic induction vector in M . This point lies on a magnetic field line and B_M is on the tangent in this point to the line. The directing vector of the tangent is defined by the coordinates (B_x, B_y, B_z) . To obtain the next point for calculation of magnetic induction we take the point $M_1(x_1, y_1, z_1)$ on the tangent which is on a small distance h from $M(x, y, z)$. The coordinates of $M_1(x_1, y_1, z_1)$ are found from the system

$$\frac{x_1 - x}{B_x} = \frac{y_1 - y}{B_y} = \frac{z_1 - z}{B_z},$$

$$(x_1 - x)^2 + (y_1 - y)^2 + (z_1 - z)^2 = h^2.$$

Thus, we have

$$x_1 = x \pm \frac{hB_x}{\alpha(x, y, z)},$$

$$y_1 = y \pm \frac{hB_y}{\alpha(x, y, z)},$$

$$z_1 = z \pm \frac{hB_z}{\alpha(x, y, z)}$$

where

$$\alpha(x, y, z) = \sqrt{B_x^2 + B_y^2 + B_z^2}.$$

We take the both values for (x_1, y_1, z_1) and repeat the calculations from item a). The construction is completed when we come to the boundary of the given area or the number of steps is achieved. The number of section planes is a parameter of the program.

2.3. Motion of a charged particle

In what follows we used the mathematical model that includes the action of electrical field as well. The detailed derivation of equations for the movement of charged particle in electrical and magnetic fields is given in many textbooks, for example in [8]. We describe them briefly. Let q and m be charge and mass of a particle. Denote by $\vec{E}(x, y, z, t)$ and $\vec{B}(x, y, z, t)$ the intensities of electrical and magnetic field induction in the point (x, y, z) at the moment t . The force acting the ion in electrical field is equal to $q\vec{E}$, and the Lorentz force in magnetic field equals $q\vec{v} \times \vec{B}$. Writing the second law of Newton we obtain $m \frac{d\vec{v}}{dt} = q(\vec{E} + \vec{v} \times \vec{B})$. Assuming that \vec{B} is co-directed with Oz, and hence $B_z = B, B_x = B_y = 0$, we obtain the following system of equations

$$m\ddot{x} = q(E(x, y, z, t) \sin \gamma \cos \beta + \dot{y} B(x, y, z, t))$$

$$m\ddot{y} = q(E(x, y, z, t) \sin \gamma \sin \beta - \dot{x} B(x, y, z, t)) \quad (3)$$

$$m\ddot{z} = qE(x, y, z, t) \cos \gamma$$

The system was investigated in [3,9] and the algorithm for approximate calculation based of using difference equations was proposed and implemented. The second order discrete system obtained from (3) has the form

$$x_{i+1} - K_i y_{i+1} = 2x_i - x_{i-1} - K_i y_{i-1} + L_i \sin \gamma \cos \beta$$

$$K_i x_{i+1} + y_{i+1} = 2y_i - y_{i-1} + K_i x_{i-1} + L_i \sin \gamma \sin \beta$$

$$z_{i+1} = 2z_i - z_{i-1} + L_i \cos \gamma, \quad (4)$$

where $K_i = \frac{qh}{2m} B(x_i, y_i, z_i)$ if current is constant, and $K_i = \frac{qh}{2m} B \cos \omega t_i$ in the case of variable

current with frequency ω . By analogy $L_i = \frac{qh^2}{m} E(x_i, y_i, z_i)$, if electrical field depends on the point, and $L_i = \frac{qh^2}{m} E \cos \omega t_i$ for periodic field. The system (4) is linear, z_i are calculated independently from x and y , and on every step x_{i+1}, y_{i+1} may be found by the Cramer method, because the determinant of the system $\Delta = 1 + K_i^2 \neq 0$.

So, in our work we realized this algorithm in Unity engine. The initial data are parameters of a particle q and m , the initial points $\mathbf{M}_0 = (x_0, y_0, z_0)$, $\mathbf{M}_1 = (x_1, y_1, z_1)$ (in global Cartesian coordinate system) of the trajectory and values of magnetic induction in these points. For each point of the trajectory the magnetic induction is calculated by the program *MagnIndPoint*.

3. TECHNOLOGICAL TOOLS OF THE MODELLING

3.1. Short description

Unity environment is a cross-platform tool for development of 3D applications. Such applications may be set practically on all known platforms [11]. Unity supports DirectX and OpenGL, which results in obtaining high-level solutions by the use of modern graphical tools.

Unity also supports script languages, so the programming in this system should present no problems because there is no need to use a large number of extraneous solutions. In the kernel of Unity there are many built-in additional tools for design, so the programming in the environment is simple and clear enough.

The working process is effected by way of the Unity visual editor. The editor links scenes, and combines the project resources and the code into interactive objects, which allows optimizing the process of implementation of professional visual applications. It should be noted that in this environment a flexible approach to object-oriented programming is realized: objects are created by union but inheritance, and there are the links controlled between the objects.

3.2. Optimization

To optimize the calculation of magnetic induction we at first splat into streams the calculation of coordinates and magnetic induction. Then we splat the

calculation of functions, magnetic induction for all the contours of a coil, total value of magnetic induction in a point, coordinate transformations and visualization. Depending on a system configuration such an optimization leads to the reducing run-time approximately 7-8 times. For a system of 3 coils (10 contours) the run time before optimization is 3-4 min, after optimization 25-30 sec.

4. EXPERIMENTS

Device parameters are the following: current intensity is 3A, coils have 7 turns, the number of windings is 25. The size of the region (in mm) is 600x600x300 the step on time h (in sec) is 10^{-6} .

The experiments were performed for various types of ions and combination of magnetic and electrical fields. In experiments was modelled the motion of 3 particles

$$Na^+: q = 3.817 * 10^{-26}, m = 1.60217 * 10^{-19};$$

$$SO_4^-: q = -7.634 * 10^{-26}, m = 1.59468 * 10^{-22}$$

$$e: q = -1.602 * 10^{-19}, m = 9.1 * 10^{-31}$$

for different configuration of magnetic field. All the particles start the motion from the initial point (5,10,15). On Fig. 2-3 the motion of the particles is shown for different position of coils.

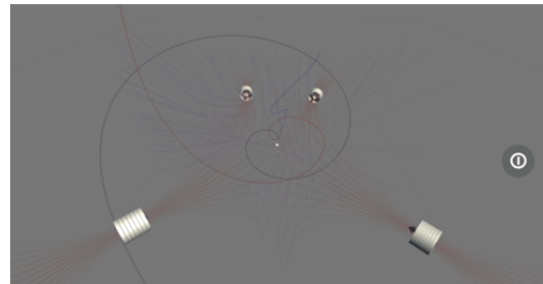


Figure 2. Four coils with coordinates (-272, 0, -272), (141, 0, 332), (-130, 0, 348), (284, 0, -284)

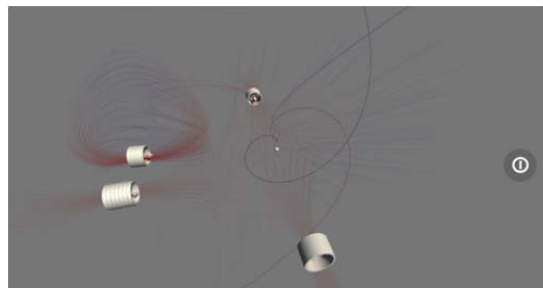


Figure 3. Four coils with coordinates (-331, 0, -74), (0, 0, 317), (-322, 0, 51), (284, 0, -280)

CONCLUSION

Development of tools for computer modelling of magnetic field distribution and the motion of various particles in the field is the important task which may help in studying the influence of low frequency magnetic field on living tissues and estimate the effectiveness of various curative sessions. Further investigations lead to a natural using other mathematical models which may be applicable not only for air but for different environments as well.

REFERENCES

- [1] V. Aleksandrov. Electromagnetic fields and ecology. St. Petersburg, 2005. (in Russian).
- [2] N. Ampilova, D. Dimitrov, B. Kudrin. Mathematical modelling of low frequency magnetic field in systems for magnetotherapy. Proc. 8 Int. Conf. CEMA13, Sofia, Bulgaria, October 17-19, 2013, p. 48-51.
- [3] N. Ampilova, F. Uvarichev, I. Soloviev. On the estimation of magnetotherapy curative sessions effects. Proc. 13 Int. Conf. CEMA18, 18-20 Oct. 2018, Sofia, Bulgaria, p. 62-65, ISSN: 1314-2100, Изд. KING 2001, Sofia.
- [4] V. Binhi. Magnetobiology: Underlying physical problems. San Diego, Academic Press, 2002.
- [5] V. Binhi, A. Savin. Effects of weak magnetic fields on biological systems: physical aspects. PHYS-USP, 2003, 46 (3), p. 259–291.
- [6] N. Ida. Numerical modelling for electro-magnetic non-destructive evaluation. New-York, Springer Publishing Company, 1994.
- [7] B. Kudrin, I. Soloviev. On interpolation methods of low frequency magnetic field in systems for magnetotherapy. Proc. 9 Int. Conf. CEMA14, Sofia, Bulgaria, October 16-18, 2014, p. 154-157.
- [8] B. Lennert, "Dynamics of charged particles", North Holland, 2004.
- [9] F. Uvarichev, N. Ampilova, I. Soloviev. On the modelling ion motion in electromagnetic field. Proc. 10 Int. Conf. EPE-2018, ID 2627, p.1-4, ISBN 978-1-5386-5061-5 IEEE Catalog number CFP 1847S-USB.
- [10] Unity. URL: <https://unity.com>
- [11] Unity Multiplatform. URL: <https://unity3d.com/unity/features/multiplatform>.

IMPROVED ALGORITHM FOR CALCULATING GEOMETRIC CHARACTERISTICS FROM OPTICAL IMAGES OF CORRODED OBJECT'S CROSS-SECTION

Borislav Bonev

Department of Microelectronics, Technical University of Sofia
8 Kliment Ohridski Blvd., Sofia, Bulgaria
T. +359876432090; E-mail: bonev@ecad.tu-sofia.bg

Anna Stoynova

Department of Microelectronics, Technical University of Sofia
8 Kliment Ohridski Blvd., Sofia, Bulgaria
T. +359882142522; E. ava@ecad.tu-sofia.bg

Antonio Shopov

Department "Mechanics and Mathematics", VSU "Luben Karavelov"
175 Suhodolska str., Sofia, Bulgaria
T. +359878930570; E. shopoff@mail.bg

Abstract

The paper proposes improvements of previously proposed by authors method for automated calculation of second area moments of random complex cross-sections by using digital images. The method is optimized for determination of corrosion impact on geometric characteristics of random cross-sections. The comparison between the method and other methods is presented for verification of the obtained results. It is studied the impact of the image's resolution on method accuracy.

1. INTRODUCTION

In modern engineering practice, various metrics can be determined by the use of digital images. Ways to determine the moment of inertia of a section have been developed [3, 7]. Although the formulas for the corresponding calculations are known, their precise calculation is still fraught with the corresponding calculation errors due to many factors. Engineering staff uses graphical computing software (such as AutoCAD for example) where it is possible to calculate geometric characteristics by using cross-section photo material. In these methods it is required to draw a given area or figure, to draw in the so-called "region" and from there the program can perform the calculation. This method significantly increases the possibility of errors and inaccuracies.

Usage of optical digital images in analysis and classification of materials is well studied [1-7]. Publication [7] proposes a method for determining second area moments using a digital image. This approach is sufficiently reliable and accurate in cases where the section has an axis of symmetry. In corrosion sections, the methods needs to be improved, since corrosion propagates arbitrarily, not symmetrically, and using the theory, there should be the product moment of inertia different from zero [8-9]. For this

reason, the possibility to calculate the principal axes of moment of inertia and rotate them to determine the maximum and minimum moment of inertia has been added. In [7], the image is segmented into two regions – region with area and region without area. This article proposes to segment three regions – solid material, empty areas and corrosion areas.

2. BASIC THEORETICAL METHOD

In [7], the proposed method uses the representation of image constituent pixels as a geometric figure with corresponding geometric characteristics (fig. 1), on the basis of which the moment of inertia is calculated:

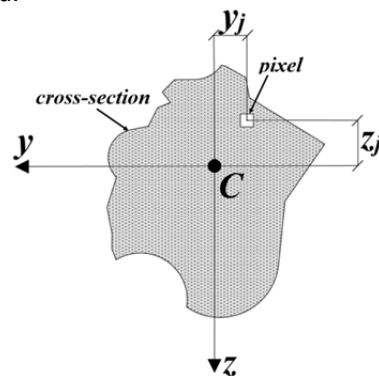


Figure 1. Basic concept for determination of pixel second area moment [9]

For figures without an axis of symmetry, the product moment of inertia is calculated by the formula [8-9]:

$$I_{yz} = \iint_A y \cdot z \, dA \quad (1)$$

It should be noted that the product moment of inertia could be: positive, negative or zero (in the case of an axis of symmetry). Fig. 2 shows the basic concept for determining axial moments of inertia and principal moments of inertia.

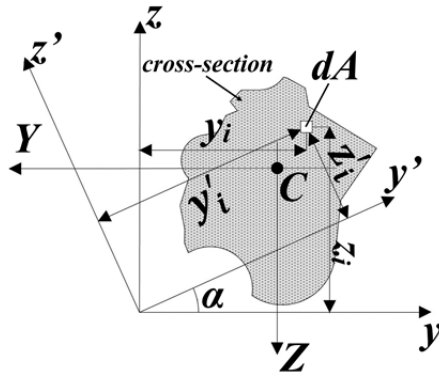


Figure 2. Basic concept of moments of inertia about inclined axis [9]

With known formulas for rotating the coordinate axis [9]:

$$I_{y'} = \frac{1}{2} \cdot (I_y + I_z) + \frac{1}{2} \cdot (I_y - I_z) \cdot \cos 2\alpha - I_{yz} \cdot \sin 2\alpha, \quad (2)$$

$$I_{z'} = \frac{1}{2} \cdot (I_y + I_z) + \frac{1}{2} \cdot (I_y - I_z) \cdot \cos 2\alpha + I_{yz} \cdot \sin 2\alpha, \quad (3)$$

$$I_{y'z'} = \frac{1}{2} \cdot (I_y - I_z) \cdot \sin 2\alpha + I_{yz} \cdot \cos 2\alpha \quad (4)$$

the extreme values of the axial moment of inertia can be determined using this requirement [9]:

$$\frac{dI_{y'}}{d\alpha} = 0 \quad (5)$$

By making the appropriate transformations, the following formula is obtained [9]:

$$\tan 2\alpha = \frac{2 \cdot I_{yz}}{I_z - I_y} \quad (6)$$

This equation has infinite number of solutions. Assuming α_1 is one of them, all others can be expressed by the formula [9]:

$$\alpha_{k+1} = \alpha_1 + k \cdot \frac{\pi}{2}, \quad (7)$$

where $k = 1, 2, 3, 4, 5, 6, \dots, n$.

If the latter formula is used, it represents two different principal axes that are mutually perpendicular. We denote these axes as y' and z' , as well as other authors [9]. Then they become principal axes of moment of inertia and for them is valid the following equation for every α [9]:

$$I_{y',z'} = \frac{(I_y + I_z)}{2} \pm \sqrt{\left(\frac{I_y - I_z}{2}\right)^2 + I_{yz}^2} \quad (8)$$

From the moment of inertia obtained, one is maximum and the other is minimum. The maximum is denoted I_1 and the minimum is I_2 and they can be determined by the formula [9-10]:

$$I_{1,2} = \frac{(I_y + I_z)}{2} \pm \sqrt{\left(\frac{I_y - I_z}{2}\right)^2 + I_{yz}^2} \quad (9)$$

This classical equation can be used for verification [9-10]:

$$I_1 \cdot I_2 = I_y \cdot I_z - I_{yz}^2 \quad (10)$$

Obtaining a zero for the product moment of inertia for a pair of axes means that these axes are principal axes of moment of inertia and if a figure with arbitrary corrosion products position has an axis of symmetry, then this axis is one of the principal axes of moment of inertia.

3. SOFTWARE IMPLEMENTATION OF THE METHOD

The presented method requires an enormous number of calculations with high performance. MatLab was chosen as the environment for the implementation of the proposed method. The software implementation is based on the algorithm presented in our previous study [7] with several major improvements:

- image segmentation into three areas – solid area, corrosion area and empty area (voids, holes, etc);
- determining the principal axes and moments of inertia;
- automatic visualization of principal axes of moment of inertia axes and coordinate systems;
- greater degree of automation of the calculation process.

Image segmentation is necessary in order to be able to examine sections where both areas with

corrosive products and areas without solid material are present (e.g. holes). Image segmentation is realized by well-known method of image binarization [7].

The calculation process is highly automated. The user is required only to define the section outside contour, as well as to measure and enter only one physical dimension of the section.

The calculation of the center of gravity is carried out by the following equations [7]:

$$Z_C = \frac{\sum_{i=1}^{N_{solid}} A_{pixel} z_i}{N_{solid} A_{pixel}}, \quad (11)$$

$$Y_C = \frac{\sum_{i=1}^{N_{solid}} A_{pixel} y_i}{N_{solid} A_{pixel}}, \quad (12)$$

$$z_i = (l_c - l_i + 0.5) a_{pixel}, \quad (13)$$

$$y_i = (c_i - c_c + 0.5) a_{pixel}, \quad (14)$$

where l_c, c_c – coordinates of the origin of the cross-section coordinate system; l_i, c_i – coordinates of an arbitrary pixel from the cross-section area, N_s – number of the pixels, representing areas with solid material.

The moments of inertia I_1 and I_2 are calculated as follows [9]:

$$I_{z_{solid}} = \sum_{i=1}^{N_{solid}} \left(\frac{a_{pixel}^4}{12} + A_{pixel} y_i^2 \right) \quad (15)$$

$$I_{y_{solid}} = \sum_{i=1}^{N_{solid}} \left(\frac{a_{pixel}^4}{12} + A_{pixel} z_i^2 \right) \quad (16)$$

$$I_{yz_{solid}} = \sum_{i=1}^{N_{solid}} A_{pixel} y_i z_i \quad (17)$$

$$z_i = (l_i - l_c + 0.5) a_{pixel} + Z_{C_m} \quad (18)$$

$$y_i = (c_i - c_c + 0.5) a_{pixel} + Y_{C_m} \quad (19)$$

The determination of the principal moments of inertia and the angles of rotation of the coordinate system are determined after completion of the calculations described above, on the basis of the formulas presented in section 2.

4. METHOD VERIFICATION

To verify the proposed method, the geometrical characteristics of a section were calculated. The drawing of the section is shown in fig. 3. Based on the drawing, a high-resolution bitmap image (the

section region of image is formed by 10,000,000 pixels) was made. The proposed method was applied to this image.

A manual calculation of the geometric characteristics of this section is presented in [10]. Table 1 presents the values obtained by manual calculation and compared with those obtained by the proposed method. The error of the values calculated by the proposed method is calculated.

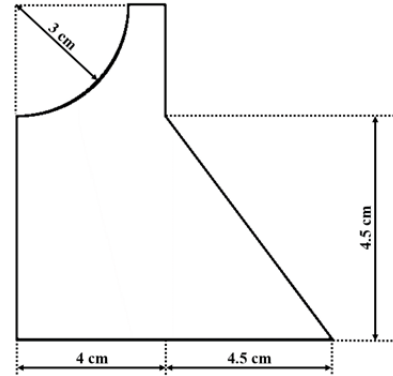


Figure 3. Diagram of the cross-section used for verification [10]

It can be seen that the accuracy of the proposed method is very high if the resolution with which the section is presented is high.

Table 1. Results from verification of the proposed method

	calculation given [10]	proposed method	error [%]
Z_c [cm]	3.167	3.167	0%
Y_c [cm]	3.235	3.235	0%
I_z [cm ⁴]	155.7	155.7	0%
I_y [cm ⁴]	200.9	200.9	0%
I_{yz} [cm ⁴]	-43.17	-43.18	0.0232%
I_1 [cm ⁴]	227.03	227.05	0.0088%
I_2 [cm ⁴]	129.57	129.58	0.0077%
α_1 [deg]	31.183	31.189	0.0192%
α_2 [deg]	-58.814	-58.811	0.0051%

Fig. 4 shows the generated image with plotted coordinate systems. The legend is as follows:

cyan – y-coordinate of the section's coordinate system;

magenta – z-coordinate of the section's coordinate system;

blue – y-coordinate of the translated coordinate system;

red – z-coordinate of the translated coordinate system

green – first principal axis of moment of inertia defining the direction of maximum moment of inertia I_1

yellow – second principal axis of moment of inertia defining the direction of minimum inertia moment I_2

α – angle of rotation relative to the coordinate system between horizontal axis and maximum moment of inertia I_1

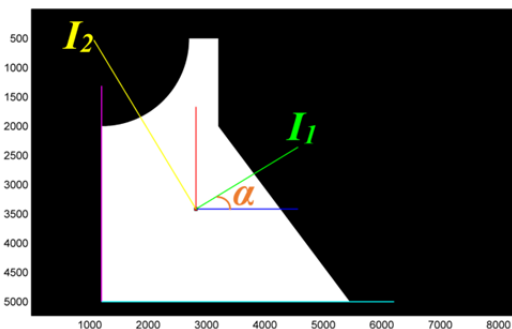


Figure 4. Coordinate systems of the cross-section, used for verification

5. STUDY THE IMPACT OF IMAGE RESOLUTION ON CALCULATION ACCURACY

The study in section 4 was carried out with high resolution image. A study was performed with reduced image resolution in order to determine the effect of the image resolution on the accuracy of the calculation. Fig. 5 shows the dependence of calculation error from number of section's pixels.

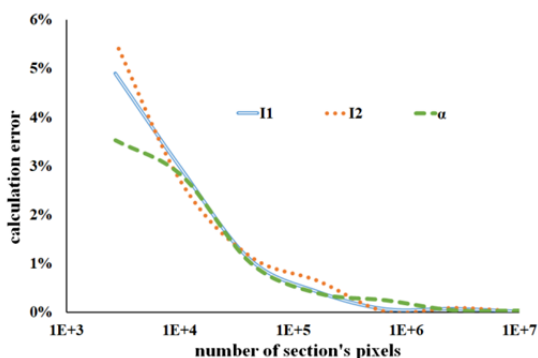


Figure 5. Dependence of calculation error from number of section's pixels

It can be seen that the calculation error is below 1 % for number of section's pixels larger than 100 000. Respectively section image with resolution larger than 0.3 megapixel (the section should occupy as much of the image as possible.) will be enough for calculation with error below 1 %.

6. USING THE METHOD FOR SECTION WITH CORROSION

After the method has been verified, it has been applied in calculating the geometrical characteristics of a section with corrosion. The shape of the corrosion products on the surface is random and therefore manual calculation is practically impossible. Image used for the calculation is shown in Fig. 6. The image resolution is 5936×4144 (24 megapixels). The section area contains 9.5 megapixels.



Figure 6. Photograph of the cross-section with corrosion used for calculation with proposed method

A comparison of the obtained results was made using the AutoCAD software. A method with AutoCAD is widely used in practice for calculation of geometric characteristics. Classically, this method requires the manual enclosure of areas for which the geometric characteristics are calculated. For case of image of section with corrosion such as used in this case, this manual enclosure is an extremely slow and difficult process. The image with hand-drawn lines in the environment of AutoCAD software is shown in Figure 7. Table 2 presents the results obtained by calculation using AutoCAD and proposed in this paper method.

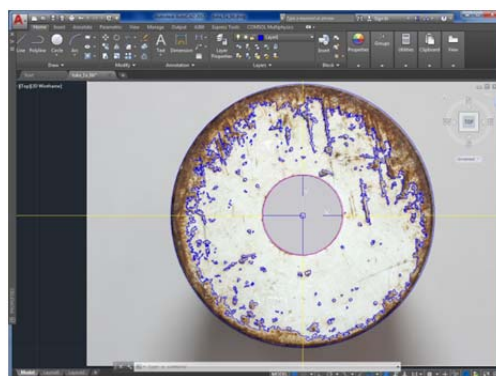


Figure 7. Using AutoCAD for geometric characteristics calculation

Table 2. Results from geometric characteristics calculation of the cross-section with corrosion

	AutoCAD calculation	proposed method	difference [%]
Z_c [cm]	3.80	4.62	13.80
Y_c [cm]	4.13	5.042	18
I_z [cm ⁴]	316.55	263.29	20.23
I_y [cm ⁴]	343.19	270.74	21.11
I_{yz} [cm ⁴]	-23.09	-16.38	29.06
I_1 [cm ⁴]	356.63	283.813	20.41
I_2 [cm ⁴]	303.22	250.216	17.48
α_1 [deg]	29.95	38.595	22.40
α_2 [deg]	-60.00	-51.406	19.45

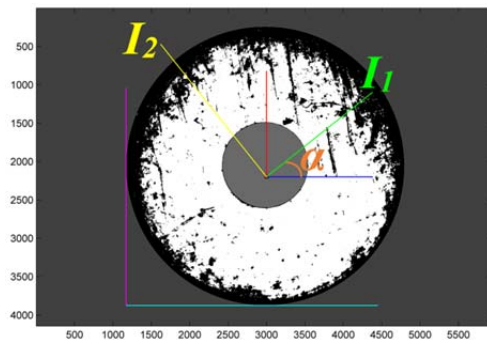


Figure 8. Coordinate systems of the cross-section with corrosion (diameter is 10 cm, image binarization with trace hold 0.65) is used for verification

7. CONCLUSION

The developed algorithm and calculation method are characterized by great versatility, reliability and accuracy.

The algorithm proposed in this article makes it possible to calculate the geometric characteristics of cross sections with the presence of corrosion products on the surface, where the classical methods are inapplicable or would be very difficult to implement them. For comparison, the method proposed in this article requires no more than a few minutes to apply, whereas the hand-drawing method with AutoCAD used for comparison takes days for complex sections.

The difference between the results obtained by AutoCAD and the method in this article are due to major imperfections in the algorithms used. AutoCAD uses vector graphics rather than raster graphics, so the following prerequisites exist:

- The section to be analyzed must be the only section in the drawing;
- The section must be hatchable;
- Can only process lines, arcs, polyline, splines, circles or ellipses are supported if created with pellipse;
- Breaks down the section into component areas or slices. More slices means greater accuracy. The maximum is limited;
- Set desired accuracy, decimal places, conversion units, and units of measure;
- When we have an optical image manual enclosing method and the imperfections of the human eye.

With this method, the segmentation and the entire computation process is automatic. This in addition to the verification results, justifies that the method to be considered more reliable.

The developed method can be applied outside the field of study of the corrosive influences and it is precise enough to be used in other areas, where it is used digital images, e.g. medical imaging.

8. APPENDIX AND ACKNOWLEDGMENTS

This research was funded by a grant (No. 192ΠΔ0016-03) from the Scientific and Research Sector of the Technical University of Sofia.

The authors would like to thank for the support and assistance of Prof. Dr. Eng. Yavor Mihov, University of Architecture, Civil Engineering and Geodesy, Faculty of Hydraulic Engineering, Department „Technical Mechanics “.

REFERENCES

- [1] A. Shopov and B. Bonev, "Determination of corrosion on surface elements by a using a graphical digital image," Proceedings of XVIII Anniversary International Scientific Conference by Construction and Architecture "VSU'2018", vol. 1, pp. 685-690, 2018, in Bulgarian.
- [2] V. Sharma and T. Thind, "Techniques for detection of rust of metals using image processing: A survey," IJESE, vol.1-4, pp. 60-62, 2013.
- [3] W. Munsell, "Method to approximate section properties of mechanical elements through data obtained from digital images" U.S. Patent No. US20040062433A1, 2004.
- [4] T. Alkanhal, "Image processing techniques applied for pitting corrosion analysis," IJRET, vol.3-1, pp. 385-391, 2014.

- [5] V. Bondada, D. Pratihari and C. Kumar, "Detection and quantitative assessment of corrosion on pipelines through image analysis", *Procedia Computer Science*, vol. 133, pp. 804-811, 2018.
- [6] F. Iacoviello, D. Iacoviello, V. Di Cocco, A. De Santis and L. D'Agostino, "Classification of ductile cast iron specimens based on image analysis and support vector machine," *Procedia Structural Integrity*, pp. 283-290, vol. 3, 2017.
- [7] B. Bonev and A. Shopov, "Computation of second area moments of cross-section using an optical images".
Proceedings of X National Conference with International Participation "Electronica 2019",
DOI: 10.1109/ELECTRONICA.2019.8825629.
- [8] S.P. Timoshenko, *Strength of materials (part 1 and part 2)*, 3rd ed., Krieger Pub Co., Mala-bar, FL, USA, 1983, ISBN: 978-0898746211.
- [9] S. Kislyakov, *Strength of materials*, Sofia: Technika, 1976, in Bulgarian.
- [10] K. Gatsov and H. Kunchev, *A collection of coursework assignments by Strength of materials*, Sofia: UACEG, 1998, in Bulgarian.

WILD ANIMALS POPULATION ESTIMATION FROM THERMOGRAPHIC VIDEOS USING TENSOR DECOMPOSITION

Ivo R. Draganov, Rumen P. Mironov, Nikolay N. Neshov, Agata H. Manolova

Radiocommunications and Videotechnologies Dept.
Faculty of Telecommunications, Technical University of Sofia
8 Kliment Ohridski Blvd., 1756 Sofia, Bulgaria

e-mail: {idraganov, rmironov, nneshov, amanolova}@tu-sofia.bg

Abstract

In this paper an algorithm is presented for wild animals population estimation through background modelling and subtraction in videos captured by thermographic cameras. In order to obtain low-rank and sparse representation of the video content on a frame-by-frame basis several decomposition techniques are tested, namely the Robust Principal Component Analysis (RPCA) with its Go implementation (GoDec), Low-rank matrix completion by Riemannian optimization (LRGeomCG), Robust Orthonormal Subspace Learning (ROSL), and Non-negative Matrix Factorization via Nesterov's Optimal Gradient Method (NeNMF). Promising results are obtained in terms of accuracy and the approach seems applicable in agronomy, protection of the natural environment, forestry and others.

1. INTRODUCTION

Thermography has been long employed into numerous applications related to remote sensing, mechanical design at the stage of component durability testing, medical treatment, civil and military surveillance and others.

In [1] Yang and He investigate wide range of thermographic methods based on optical and non-optical excitation to locate damages in composites as a non-destructive approach. They group the various implementations based on the nature of the heat inductor as optical, laser, eddy current, microwave, vibro- and ultrasound. Classification of known realizations has also been provided according to the type of the heating function, style, position and motion. At the stage of registered signals processing some of the designers rely on tensor decomposition. Gao et al.[2] turn towards the estimation of fatigue and residual stress by incorporating spatial-transient-stage tensor along with Tucker decomposition taking into account the variation of material qualities over time. Positive results are reported from analyzing gear fatigue. Further the authors [3] confirm the significant level of correlation between the deviation of the physical properties of tested steel materials and the mathematical models based on tensor analysis when eddy currents are applied in a pulsed manner.

Active thermography is another mean for composites exploration by analyzing captured images for detecting various defects [4]. Series of infrared

pictures are ordered in time of recording and then adjacent pixels from consecutive planes are processed. The first derivative over the selected spatial direction together with two-dimensional wavelet transform yielded most accurate results into detecting cracks.

Series of thermo-images are also under consideration by Garbe et al. [5] who propose to have from them a complex motion estimation. Heat dissipation on a time scale as a diverging process undergoes analysis with the local gradient technique. Atmospheric interaction with the ocean surface is the primary focus with a possible application to non-destructive testing and botany as well. This method permit accuracies as high as one tenth of a pixel.

Thermography allows not only pattern analysis but also separation from thermos-series [6]. Non-negative pattern discriminative scheme when eddy current acts as a driver in pulsed thermography for detecting particular patterns and their temporal change is applicable in this unsupervised approach. It is known with its scale invariance.

Aerospace composites are another object of testing under the use of eddy current [7]. In this approach signal reconstruction along with a pattern recognition techniques take place. Relatively large surface areas under processing and short time intervals are distinct properties of this method. Tucker decomposition helps into near-surface defects spotting from a few hundred frames captured forming the three-dimensional tensor.

Tensor regression based on engaged penalties are in the basis of an image-based prognostics approach [8]. Series of degradation images supports the prediction of the residual product lifetime. Tensors give the opportunity for dimension reduction by projection to a sub-space with information sparing capability. Further, regression acts a mapping tool for the time-to-failure data and CANDECOMP/PARAFAC (CP) along with Tucker decomposition serve as parameter estimator for the higher dimension configuration. Testing with a data from rotating machinery provides positive practical results.

Another highly productive and current approach for nondestructive testing is the microwave thermography [9]. Zhang et al. present a review on various techniques employing it pointing out its advantages – selection of the area of heating, energy efficiency, power uniformity, volume affecting and ability for particular penetration. Despite being extremely useful in quality control and industrial continuous monitoring its applicability in surveillance applications is not mentioned.

Gear inspection in wind turbines at limited time intervals during general maintenance for fatigue discovery prove useful according to Gao et al. [10]. The implementation of the tensor apparatus over thermal data obtained by inductive principle it becomes possible to supply early warning on wearing out such components.

Despite the vast amount of practical implementations of thermographic sequences, most often applying tensor decomposition schemes, in non-destructive testing, quality control, fault diagnosis or investigating complex interaction processes of physical nature it seems that thermography based surveillance systems is another major field that deserves attention into employing these methods. In this study we are investigating the applicability of 4 multidimensional decomposition algorithms for wild animals population estimation through background modelling and subtraction. The tested algorithms are presented in Section 2, followed by experimental results in Section 3. The latter are discussed in Section 4 with useful guidelines about the future use of this algorithms and then the paper ends with a conclusion.

2. ALGORITHMS DESCRIPTION

2.1. GODEC

When establishing certain relations among parameters describing processes it is practical to use compressed representations and most of the processing is done by matrix completions. The latter are done by low-rank formations \mathcal{L} and sparse entities \mathcal{S} . The Go decomposition [11] is efficient tool in estimating these parts given the input matrix as:

$$\mathcal{X} = \mathcal{L} + \mathcal{S} + \mathcal{G}, \quad (1)$$

where \mathcal{G} is the present noise within the data. Alternative association is made according to:

$$\begin{cases} \mathcal{L} \cong \mathcal{X} - \mathcal{S} \\ \mathcal{S} \cong \mathcal{X} - \mathcal{L} \end{cases} \quad (2)$$

Speeding up the whole process comes from bilateral random projections [11]. It is also applicable to matrix completion. Given the objective function:

$$f = \|\mathcal{X} - \mathcal{L} - \mathcal{S}\|_F^2 \quad (3)$$

Zhou and Tao [11] prove that it goes to a local minimum while \mathcal{L} and \mathcal{S} strive to their optimums. The procedure is robust as the authors report compared to Robust PCA and OptSpace.

2.2. LRGEOMCG

LRGeomCG [12] represent low-rank matrix completion where the optimizing procedure is implemented directly given a multitude of matrices with a fixed rank. This task may be expressed as:

$$\begin{cases} \text{minimize}_x f(\mathcal{X}) := \frac{1}{2} \|P_\Omega(\mathcal{X} - \mathcal{A})\|_F^2, \\ \text{subject to } \mathcal{X} \in \mathcal{M}_k := \\ \{\mathcal{X} \in \mathbb{R}^{m \times n} : \text{rank}(\mathcal{X}) = k\}. \end{cases} \quad (4)$$

In (4), applying the Frobenius norm F , \mathcal{A} is $m \times n$ matrix on subset Ω , part of entire set of inputs $\{1 \div m\} \times \{1 \div n\}$. The holistic minimizer has a rank of k . \mathcal{M}_k is a smooth manifold over \mathbb{C}^∞ and the optimization function is denoted as f . The author reports good scalability in solving large-scale tasks with higher efficiency than some of the other well known algorithms of the same type.

2.3. ROSL

Computational sparing low-rank recovery is possible by applying ROSL [13] in the case of lacking

samples from the input data. The approach is quite practical within the computer vision field. A new measure considering the rank of the sparse representation over orthonormal subspace and a coding algorithm for rank minimization makes it possible to have quadratic complexity of the matrix size for the procedure. Shu et al. [13] prove that the new rank measure is limited from below by the nuclear norm. Random sampling leads to linear complexity in further optimizing the algorithms according to the authors and outperforms some of the earlier decompositions.

2.4. NENMF

Non-negative matrices could undergo decomposition using a product of a couple of factors in two-dimensional form with the condition to be also non-negative. NeNMF [14] uses Nestorov's optimal gradient approach over one factor optimizing it alternatively with another of fixed form. Matrix factor is recalculated at each step by the projected gradient method over a predetermined position for a search and a Lipschitz constant determines the amount of increment. Approximation accuracy and computational time efficiency are proved to be higher than that of multiplicative update rule and projected gradient method alone [14].

2.5. Motion-based multiple object tracking (MT)

As a mean for comparison with the above four described algorithms MT [15] has been tested to evaluate both the computational efficiency and the accuracy provided. Working entirely in spatial domain it is widely used in the practice consisting of the following stages: entity objects construction, tracks initialization, detecting objects, predicting track changes, assigning tracks to objects, continuous update of generated tracks and outputting the results.

3. EXPERIMENTAL RESULTS

The experiments are implemented on a PC with Intel Core i5 x64 CPU (4 cores) operating at 3.1 GHz, 12 GB operational memory. The OS is Linux Ubuntu 14.04 LTS and the testing environment – Matlab R2016a. All decomposition algorithms come from LRSLibrary v. 1.0.10 [16]. Testing database comprises of six thermographic videos (Tabl. 1) containing in various frames from one to tens of wild species.

The average decomposition (DT) and full processing time (FT) for all 6 videos, including input-output operations to the hard drive, are given in Table 2.

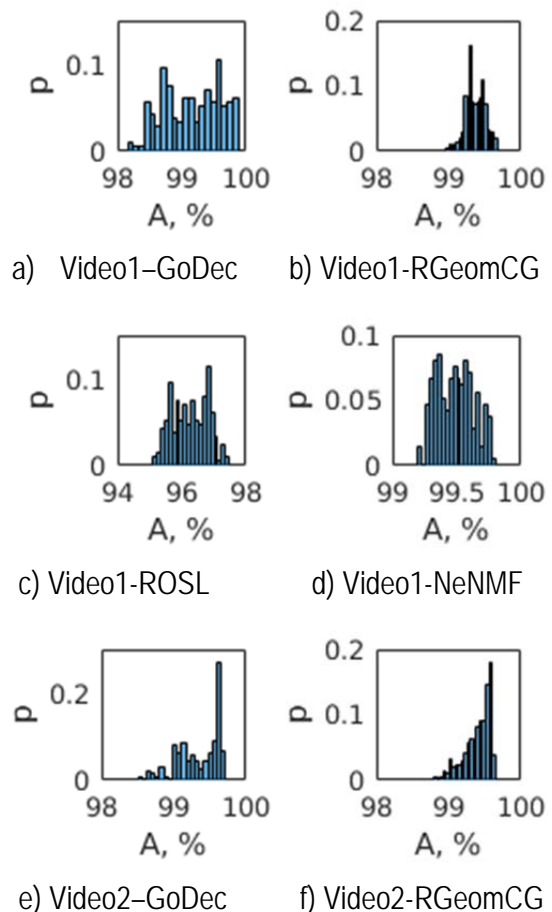
Table 1. Testing videos

Video	Width, px	Height, px	FPS	Frames
1	320	180	29.97	211
2	400	224	29.97	211
3	400	224	23.98	145
4	400	300	29.97	211
5	400	300	20.00	141
6	400	300	20.00	140

There also appears the average animal detection accuracy (A). In Fig. 1 its distribution (p) for every video reveal how stable each of the tested algorithms are.

Table 2. Average processing times and detection accuracy

Algorithm	DT, sec	FT, sec	Accuracy, %
GoDec	1.96	5.54	98.53
LRGeomCG	4.74	8.43	99.20
ROSL	9.01	12.45	96.51
NeNMF	0.36	4.01	99.30
MT	4.22	-	63.55



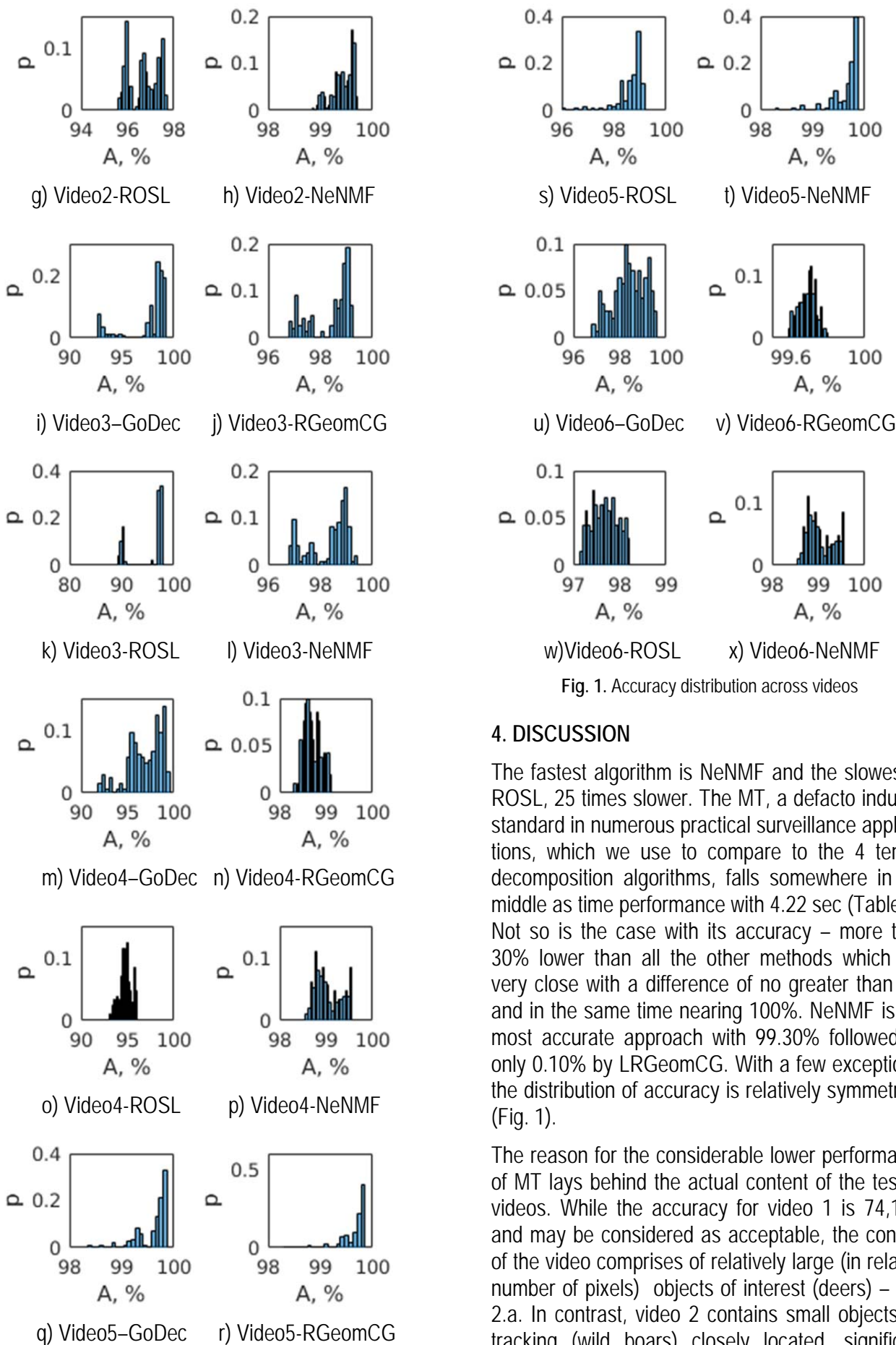


Fig. 1. Accuracy distribution across videos

4. DISCUSSION

The fastest algorithm is NeNMF and the slowest is ROSL, 25 times slower. The MT, a defacto industry standard in numerous practical surveillance applications, falls somewhere in the middle as time performance with 4.22 sec (Table 2). Not so is the case with its accuracy – more than 30% lower than all the other methods which are very close with a difference of no greater than 3% and in the same time nearing 100%. NeNMF is the most accurate approach with 99.30% followed by only 0.10% by LRGeomCG. With a few exceptions, the distribution of accuracy is relatively symmetrical (Fig. 1).

The reason for the considerable lower performance of MT lays behind the actual content of the testing videos. While the accuracy for video 1 is 74,16% and may be considered as acceptable, the content of the video comprises of relatively large (in relative number of pixels) objects of interest (deers) – Fig. 2.a. In contrast, video 2 contains small objects for tracking (wild boars) closely located, significant portions of which are being missed or tracked as one object (Fig. 2b). Only 2 objects for tracking

exist in video 3 (baby deers) and here MT achieves 100% accuracy but with 109% false positives due to slightly moving nearby objects with temperatures close to that of the animals (Fig. 2c). Accuracy falls considerably for the MT in video 4 with only 42,25% due to the extremely small objects to track (wild boars) and their large number (Fig. 2d). The perspective of capturing the video is panoramic taken high above the ground which leads to radial-like change of speed of the species even when they are moving at a constant rates. All these factors lead to that unsatisfactory result in this case. The accuracy is even smaller, just 16.31%, for video 5 which includes a family of wild boars – mother with babies which are significantly smaller in size and no detection occurs for them. Only the mature specimen has been spotted for around 1/3rd of the frames (Fig. 2e). A single deer captured at a close distance in video 6 (Fig. 2f) yields 100% accurate detections of its body by the MT. Lots of segmented detections at the boundaries of limbs and head lead to 96.43% false positives. It raises concerns for cases where multiple parts of a single connected body are moving at different speeds and sometimes in different directions. A problem that need to be resolved further by more advance analysis within the tracking algorithm.

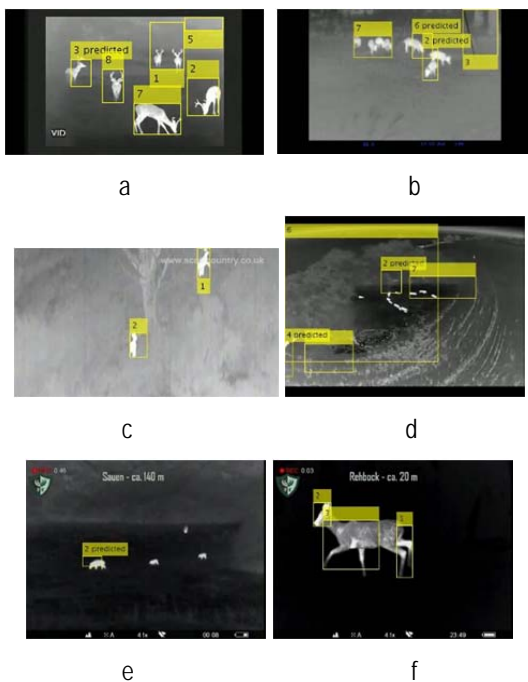


Fig. 2. Animal detections by MT

5. CONCLUSION

In this study the performance of GoDec, LRGeomCG, ROSL, NeNMF and MT algorithms is evalu-

ated applied to the wild animals detection and tracking. High accuracy for the tensor decomposition based implementations of 98.39% on average is achieved. Execution times allow real-time processing when ported on the appropriate hardware and may be used in mobile environment. Further study is needed to enhance performance when dealing with smaller objects and in particular cases of camera perspectives, e.g. when filming from a drone.

ACKNOWLEDGEMENT

This work was supported by the National Science Fund at the Ministry of Education and Science, Republic of Bulgaria, within the project KP-06-H27/16 „Development of efficient methods and algorithms for tensor-based processing and analysis of multidimensional images with application in interdisciplinary areas“.

REFERENCES

- [1] Yang, R., & He, Y. (2016). Optically and non-optically excited thermography for composites: A review. *Infrared Physics & Technology*, 75, 26-50.
- [2] Gao, B., Yin, A., Tian, G., & Woo, W. L. (2014). Thermography spatial-transient-stage mathematical tensor construction and material property variation track. *International Journal of Thermal Sciences*, 85, 112-122.
- [3] Gao, B., Yin, A., Wang, Y., Tian, G., Woo, W. L., & Liu, H. (2014, June). Thermography spatial-transient-stage tensor model and material property characterization. In *2014 IEEE Far East Forum on Nondestructive Evaluation/Testing* (pp. 199-203). IEEE.
- [4] Chrysafi, A. P., Athanasopoulos, N., & Siakavellas, N. J. (2017). Damage detection on composite materials with active thermography and digital image processing. *International journal of thermal sciences*, 116, 242-253.
- [5] Garbe, C. S., Spies, H., & Jaehne, B. (2003, April). Estimation of complex motion from thermographic image sequences. In *Thermosense XXV* (Vol. 5073, pp. 303-317). International Society for Optics and Photonics.
- [6] Gao, B., Bai, L., Woo, W. L., & Tian, G. (2014). Thermography pattern analysis and separation. *Applied Physics Letters*, 104(25), 251902.
- [7] He, Y. Z., Tian, G. Y., Pan, M. C., Chen, D., & Luo, F. (2012). Signal reconstruction and feature extraction of pulsed eddy current thermography for aerospace composites. In *18th World Conference on Nondestructive Testing*. sn.
- [8] Fang, X., Paynabar, K., & Gebraeel, N. (2019). Image-based prognostics using penalized tensor regression. *Technometrics*, 1-29.

- [9] Zhang, H., Yang, R., He, Y., Foudazi, A., Cheng, L., & Tian, G. (2017). A review of microwave thermography nondestructive testing and evaluation. *Sensors*, 17(5), 1123.
- [10] Gao, B., He, Y., Woo, W. L., Tian, G. Y., Liu, J., & Hu, Y. (2016). Multidimensional tensor-based inductive thermography with multiple physical fields for offshore wind turbine gear inspection. *IEEE Transactions on Industrial Electronics*, 63(10), 6305-6315.
- [11] Zhou, T., & Tao, D. (2011, October). Godec: Randomized low-rank & sparse matrix decomposition in noisy case. In *Proceedings of the 28th International Conference on Machine Learning, ICML 2011*.
- [12] Vandereycken, B. (2013). Low-rank matrix completion by Riemannian optimization. *SIAM Journal on Optimization*, 23(2), 1214-1236.
- [13] Shu, X., Porikli, F., & Ahuja, N. (2014). Robust orthonormal subspace learning: Efficient recovery of corrupted low-rank matrices. In *Proceedings of the IEEE conference on computer vision and pattern recognition* (pp. 3874-3881).
- [14] Guan, N., Tao, D., Luo, Z., & Yuan, B. (2012). NeNMF: An optimal gradient method for nonnegative matrix factorization. *IEEE Transactions on Signal Processing*, 60(6), 2882-2898.
- [15] Motion-Based Multiple Object Tracking, Matlab Documentation, <https://www.mathworks.com/help/vision/examples/motion-based-multiple-object-tracking.html>, last accessed Sept. 7th, 2019
- [16] Sobral, A., Bouwmans, T., & Zahzah, E. H. (2016). Lrslibrary: Low-rank and sparse tools for background modeling and subtraction in videos. *Robust Low-Rank and Sparse Matrix Decomposition: Applications in Image and Video Processing*.

SIGNAL PROCESSING AND STORING OF HIGH DYNAMIC RANGE ACOUSTIC DATA FOR KNOWLEDGE DISCOVERY

I. Simeonov¹, T. Trifonov^{1,2}, T. Georgieva-Trifonova²

¹Vasil Levski National Military University, Veliko Tarnovo, Bulgaria
76, Bulgaria Blvd., 5000, Veliko Tarnovo, Bulgaria

Tel. +359 62 618724, Fax. +359 62 618899, E-mail: ivanov_ivan@nvu.bg

²St. Cyril and St. Methodius University of Veliko Tarnovo, Faculty of Mathematics and Informatics, 3, Georgi Kozarov str.,
BG 5000, Veliko Tarnovo, Bulgaria

E-mail: TihomirTrifonov@ieee.org, cv.georgieva@live.uni-vt.bg

Abstract

The purpose of this paper is to present some difficulties when signal processing and storing of high dynamic range acoustic data is performed for knowledge discovery.

Typical examples from musical acoustics, archaeoacoustics and battlefield acoustics are considered. The characteristic acoustic environment signature in the audio capture recording depending from background noise, reverberations and from concrete setup is discussed.

Some datasets consisting of the raw data and extracted metadata from bell ringing and gunfire, noise and voice recordings are built and shared in a data repository. Guidelines are outlined for using these data to apply data mining methods for discovery useful information. Possible directions for using these data to apply data mining methods for retrieving useful information are outlined.

The results can be used in various areas of acoustics, electrodynamics, image processing in medical diagnostics, systems of detection and localization of tactical firing systems on the battlefield, etc.

1. INTRODUCTION

In the recent years, our team has worked on several important projects [1, 2, 3] related to the application of modern acoustic methods in interdisciplinary fields. Studies aimed at the acoustics of the battlefield were also conducted. A large amount of experimental data has been accumulated. Acoustic signal processing has made it possible to draw interesting conclusions. However, it is laborious work and it is made by highly qualified experts.

In order to facilitate the users of this information, who are usually specialists in other fields (archeology, music, military, etc.), we decided to use the methods for knowledge discovery.

2. SOME PROBLEMS IN ACOUSTIC DATA RETRIEVING AND DATA PROCESSING

Various factors could affect how a sound wave attenuates with distance in outdoor and indoor environments.

For example, the interaction of the wave with objects, such as the ground, obstacles, effects of reverberations, first reflections, interference and diffraction, absorption and many others. On the other hand some factors as variations in temperature,

wind speed and direction, air pressure and humidity could affect. The sound picture is varying in accordance of type of concrete space: close, semi close or free space, in dependence of source and receiver points placement.

Some of effects were very difficult for formal analysis par example interactions within turbulence.

An understanding of how these factors change the sound pictures that are registered is important for the analysis of accumulated sounds.

The difficulty in computing these effects analytically for real-world situations, particularly the case in outdoor environments, means that experiments are important decision.

3. EXAMPLES OF EXPERIMENT DATA SETS FOR ANALISYS

It will regarded acoustic data set, one not big collection of signals, registered as a part of many experimental works, that was produced in the project "Thracians - genesis and development of ethnicity, cultural identities, interactions and civilizational heritage of antiquity", [2] Analogical sound phenomena observations was produced for bell sound in project "BELL – Research and Identification of Valuable

Bells of the Historic and Culture Heritage of Bulgaria and...”, [1,4], and for pulse noise from the training ranges of National military university, collected during the tactical exercises [5].

In closed spaces it can be observed two types of reverberation with different characteristics: early reverberation and late reverberation. Here is represented the experimental setup within close space inside the “Thracian tomb Griffins. The scheme of the tomb is shown on figure 1, where it can be seen the position of measuring microphone 4193 Brüel&Kjær and the source. Reverberation time RT60 was estimated by impulse measurement techniques. The pistol shot and balloon boom were made for obtaining the impulse responses of a camera.

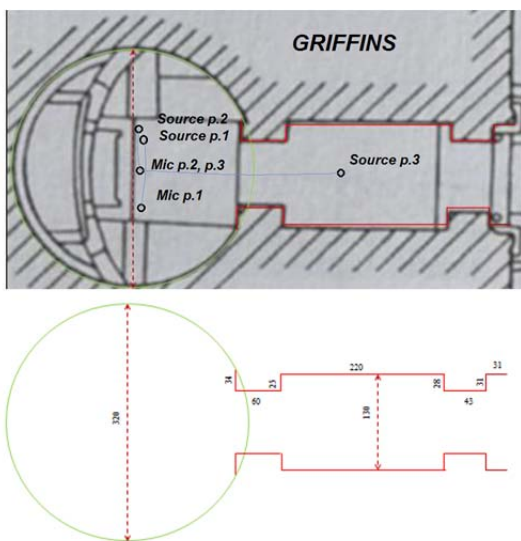
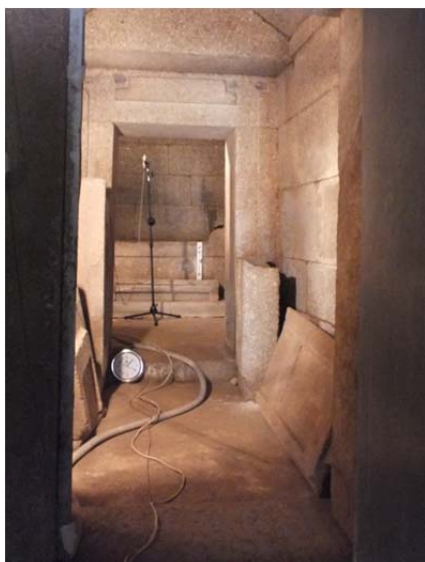


Figure 1. Measuring microphone disposition in “Thracian tomb Griffins” 42°42'19.8714"N 25°20'40.9554"E, 30 March 2016

The approximation of reverberation time RT60 was found in MatLab with the software - Signal Processing Utility Package V2 from Institute of Communication Systems RWTH Aachen University [6], see figure 2.

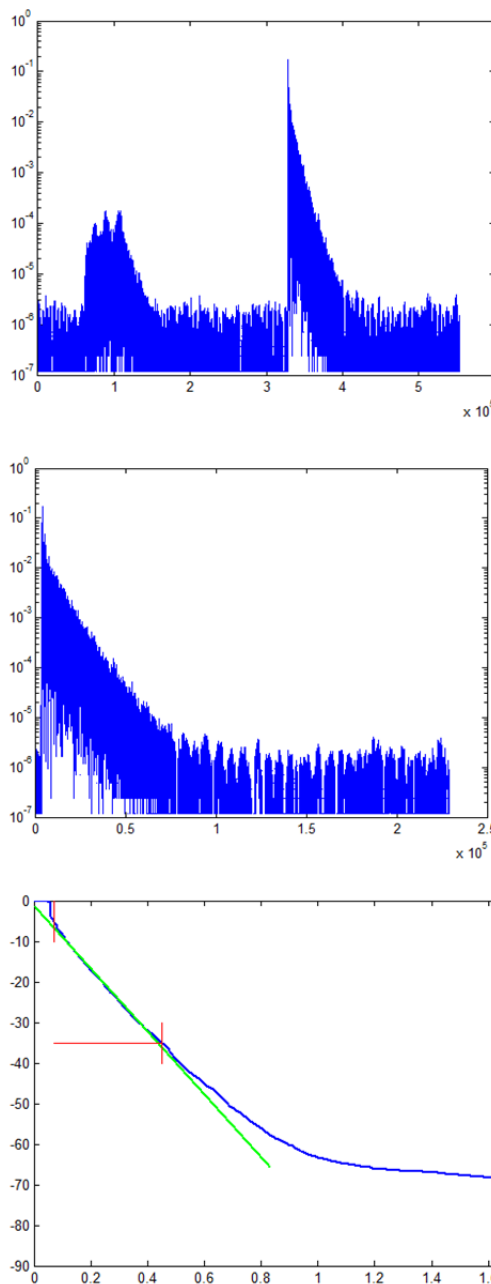


Figure 2. Signal waveforms from “tomb Griffins” (source p2 mic p2) and estimation of reverberation time RT60, 0.77s, $T_s=1/65536$ s

It was made experiments in larger close spaces – lecture hall 1121 (signal s3) and biggest theatre hall (signal s4) in National military university in V. Tarnovo and one free space musical improvisation in lawn near to Sveshari tomb (signal s5).

The results for RT60 approximation are seen in Table 1.

Table 1. The reverberation time RT60 estimation

name	RT60, s	Place
s1	0.774	Inside mound Thracian Tomb Griffins (before socialization), town Shipka, Province of Stara Zagora, Bulgaria, 2016
s2	no	Inside mound Thracian Tomb Griffins (after socialization), 2017
s3	0.802	Hall 1121 in Vasil Levski National Military University, Veliko Tarnovo, Bulgaria, 2018
s4	1.388	Inside biggest hall in National Military University, Veliko Tarnovo, 2018
s5	no	lawn near to Sveshari tomb no 13, Bulgaria, 2017

In the next it was made the analysis of a set of experiments where was investigated the energy characteristics of the different sound waves.

Wavelet Entropy is one known entropy measurement method by means of the discrete wavelet transform subband, [7]. The idea is that the accuracy of the selected wavelet basis is higher when the entropy is small.

Wavelet packet decomposition on one signal was defined as

$$d_{j,n}(k) = 2^{\frac{j}{2}} \int_{-\infty}^{\infty} s(t) \psi_n(2^{-j}t - k) dt,$$

$$0 \leq n \leq 2^N - 1$$

where j denotes the scale, n the band and k the surge parameter

Wavelet packet entropy, [7,8] is expressed as:

$$WPE_N = - \sum p_{j,n} \log p_{j,n}$$

where $p_{j,n}$ is relative energy

$$p_{j,n}(k) = \frac{E_{j,n}}{E_{tot}} = \frac{\sum_k |d_{j,n}(k)|^2}{\sum_n E_{j,n}}$$

Figure 3 shows wavelet packets for two parts of acoustic signal waveform see fig. 2 voice, noise and shot from small pistol, recorded inside the Thracian tomb Griffins. This raw data was exported in MatLab and here were determined Shannon entropy coefficients for the wavelet tree for Daubechies3 wavelet level 3.

Table 2. Description of the signals

Name	time, sec	contains	category	c_name
S1_all	8	Male voice and pistol shot	small	S1_1
S1_pulse	2	shot by small start pistol	small	S1_2
S1_noise	2	noise	small	S1_3
S1_voice	2	Male voice	small	S1_4
S2_pulse2	2	hand claps	small	S2_1
S2_pulse	2.076	hand clap	small	S2_2
S2_noise	2	noise	small	S2_3
S2_voice	2	Male voice	small	S2_4
S3_all	11	balloon boom	hall	S3_1
S3_pulse	2	balloon boom	hall	S3_2
S3_noise	2	noise	hall	S3_3
S4_pulse	2	balloon boom	hall	S4_1
S4_noise	2	noise	hall	S4_2
S5_pulse	2	hand claps	free space	S5_1
S5_noise	2	noise	free space	S5_2
S5_nois	1	noise	free space	S5_3
S5_noise_pause	0.563	noise	free space	S5_4
S5_music	2	kaval music	free space	S5_5
S5_music 2	2	kaval music	free space	S5_6

Analogically wavelet packet entropies for the five categories (totally 19 examples from S1_1 to S5_6) were calculated. Part of results is shown in table 3.

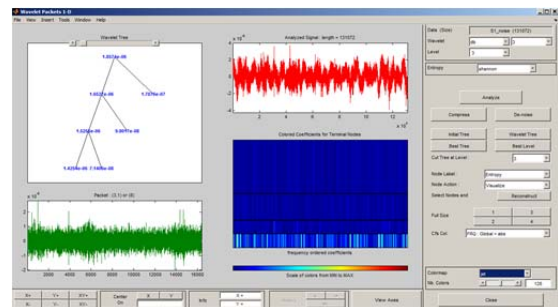
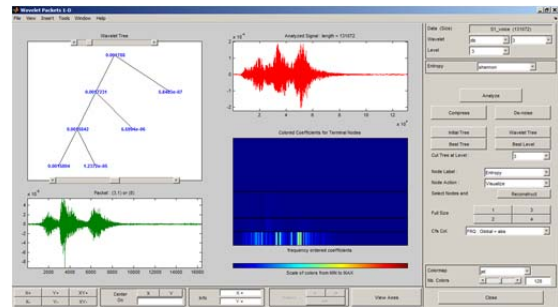


Figure 3. Calculated wavelet packets and Shannon entropies for waveforms correspondingly to fig. 2., Daubechies db3, level 3.

Table 3. The wavelet packets, Shannon entropies - db3,3.

c name	ShE(0,0)	ShE(1,0)	...	ShE(3,1)
S1_1	4.3306	3.7863		0.63957
S1_2	4.3288	3.7846		0.63956
S1_3	1.86E-06	6.53E-06		7.14E-08
S1_4	1.79E-03	1.72E-03		1.24E-05
S2_1	423.25	359.97		26.422
S2_2	223.14	189.37		13.105
S2_3	3.2667	3.0095		0.03363
S2_4	143.64	130.68		0.39973
S3_1	299.88	246.48		18.711
S3_2	299.73	246.66		18.51
S3_3	0.0326	0.02236		0.0031
S4_1	1220.2	910.8		91.656
S4_2	5.5622	4.5434		0.20388
S5_1	46.776	42.981		0.42473
S5_2	32.111	30.056		0.10593
S5_3	13.69	12.718		0.026823
S5_4	1.3329	1.2455		0.016731
S5_5	53.779	49.629		1.3118
S5_6	885.65	780.12		10.174

This wavelet packet entropies was regarded as attributes in data mining algorithm.

4. DATA MINING FOR ADDITIONAL ANALYSIS

The dataset, which consists of the signal characteristics (Table 2,3) extracted as described above, are further analysed by applying data mining algorithms. This dataset is used to build a data classification model for the purpose of automatically recognizing the type of location from which the signal is received. The previously defined categories are *small*, *hall*, *free space*; the first eight examples of the dataset, shown in Table 3 (s1_1, ... s2_4) are associated with the category *small*; s3_1, ..., s4_2 – *hall*; s5_1, ..., s5_6 – *free space*. The data classification is performed by creating a process by using RapidMiner [9] (<http://rapidminer.com>). The k-NN (*k*-Nearest Neighbours) algorithm is applied, which is based on comparing a given test example with training examples that are similar to it. The cosine similarity is used to measure the similarity. If $x(x_1, x_2, \dots, x_n)$ is a test example, $t(t_1, t_2, \dots, t_n)$ is an example from the training dataset, then the cosine similarity between them is computed by the following way:

$$\text{CosineSimilarity}(x, t) = \frac{\sum_{i=1}^n x_i t_i}{\sqrt{\sum_{i=1}^n x_i^2} \sqrt{\sum_{i=1}^n t_i^2}}$$

The validation of the trained model is done by the so-called cross validation, i.e. dividing the dataset into m subsets of equal sizes. One of these m subsets is kept as a test dataset. The remaining $m - 1$

subsets are used as training dataset. Then the cross validation process is repeated m times, using each of these m subsets exactly once as test data. The obtained m result from the executed m iterations is averaged to obtain a single estimate.

The following measures are computed to evaluate the validity of the classification model:

- *Accuracy* is defined by the ratio of the number of correctly classified examples (TP) to the total number of examples (N);

$$\text{Micro-average of accuracy} = (TP_1 + TP_2 + \dots + TP_m) / (N_1 + N_2 + \dots + N_m),$$

$$\text{Macro-average of accuracy} = (TP_1/N_1 + TP_2/N_2 + \dots + TP_m/N_m) / m,$$

where:

- TP_i is the number of correctly classified examples of the i -th iteration for $i = 1, \dots, m$;
- N_i is the number of the examples of the i -th dataset.
- *F-measure* is defined as the harmonic mean of the *precision P* and the *recall R*.

$$F = \frac{2 \cdot P \cdot R}{P + R},$$

where:

- The *precision P* is calculated as the ratio of the number of correctly classified examples of a given category to the number of all examples classified in that category;
- The *recall R* is calculated as the ratio of the number of correctly classified examples of a given category to the number of all examples that are actually in that category.

Usually, the *F-measure* is useful for uneven distribution of categories in the dataset.

The calculated results obtained for $m=5$, $k=1$, are shown in Table 4.

Table 4

	small	hall	free space
Precision	71.43%	100%	62.50%
Recall	62.50%	80.00%	83.33%
F-measure	66.67%	88.89%	71.43%

The computed values of the accuracy are:

Micro-average of accuracy: 73.68%;

Macro-average of accuracy: 75.00%.

5. CONCLUSION AND FUTURE RESEARCH

Table 4 shows that the Precision parameter is in the range of 62-100%, the Recall varies from 62 to 83% and the F-measure is between 67 and 89%. The obtained results show acceptable accuracy and warrant experimentation with more data and different classifiers. Other data mining methods may also be tried in the future.

In addition, there are many other important acoustic parameters, that can be investigated by applying the data mining methods.

Our future work will be related to their application in aerial and underwater acoustics, in interdisciplinary fields such as music, archeoacoustics, noise study of significant natural phenomena, ecology and others. Particular attention will be paid to the study of the acoustics of the battlefield, and in particular the detection, localization and classification of weapons systems.

REFERENCES

- [1] The Bell Project-Research and Identification of Valuable Bells of the Historic and Culture Heritage of Bulgaria and Development of Audio and Video Archive with Advanced Technologies, <http://www.math.bas.bg/bells/belleng.html>
- [2] Fol, V., György, G., Trifonov, T., Alexiev, A., Ivanov I.S., Acoustic Characteristics of Sacral Thracian Sites. AIS 2016 - 11th International Symposium on Applied Informatics and Related Areas, November 17, 2016, Székesfehérvár, Hungary, 84-87.
- [3] Trifonov T., I. Simeonov, N. K. Yordanov Advanced Signal Processing Methods For Analysis Of High Dynamic Range Acoustic Phenomena, Proc. 13th Conference on 'Communications, Electromagnetics and Medical Applications' (CEMA'18), Sofia, Bulgaria, 18-20 Oct. 2018, pp. 52-56, ISSN: 1109-1606
- [4] Dimkov G., T. Trifonov, I. Simeonov "Improving the Visualization of Scalograms by Means of Transformation in the Complex Plane", Proc. of the Forty Second Spring Conference, of the Union of Bulgarian Mathematicians, Borovetz, April 2-6, 2013, p.218. online at address http://www.math.bas.bg/smb/2013_PK/tom_2013/pdf/218-221.pdf.
- [5] Trifonov T., I. Simeonov, R. Dzhakov Features of Time-Frequency Analysis Visualization of Large Dynamic Range Signals, XLVII International Scientific Conference on Information, Communication and Energy Systems and Technologies (ICEST 2012), Veliko Tarnovo, June 2012, pp. 155-158,
- [6] Signal Processing Utility Package V2, Multi-Channel Impulse Response Database, Institute of Communication Systems RWTH Aachen University, 2019
- [7] Rizal, A., R. Hidayat, R., H.A Nugroho, Comparison of multilevel wavelet packet entropy using various entropy measurement for lung sound classification, International Journal of Advanced Computer Science and Applications 10(2), pp. 77-82, 2019.
- [8] Rosso, O. A., Blanco, S., Yordanova, J., Kolev, V., Figliola, A., Schürmann, M., & Başar, E. (2001). Wavelet entropy: a new tool for analysis of short duration brain electrical signals. *Journal of neuroscience methods*, 105(1), 65-75.
- [9] Markus Hofmann, Ralf Klinkenberg, RapidMiner: Data Mining Use Cases and Business Analytics Applications, CRC Press/Taylor & Francis Group, 2014.

AN EXPERIMENTAL STUDY OF IMPROVING SOUND INSULATION INDEX OF HOLLOW BRICK WALL BY USING WALL LINING PANELS FOR ACOUSTIC SENSITIVE ROOMS IN HOSPITALS

Snezhana Pleshkova, Aleksandar Vasilev Kirechev

Faculty of Telecommunications, Technical University of Sofia
8 Bulevar Kl. Ohridski, 1000 Sofia, Bulgaria

T.+359 895588851; E. snegpl@tu-sofia.bg
T.+359 883304706; E. a.kirechev@gmail.com

Abstract

The main construction material between dwelling apartments and hospital rooms in Bulgaria which is not part of the skeleton structure is ceramic hollow bricks. According to National standard the minim sound reduction index between dwellings has to be $R'w > 53\text{dB}$ for residential buildings and walls between hospitalization rooms $R'w > 47\text{dB}$.

Most of the brick on the market has maximum sound insulation index calculated and measured is around $R'w = 46\text{dB}$ which don't meet the regulations.

There is different approaches to solve this issue. Some of them include splitting the wall and making double masonry wall, other is to make wall lining with steel studs, mineral wool and gypsum board. They all have their advantages and disadvantages but the focus of this paper will be new type of sound insulation system which can increase significant the performance of the wall with minimum thickness. The experiment study is cared in laboratory and in on site measurements. Results shown great promises for wall lining panels and same conclusions for influence of wall connections.

1. INTRODUCTION

In Bulgaria the walls between apartments for every new building has to be made with minimum thickness of 250mm. Based on architectural plan and civil engineering project wall between apartments are made from rainforest concrete, part of skeleton of building, and ceramic hollow bricks. In the case of rainforest concrete walls the calculated and measured noise insulation index is more than $R'w > 58\text{dB}$ but in cases where the ceramic hollow brick walls are installed the noise reduction index is less than $R'w < 49\text{dB}$. According to national standard the minim apparent sound reduction index between dwellings has to be $R'w > 53\text{dB}$ and where the requirements are not met the sound insulation has to be increased. In this work, we present same experimental results related with different technics for increasing sound insulation index of hollow brick walls measured in laboratory conditions according to EN ISO 10140-3 [1] and field measurements according to EN ISO 16283-1 [2]. Because every wall and every room has different structure, arrangement of bricks, flanking transmission, all result will be compare only for sound insulation different $\Delta R'w$.

Because of minimum dimensions of rooms the following test will focus only on sound insulation sys-

tems from 30 to 80mm, which cannot be achieved with conventional wall lining metal frame. The panels are specially design with combination of high density gypsum fibreboard and absorber material in air gap.

2. HOLLOW BRICK NOISE INSULATION

2.1. Laboratory measurements

Laboratory measurements are carry out according to EN ISO 10140-3 in test chamber with volume of source room $V_1 = 164 \text{ m}^3$ and volume of receiving room $V_2 = 119 \text{ m}^3$. The opening for test walls is with aria of $S = 10.92\text{m}^2$.

Tested masonry wall has following materials with their properties:

Table 1. Material properties

Type of material	Parameters				
	Thickness (mm)	Density (kg/m ³)	E module (GPa)	Coeff. of Poisson	Internal loss
Hollow bricks	250	625	6.85	0.12	0.02
Gypsum Plaster	20	700	1.5	0.22	0.01



Figure 1. Typical ceramic hollow brick used in conventional residential buildings and in this experimental study

Detail drawing of masonry wall is shown on figure 2:

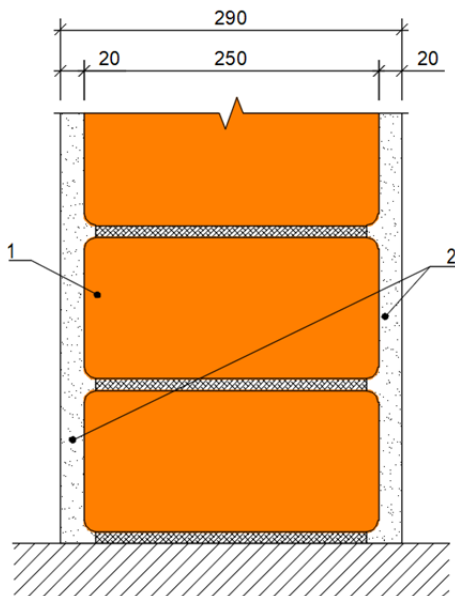


Figure 2. Detail of masonry brick (1) wall with gypsum plaster (2).

2.2. Field measurements

Field measurements are carried on three different apartments with different wall sizing, room configuration and different reverberation time. Despite that all three has close sound insulation index because of similarity of wall materials.

The figures 3 and 4 the configuration of three apartments are shown.

The measurement follow strictly EN ISO 16283-1 and they are carried.

In all three cases the residents are complaining of intelligibility of speech noise. Because there is no information about the types of hollow bricks and plasters covering the property of walls are not reviewed.

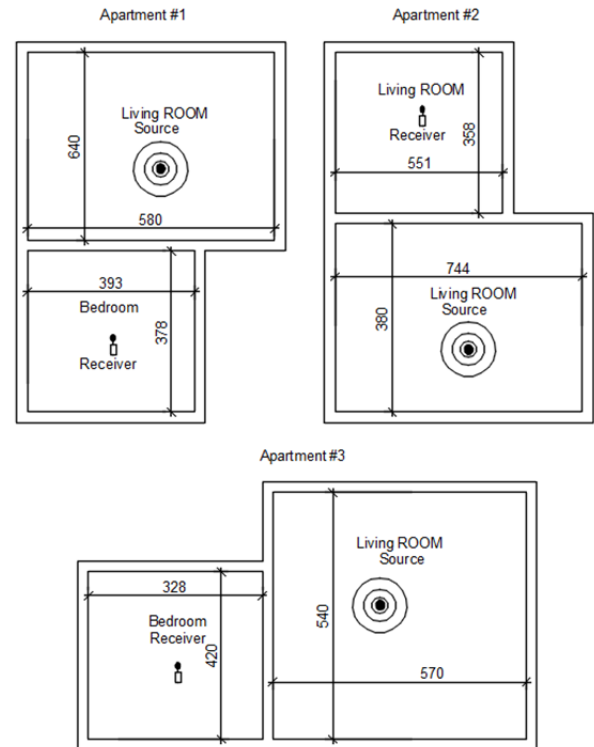


Figure 3. Field measurement in: apartment #1 with high $H=2.58\text{m}$, apartment #2 with high $H=2.45\text{m}$, apartment #3 with high $H=2.55\text{m}$

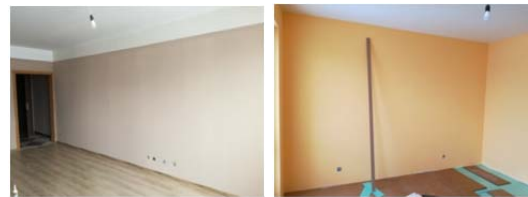


Figure 4. Photo of source and receiver room of apartment #1

3. WALL LINING PANELS

3.1. Laboratory measurements

Four different cases are measured in laboratory conditions in order to choose best wall panel for field measurements. Panels are made from one layer of open cell elastic polyurethane foam, one layer of gypsum fibreboard and finish layer of gypsum plasterboard.

Basically the wall lining panels can be divided into two groups. First group - panels glued to brick wall and second group - panels fix on brick wall with special elastic point connection made of rubber elastomer. Following tables shows system configuration with all materials and type of connections.

Table 2. System configurations

System Name	Thickness of system (mm)	Layers (from wall to room)	Thickness (mm)	Type of connection
M1	42.5 mm	Air	0 mm	Glue to wall
		Polyurethane foam	20 mm	
		Gypsum fiberboard	10 mm	
		Gypsum Plasterboard	12.5 mm	
M2	45 mm	Air	10 mm	Elastic rubber point connection
		Polyurethane foam	10 mm	
		Gypsum fiberboard	12.5 mm	
		Gypsum Plasterboard	12.5 mm	
M3	55 mm	Air	10 mm	Elastic rubber point connection
		Polyurethane foam	20 mm	
		Gypsum fiberboard	12.5 mm	
		Gypsum Plasterboard	12.5 mm	
M4	85 mm	Air	10 mm	Elastic rubber point connection
		Polyurethane foam	50 mm	
		Gypsum fiberboard	12.5 mm	
		Gypsum Plasterboard	12.5 mm	

The goal is to compare two camper the two types of connections and for the second group to compare how different air gaps change sound insulation.

In following figures the details for all four system are presented.

All measurement are carried in same conditions as masonry brick wall.



Figure 5. Photo from laboratory with installation of system M2

3.2. Field measurements

Field measurements are made only with one type of panels which shown best results – Panel M3.

In all three cases the wall lining panels are placed on side of the source in order to avoid direct flanking transmission from side wall.

Pictures of one of the sites showing installation of panels in progress.



Figure 6. Photo

4. TEST RESULTS

4.1. Laboratory measurements

The measured results of masonry hollow brick wall are shown on “Figure 7”

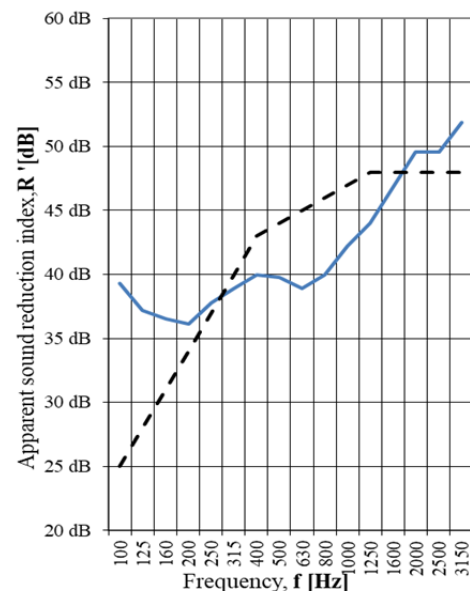


Figure 7. Graphic of apparent sound reduction index of masonry wall

Results of all group and types of wall lining panels are shown on “Figure 8”.

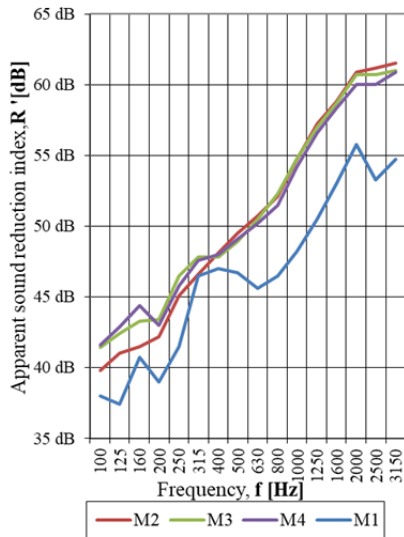


Figure 8. Graphics of apparent sound reduction index of masonry wall with installed wall panels

The weighted noise reduction index is carried according to EN ISO 717 -1 and the results are shown on "Table 3".

Table 3. Laboratory test results

	Hollow bricks	Hollow bricks + M1	Hollow bricks + M2	Hollow bricks + M3	Hollow bricks + M4
R _w	44dB	49dB	54dB	54dB	54dB
C, C _{tr}	-1;-3	-1;-3	-1;-4	-1;-4	-1;-3
ΔR _w	-	5dB	10dB	10dB	10dB

The following graphic is made to show noise reduction different between hollow brick and every type of wall lining.

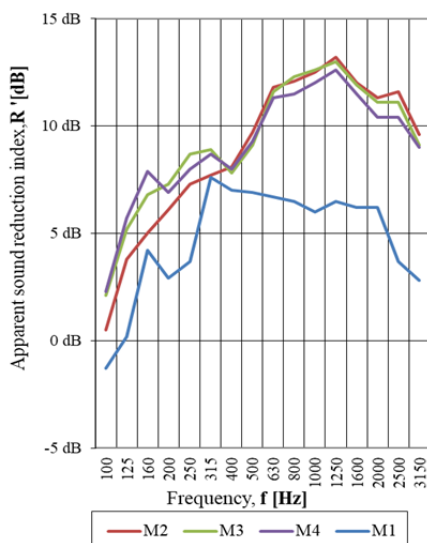


Figure 9. Graphics of spectral noise insulation improvement

4.2. Field measurements

All three cases shown different noise reduction graphs and sound insulation index. The following graphics shows measurement of brick walls before sound insulation and after installation of wall lining panels M3.

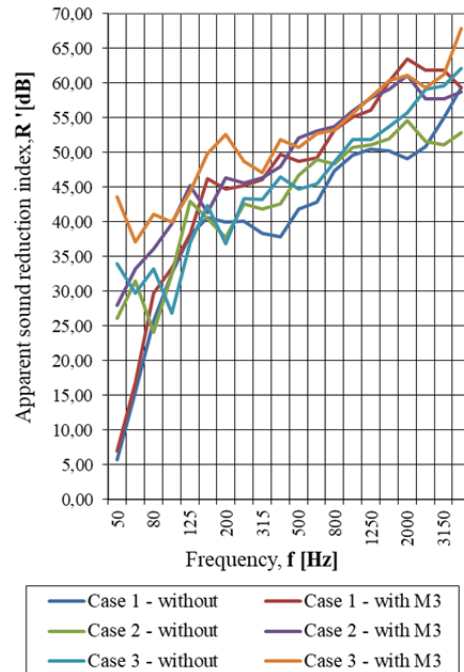


Figure 10. Graphic of apparent sound reduction index

Results are presented in Table 4, where sound reduction index is carried according to EN ISO 717 -1 [3].

Table 4. Field test results

	Type of wall	R _w	C, C _{tr}	ΔR _w
Case 1	Hollow brick wall	47dB	-1;-3	7dB
	Hollow brick wall + M3	54dB	-1;-5	
Case 2	Hollow brick wall	49dB	-1;-3	6dB
	Hollow brick wall + M3	55dB	-1;-4	
Case 3	Hollow brick wall	48dB	0;-4	8dB
	Hollow brick wall + M3	56dB	-1;-4	

5. DISCUSSION OF RESULTS

According to laboratory measurement there is big difference between system M1 and other three.

This result shows the how type of conation between the masonry wall and insulation system influent the end result.

Laboratory test also shows that despite the big difference of air gap (40mm) between M2 and M4 the weighed sound level index and in most of the spectrum (from 200Hz to 4000Hz) there is no significant difference. This result can be explain with two models of theoretical expression of transmission loss of double panel by Beranek [4] and Work and London [5]

Laboratory test also shown that the optimum Panel system, considering full spectrum transmission loss is Panel M3, that's why all on side measurement are carried with this system.

On site measurement shown that all brick walls have better performance than this in laboratory this is because in the apartments different bricks are used and the plaster cover is greater. However all three case the requirements are not met and the occupants of the apartments have complains about speech intelligibility from adjacent apartment.

In all three cases the less than laboratory test because of flanking transmission. The weighted noise level difference (ΔR_w) is different in every case, but from 200Hz to 4000 Hz the results have good comply. Despite that all measurement are made according EN ISO 16283-1 many factors can explain the difference in noise reduction of frequencies under 200 Hz.

6. CONCLUSION

Test results from laboratory measurements show that type of connection have significant influence upon increasing sound insulation index in thick wall systems. The test shows that for the system M1 the minimum requirement from regulation is not met and for the system from M2 to M4 the requirement is met for residential apartments and hospitalisation rooms. The optimal wall system considering thickness and noise reducing efficiency is wall system M3.

On site results shows that the sound insulation index with system M3 are less effective than the results shown is laboratory tests. But despite that the average increasing in sound level index is 7dB and the minimum requirements are met.

Become of laboratory test future work will focus on studding how and witch properties of rubber connection will affect the transmission loss index in order to achieve better results.

REFERENCES

- [1] EN ISO 10140-3:2015
- [2] EN ISO 16283-1:2014
- [3] EN ISO 717 -1:2013
- [4] L. Beranek and G. Work, Sound transmission through multiple structures containing flexible blankets, *acoust. Sot. Am.* 21, 419.,1949
- [5] A. London, Transmission of reverberant sound through double walls., *acoust Sot. Am.* 22, 270., 1950
- [6] V. Hongisto, Airborn sound insulation of wall structures-measurment and prediction methods, Espoo 2000, Report 56, Finland, 2000
- [7] V. Hongisto, The calculation of the sound insulation of double panels – comparison of the existing models, *inter.noise 2000*, Finland, 2000
- [8] A. Wamck, Sound transmission loss measurements through 190 mm and 140 mm blocks with added dry-wall and through cavity block walls, Internal Report No. 586, Council Canada, 1990

COMPARISON BETWEEN APPLICATION OF GIRDLE COIL AND SEVERAL LOCAL INDUCTORS IN MAGNETOTHERAPY

Dimitar Dimitrov

Technical University of Sofia
1000 Sofia, 8, Kliment Ohridski str.

dcd@tu-sofia.bg

Abstract

It's well known that the girdle coil and/or several local inductors are most used in magneto-therapy. In formal point of view there is not any difference between application of these two kind of inductors. There are only difference in constructions of these two kind inductors. Often the physicians prefers to use girdle coil because its application is more friendly for the patient. The nurse prefers to use girdle coil because its application is more easy than application of several local inductors. In principally the girdle coil can provide influence of electromagnetic field on more large area of the human body. Nevertheless in many cases the physicians prefers applications of local inductors. For instance in stomatology can be used only local inductors. Often in surgery physicians prefers application of local inductors, also. The comparison between properties of girdle coil and local inductors is the main goal of present investigation.

1. INTRODUCTION

Comparison between the two kind of inductors should consists not only comparison between two construction. More important is comparison between space configuration of magnetic field created by the two different inductors in patient's area. This space configuration of magnetic field can be obtained using appropriate computer visualisation of magnetic field of both local inductors and girdle coil. In the process of discussion on influence of magnetic field on the human body in the case of two kind of inductors it's necessary to take in account vector of velocity of ions of blood and ions of other kind of liquid of human body in the area of influence of magnetic field.

2. BASIC MATHEMATICAL DESCRIPTION OF INFLUENCE OF MAGNETIC FIELD ON THE MOVEMENT OF IONS IN LIVE TISSUES

It is known from electrotechnics the equation (1) for determination of the force \vec{F} of influence of magnetic field with magnetic induction \vec{B} on ion with electric charge q which moves in the magnetic field with velocity \vec{V} .

$$\vec{F} = q(\vec{V} \times \vec{B}) \quad (1)$$

It follows from the equation (1) that this force \vec{F} would be maximal when the vector of velocity \vec{V} of the moving ion and the magnetic induction \vec{B} are

perpendicular. If the mass of the moving ion is m then the acceleration \vec{a} given by the force \vec{F} is:

$$\vec{a} = \frac{\vec{F}}{m} \quad (2)$$

Thus, a new component \vec{V}_n of the ion's velocity in the living tissue appears:

$$\vec{V}_n = \vec{a}t \quad (3)$$

Where t is the time.

Formally, the effect of external magnetic field on the moving ion in living tissue is expressed by adding the new component to its initial velocity. Thus, the final value of velocity of ion movement in living tissue can be determined by the equation (4).

$$\vec{V}_R = \vec{V} + \vec{V}_n \quad (4)$$

It's well known in medicine, that the physiological effect of the influence of external factors (in particular the influence of external low-frequency or permanent electric and magnetic fields) depends on the change in the rate of movement of the ions in the tissues due to these effects. In this case, the equation (4) illustrates the basic principle of magnetotherapy, namely that the physiological effect of the influence of the low-frequency magnetic field on the living tissue depends to the new component \vec{V}_n of the speed of movement of ions. If the equation

(1) and (2) are replaced successively in the equation (3), the equation (5) can be obtained:

$$\vec{V}_n = \frac{q(\vec{V} \times \vec{B})}{m} t \tag{5}$$

Basic remarks:

1. From the equation (5), it can be seen that the new component of the travel speed, resp. the physiological effect of magnetic field effects on living tissues depends on:

1.1. Electric charges q and mass m of specific ions.

1.2. The value of magnetic induction \vec{B} and the value of the initial ionic velocity \vec{V} , which in turn depends on the temperature of the tissues.

1.3. Angle between the vectors of magnetic induction \vec{B} and the initial velocity \vec{V} of the ions.

1.4. If at least one of the two magnetic induction vectors \vec{B} and l or the initial ionic velocity \vec{V} changes, this results in a change in the new travel speed components, respectively. the physiological effect of magnetic field effects on living tissues.

3. COMPARISON BETWEEN BASIC PROPERTIES OF GIRDLE COIL AND SYSTEMS OF SOME LOCAL INDUCTORS

On Fig. 1 can be seen application of girdle coil in magneto-therapy. On Fig. 2 can be seen electronic unit of system for magneto-therapy together with local inductors.

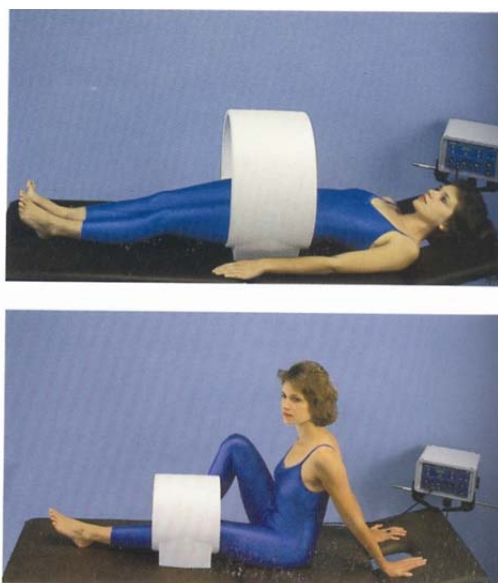


Fig.1. Magneto-therapy using girdle coil



Fig. 2. Electronic unit of system for magneto-therapy together with local inductors

3.1. Basic properties of girdle coil

1. It can be seen on Fig.1 that the application of a girdle coil provides a low frequency magnetic field effect on a relatively large area of the human body, but the therapy is of limited effectiveness due to the small angle values between the magnetic induction vector and vector of the initial ionic velocity of blood at most points of the impact area of the magnetic field [9].

2. Changing the space configuration of the magnetic field created by the girdle coil (the "moving" magnetic field mode) can only provide a simple "motion" of the magnetic field – only along the coil axis.

3.2. Basic properties of systems of some local inductors

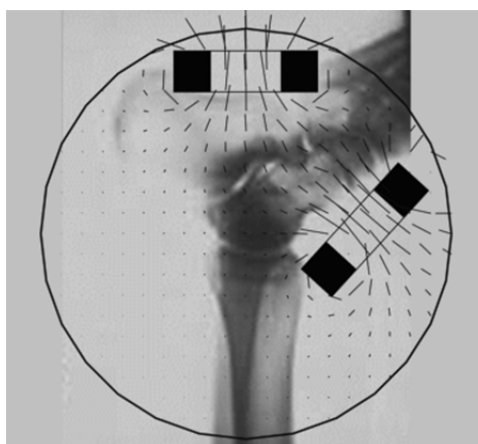


Fig. 3. A simple application of pair local inductors

1.The application of one or a pair of local inductors provides magnetic field impact on a small area of the body, but local inductors can easily be positioned such that the vectors of magnetic induction and initial ionic velocity are nearly perpendicu-

lar (Fig.3), providing an increased effectiveness of the therapeutic process [6,7].

2. The application of local inductors allows the use of a different number of inductors suitably located around the field of magnetic field action. This practically provides unlimited possibilities for forming the spatial configuration of the magnetic field in the patient area.

3. The use of a plurality of local inducers suitably located in the patient region allows a number of combinations to be formed by varying their number by switching with respect to the instantaneous spatial configuration of the magnetic field in the subject area including rotation and translation of the field. This allows a longer therapy process to be used without adaptation of the body to the influence of magnetic field.

4. Of course increasing the number of local inductors used complicates their management. However, this disadvantage can be easily avoided by using microprocessor control of the magnetotherapy system modes [8,10].

5. The microprocessor control of magnetic therapy systems allows not only changes in the spatial configuration of the magnetic field in the patient area but also changes in the parameters of excitation current in the inductors (amplitude, frequency, signal form). Practically, with the use of appropriate software, multiple modes of therapy can be provided [11,12].

4. SYSTEM FOR MAGNETOTHERAPY WITH "RUNNING" MAGNETIC FIELD

This system (Fig.4) can be an example about application of limited number of local inductors using microprocessor control of the magnetotherapy system.

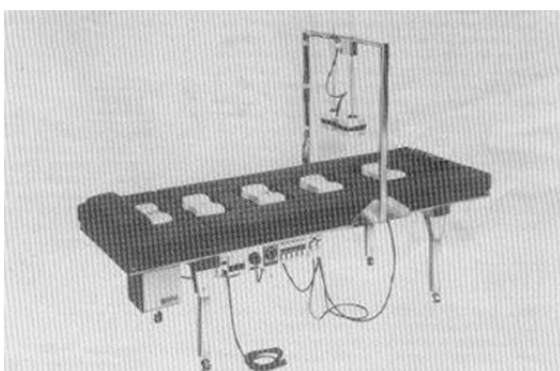


Fig. 4. System for magneto-therapy with "running" low frequency magnetic field

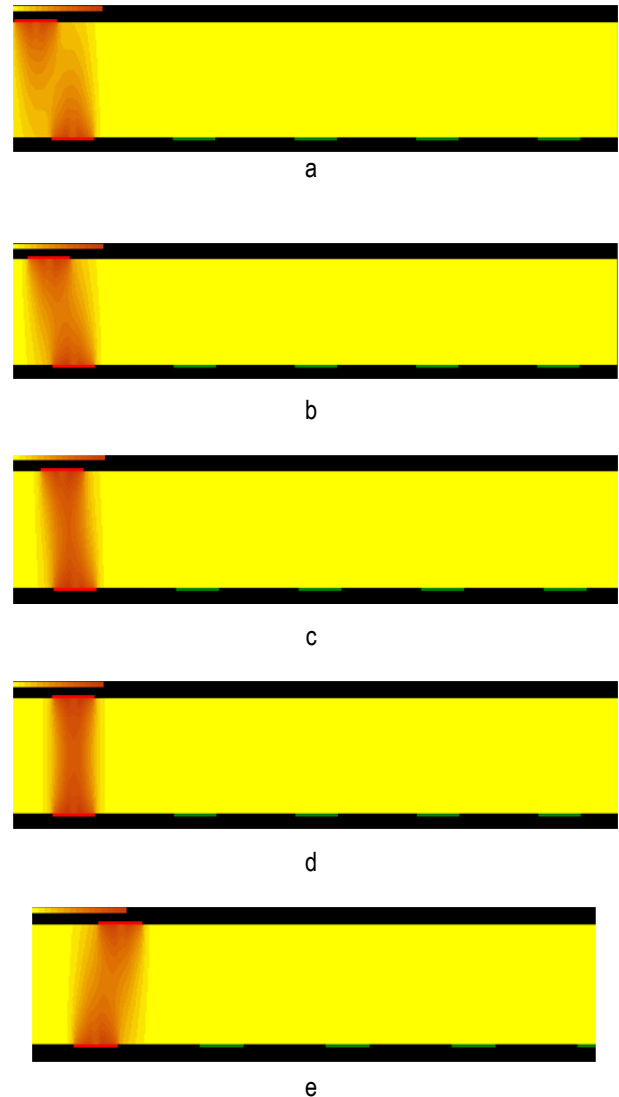


Fig. 5 (a,b,c,d,e). Visualisation of "running" low frequency magnetic field on the axis of bed

The spatial location of the local inductors in the patient area in the proposed random "running" magnetic field system is chosen considering the above mentioned in 3.2 properties of system build by local inductors [1,2,3,4,5]. The aim is to provide not only the possibility of rotating the magnetic induction vector in a plane perpendicular to the axis of the bed, but also moving said plane of rotation of the magnetic induction vector longitudinally along the axis of the bed. Thus, system application can be provided for multiple diseases, regardless of which part of the patient's body is concerned. At the same time, thanks to the microprocessor control of the system, there are quite a number of modifications of the spatial-time configuration of the magnetic field in the patient's body. The microprocessor control of spatial field configurations of the magnetic induction vector field implies the possibility of 3D pseudo-random changes in spatial field configurations of the magnetic induction vector field, resulting in im-

proved therapeutic results and more severe cases of disease.

5. CONCLUSION

It's clear that the construction of system with "running" low frequency magnetic field is more complicated and more expensive than girdle coil. In addition this system need microprocessor control as advantage and as disadvantage.

The system with "running" low frequency magnetic field can provide not limited modes of programs for therapy on the base of appropriate software, which is impossible in the case of application of girdle coil.

The conclusions made above are of a general nature and should be taken into account at all in the study, comparison and synthesis of different systems of magnetotherapy. These conclusions are also important when interpreting trajectories of movement of various ions in living tissues, also.

6. ACKNOWLEDGMENTS

The author would like to thank the Research and Development Sector at the Technical University of Sofia for the financial support.

REFERENCES

- [1] A. Dimitrov, K. Dimitrov, Methods and algorithms for generation of random low frequency series of signals for magnetotherapy, „Journal of Applied Electromagnetism“, Greece, ISSN 1109-1606, Volume 15, No. 2, December 2013, p. 34-43
- [2] A. Dimitrov, Design of power unit of system for therapy using "running" low frequency magnetic field, Proceedings of 7th International Conference "Communication, Electromagnetics and Medical Application CEMA'12", ISSN 1314-2100, Athens, November 8th-10th, 2012, p.110-113
- [3] A. Dimitrov, Algorithms for management and control of system for therapy by "random" running low frequency magnetic field, Proceedings of 6th International Conference "Communication, Electromagnetics and Medical Application CEMA'11", ISSN 1314-2100, Sofia, October 6th-8th, 2011, p.26-30
- [4] A. Dimitrov, Method for design of system for therapy using "random" running low frequency magnetic field, Proceedings of 6th International Conference "Communication, Electromagnetics and Medical Application CEMA'11", ISSN 1314-2100, Sofia, October 6th-8th, 2011, p.31-34
- [5] A. Dimitrov, K. Dimitrov, Method for design of system for magnetotherapy using "running" random low frequency series of signals, Proceedings of 8th International Conference "Communication, Electromagnetics and Medical Application CEMA'13", ISSN 1314-2100, Sofia, October 17th-19th, 2013, p.26-30
- [6] B. Kudrin, A. Dimitrov, An algorithm for visualization of low frequency magnetic signals in system for magnetotherapy, Proceedings of 8th International Conference "Communication, Electromagnetics and Medical Application CEMA'13", ISSN 1314-2100, Sofia, October 17th-19th, 2013, p.31-35
- [7] B. Kudrin, A. Dimitrov, Computer visualization of low frequency magnetic signals in system for magnetotherapy with variable parameters, Proceedings of 8th International Conference "Communication, Electromagnetics and Medical Application CEMA'13", ISSN 1314-2100, Sofia, October 17th-19th, 2013, p.36-39
- [8] Guergov, S. Acupressure in magneto therapy environment, Series on Biomechanics, Peer-reviewed Journal Edited by Bulgarian Academy of Science, Vol.32, No.1 (2018), p.16-19"
- [9] Atanas Dimitrov, Sasho Guergov, One application of influence of low frequency magnetic field on the head, Proceedings of 14th International Conference "Communication, Electromagnetics and Medical Application CEMA'19", ISSN 1314-2100, Sofia, October 17th-19th, 2019, p.30-34
- [10] Atanas Dimitrov, Sasho Guergov, Some Possibilities for Optimisation of Application of Girdle Coil in Magnetotherapy, Proceedings of 14th International Conference "Communication, Electromagnetics and Medical Application CEMA'19", ISSN 1314-2100, Sofia, October 17th-19th, 2019, p.35-39
- [11] Bekiarski Al., Sn. Pleshkova, Sv. Antonov. "Real Time Processing and Database of Medical Thermal Images", 4rd International Conference on Communications, Electromagnetics and Medical Application'11, Sofia, 2011, pp.101-106
- [12] Bekiarski Al., Sn. Pleshkova. Moving Objects Detection and Tracking in Infrared or Thermal Image. 5th World Conference: Applied Computing Conference (ACC '12), University of Algarve, Faro, Portugal, 2012, pp. 128-132

SOME POSSIBILITIES FOR OPTIMISATION OF APPLICATION OF GIRDLE COIL IN MAGNETO-THERAPY

Atanas Dimitrov, Sasho Guergov

Technical University of Sofia
1000 Sofia, 8, Kliment Ohridski str.

sguergov@tu-sofia.bg

Abstract

The girdle coils are often used in magneto-therapy. The basic advantage of this coils is possibility for providing of influence of low frequency magnetic field on big part of the human body. In addition it's easy to provide movement or / and static disposition of the girdle coil on axis of the human body. During the procedures of therapy usually both the axis of girdle coil and axis of human body are parallel. It's well known that both the axis of vector of magnetic induction for more of the points in the middle are of the girdle coil and axis of coil are the same or parallel. It's well known that the influence of magnetic field is first of all on the movement of ions of blood. In the case of ordinary application of girdle coil, the direction of movement of blood in the big blood vessels in the human body, in the hand and in the legs would be also parallel of the direction of magnetic induction or the angle between vector of magnetic induction and direction of movement of blood in the big blood vessels in the human body, in the hand and in the legs would be too small. Therefore the results of therapy using ordinary girdle coil are not optimal. This is the biggest disadvantage of allocation of girdle coil in magneto-therapy. The goal of this paper is to present some possibility for optimization of application of girdle coil in magneto-therapy.

1. INTRODUCTION

The magnetic device (girdle coil) which is constructed for use as a therapeutic tool in magneto-therapy can be seen on Fig. 1. Usually both the axis Z of girdle and axis of human body are parallel. The current in girdle coil is I and the radius of girdle coil is R. The space-temporal configuration of low frequency magnetic field in the patient's area is very important in the process of magneto-therapy [1,2]. Therefore the precise calculations of low frequency magnetic field as well as an easy-understand visualization of field distribution over the patient's area are of great importance for the reliability and predictability in the process of experimental measurement of magnetic induction of the constructed electromagnetic device.

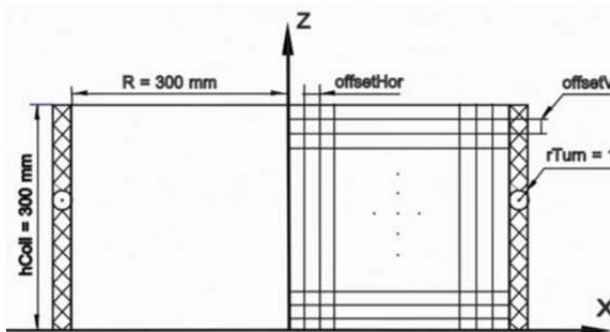


Fig.1. Girdle coil

The calculation exposes a low frequency magnetic field solver that allows evaluating the field strength throughout the volume influenced by the coil [1,2,3]. The presented article illustrates one approach to calculate and visualize a low frequency magnetic field distribution in 2D.

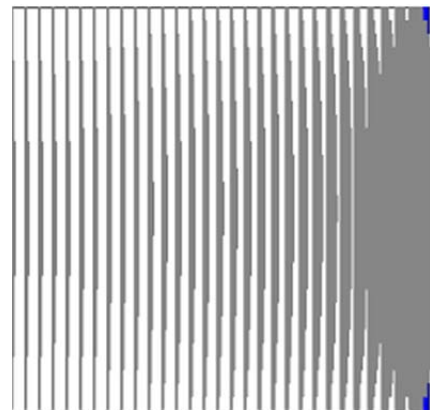


Fig. 2. Experimental histogram of the module of magnetic induction in the case of static activation of the girdle coil

The histogram of experimental measurements of amplitude of the module of magnetic induction in the plane XOZ (Fig. 1) can be seen on Fig. 2 [1,3]. It's clear that this histogram is constant in the time. Because of that there is possibility for fast adaptation of patients to parameters of low frequency magnetic field during process of therapy. This is the second disadvantage of application of ordinary

girdle coil. For experimental investigation a small coil (diameter $d = 8\text{mm}$, height $h = 10\text{mm}$ and current turns $w = 2 \times 300$) has been used as sensor for measurement of the value of magnetic induction. This coil has been connected with the inputs of differential amplifier in the input of apparatus for measurement of magnetic induction of low frequency magnetic field. The measurement has been done for the sinusoidal current in the girdle coil with frequency $f = 50\text{Hz}$. It's well known that the frequency band $f = 10\text{Hz} - 100\text{Hz}$ is used in the process of magneto-therapy. The sensor has been putted in different points around the girdle coil. The mechanical construction of the girdle coil with the main mechanical sizes can be seen on Fig. 3.

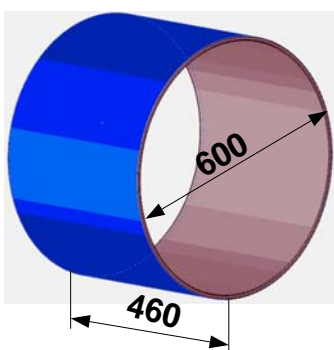


Fig. 3. Mechanical construction of girdle coil

2. ON OPTIMIZATION OF APPLICATION OF GIRDLE COIL IN MAGNETOTHERAPY

Taking in account Fig. 3 it's clear that mechanical construction of girdle coil is hard. Because of that the optimisation of application of girdle coil would be possible only on the base of optimisation of space temporal function of current in the coil. One new method in physiotherapy is simultaneously application of low frequency magnetic field together with mineral water. The application of low frequency magnetic field provide increasing of the module of velocity of ions in the liquids of human body (first of all ions of the blood). Because of that there is increasing of the velocity of biochemical processes in the body. When the human body is in the mineral water (Fig. 4) there is diffusion of components (ions) of mineral water through the skin [4,5,6]. Therefore there is biochemical processes in the human body with participation of ions of mineral water. As results the simultaneously application of low frequency magnetic field together with mineral water protects therapy by mineral water.



Fig. 4. Application of girdle coil is in the process of magneto-therapy together with mineral water

During of above described process of simultaneously therapy by mineral water and low frequency magnetic field it's necessary to be avoided adaptation of patient's body to the influence of magnetic field [7,8]. In this case it would be possible to provide more long process of therapy and to obtain more good effect of therapy. The adaptation of patient's body to the influence of low frequency magnetic field can be avoided if there is "movement" of magnetic field during the therapy. This "movement" would be one optimisation of application of girdle coil in magnetotherapy. This optimisation can be provided if the construction of girdle coil consists several part one the one axis and if every part create independent low frequency magnetic field. This construction of girdle coil can provide "movement" of low frequency magnetic field on the axis of the coil.

3. GIRDLE COIL WITH "MOVEMENT" OF MAGNETIC FIELD



Fig. 5. Girdle coil with "movement" of low frequency magnetic field on the coil's axis

The construction of girdle coil (2) with "movement" of magnetic field and electronic unit (1) for magnetic field management can be seen on Fig. 5. As mentioned above, the therapeutic outcome may be improved by providing the possibility of changing the parameters of the effecting magnetic field if appropriate periodic magnetic signals are used. When applying a girdle coil, this can be provided by sectioning the coil and sequentially agitating the individual sections in a pre-selected order. These types of coils could be used to provide the "waving wave" mode by sequential or pseudo-random excitation of the individual coil sections. For this case of a multi-layer coil, the calculation of the magnetic field is performed for a separate section. Because the coil contains 5 sections activated sequentially, the visualization is based on once-calculated and stored data and reproduces an identical picture of the field but displaced along the Z axis (Fig. 1). Figure 6 (a, b, c, d, e) shows the results of the field calculation for each of the 5 identical sections. The field preview is animated to match the coil section of the coil sections.

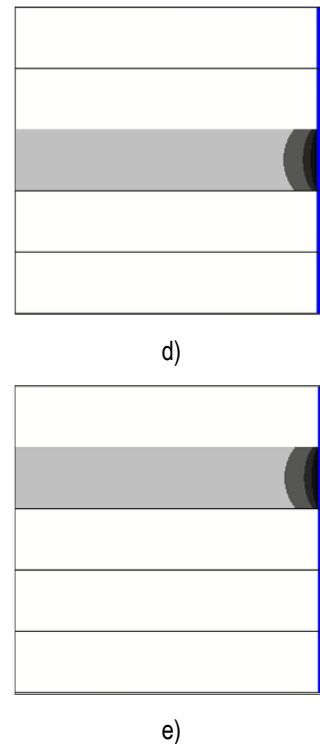
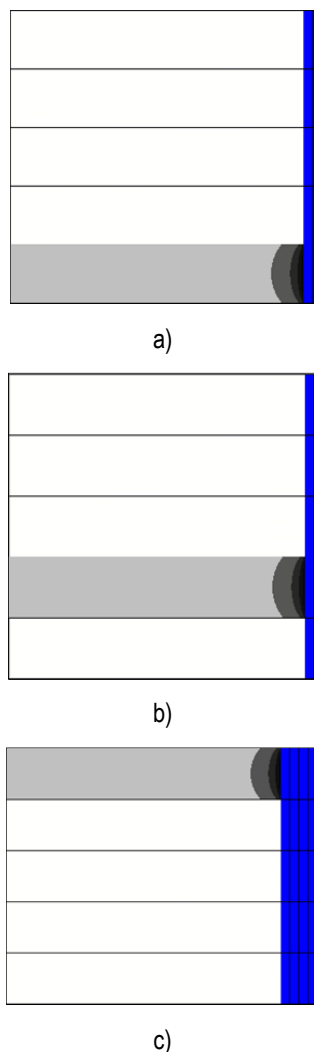


Fig. 6. "Running" magnetic field mode for a sectioned girdle coil

4. CONCLUSION

The proposed sectioning of the girdle coil (Fig. 5 and Fig. 6) ensures the improvement of the therapeutic results due to the periodic variation of the coil parameters (the switching of the individual sections). At the same time, each of the coil sections has a reduced inductance, and only one section is always included. Therefore, coil segmentation ensures that the inductor is energized with lower voltage. Each of the coil sections also has a reduced time constant, which greatly relieves the switching of the sections. Therefore, the proposed construction of girdle coil has certain advantages over the "classic" girdle coil. In fact this is the result of optimisation of application of girdle coil in magnetotherapy. Of course, it must be said that the magnetic wave can "run" only on the coil axis. This is a serious constraint in the process of changing the spatial configuration of the magnetic field in the therapy process.

8. ACKNOWLEDGMENTS

The authors would like to thank the Research and Development Sector at the Technical University of Sofia for the financial support.

REFERENCES

- [1] Dimitar Tz. Dimitrov, "Computer simulation of space configuration of low frequency magnetic field in magnetotherapy", Journal Electronics and Electrical Engineering, Lithuania, ISSN 1392-1215, No3/59, 2005, p.28-32.
- [2] Dimitar Tz. Dimitrov, "Improving the Performance of Program Package for 3D Simulation of Low Frequency Magnetic Field in Medical Therapy", Journal Electronics and Electrical Engineering, Lithuania, ISSN 1392-9631, 2007, No.1(73), p.69-72
- [3] Dimitar Tz. Dimitrov, "Visualization of a Low Frequency Magnetic Field, generated by Girdle Coil in Magnetotherapy", Journal "Electronics and Electrical Engineering", Litvania, ISSN 1392-1215, 2007, No.6(78), p.57-60.
- [4] Dimitar Tz. Dimitrov. Veska Georgieva, "Application of Apparatus for Magneto Therapy in Stomatology and Computer Treatment of X-ray Images before and after Therapy", Journal "Electronics and Electrical Engineering", Litvania, 2009, No.3(91), ISSN 1395-1215, p.39-43.
- [5] Dimitar Tz. Dimitrov, "Wireless module for distance measurement of patient's temperature in hospitals", Journal "Electronics and Electrical Engineering", Litvania, 2008, No.2(82), ISSN1395-1215, p.53-58.
- [6] Dimitar, Tz. Dimitrov, Simultaneously influence of magnetic and electrical field on the human body, Journal "Electronics and Electrical Engineering", Litvania, 2008, No.7(87), ISSN1395-1215, p.77-80.
- [7] Dimitar Tz. Dimitrov, Comparison between application of girdle coil and several local inductors in magnetotherapy, Proceedings of 14th International Conference "Communication, Electromagnetics and Medical Application CEMA'19", ISSN 1314-2100, Sofia, October 17th-19th, 2019, p.40-44.
- [8] Dimitar Tz. Dimitrov, Nikola Ralev, Signals and Systems for Electrosleep, Journal "Electronics and Electrical Engineering, ISSN 1392-1215, No.5(93), 2009, p.95-98.

ONE APPLICATION OF INFLUENCE OF LOW FREQUENCY MAGNETIC FIELD ON THE HEAD

Atanas Dimitrov, Sasho Guergov

Technical University of Sofia
1000 Sofia, 8, Kliment Ohridski str.

sguergov@tu-sofia.bg

Abstract

One description of theoretical and experimental investigation on influence of low frequency magnetic field on the head is the goal of present paper. The experimental investigation has been done using appropriate circuit. A comparison between direct electrical stimulation of neural tissue and stimulation of neural tissue by pulse magnetic field is done with respective conclusions and recommendations. An optimisation of parameters of used pulse magnetic field for stimulation is done, also.

1. INTRODUCTION

It's well known that the origin of the biomagnetic field is the electric activity of biological tissue [1,2,3]. This bioelectric activity produces an electric current in the volume conductor which induces the biomagnetic field. This correlation between bioelectric and biomagnetic phenomena is not limited in the process of generation of bioelectric and biomagnetic fields by the same bioelectric sources. This correlation also arises in the stimulation of biological tissue. Magnetic stimulation is a method for stimulating excitable tissue with an electric current induced by an external time-varying magnetic field [4,5,8]. It is important to note here that, as in the electric and magnetic detection of the bioelectric activity of excitable tissues, both the electric and the magnetic stimulation methods excite the membrane with electric current. The former does that directly, but the latter does it with the electric current which is induced within the volume conductor by the time-varying applied magnetic field. The reason for using a time-varying magnetic field to induce the stimulating current is, on the one hand, the different distribution of stimulating current and, on the other hand, the fact that the magnetic field penetrates unattenuated through such regions as the electrically insulating skull. This makes it possible to avoid a high density of stimulating current at the scalp in stimulating the central nervous system and thus avoid pain sensation. Also, no physical contact of the stimulating coil and the target tissue is required, unlike with electric stimulation.

2. DEVICE FOR INFLUENCE OF LOW FREQUENCY MAGNETIC FIELD ON THE HEAD

A magnetic stimulator includes a coil that is placed on the surface of the skin. To induce a current into the underlying tissue, a strong and rapidly changing magnetic field must be generated by the coil. In practice, this is generated by first charging a large capacitor to a high voltage and then discharging it with a thyristor switch through a coil. The principle of a magnetic stimulator is illustrated in Fig. 1.

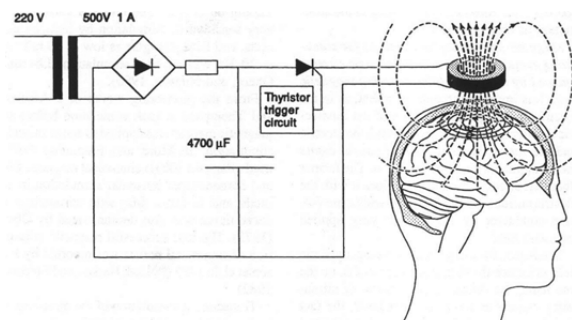


Fig. 1. Simple device for influence of low frequency magnetic field on the head

The magnitude of induced electromotive force "e" (emf) is proportional to the rate of change of current, di/dt and to the inductance of the coil L . The term di/dt depends on the speed with which the capacitors are discharged; the latter is increased by use of a fast solid-state switch (i.e., fast thyristor) and minimal wiring length. Inductance L is determined by the geometry and constitutive property of the medium. The principal factors for the coil system are the shape of the coil, the number of turns on the coil, and the permeability of the core.

3. SPACE CONFIGURATION OF CURRENT IN THE HEAD TISSUES AS RESULT OF INFLUENCE OF LOW FREQUENCY MAGNETIC FIELD

The magnetic permeability of biological tissue is approximately that of a vacuum. Therefore the tissue does not have any noticeable effect on the magnetic field itself. The rapidly changing field of the magnetic impulse induces electric current in the tissue, which produces the stimulation. Owing to the reciprocity theorem, the current density distribution of a magnetic stimulator is the same as the sensitivity distribution of such a magnetic detector having a similar construction. It's necessary to note that in the lead field theory, the reciprocal energization equals the application of stimulating energy. Two cases of application of single coil and quadrupolar coil configuration are described below

3.1. One inductor

The current distribution of a single inductor, producing a dipolar field, is presented on Fig. 2, which illustrates the isointensity lines and half-intensity volume for a inductor with a 50 mm radius. The distance of the inductor's plane from the head is 10mm. The concepts of isointensity line and half-intensity volume are reciprocal to the isosensitivity line and half-sensitivity volume [7,8]. Because of cylindrical symmetry the isointensity lines coincide with the magnetic field lines.

3.2. Quadrupolar Coil Configuration

The inductors can be equipped with cores of highly permeable material. One advantage of this arrangement is that the magnetic field that is produced is better focused in the desired location [6,7]. Constructing the permeable core in the form of the letter V results in the establishment of a quadrupolar magnetic field source. With a quadrupolar magnetic field, the stimulating electric current field in the tissue has a linear instead of circular form. In some applications the result is more effective stimulation. On the other hand, a quadrupolar field decreases as a function of distance faster than that of a dipolar coil. Therefore, the dipolar coil is more effective in stimulating objects that are located deeper within the tissue.

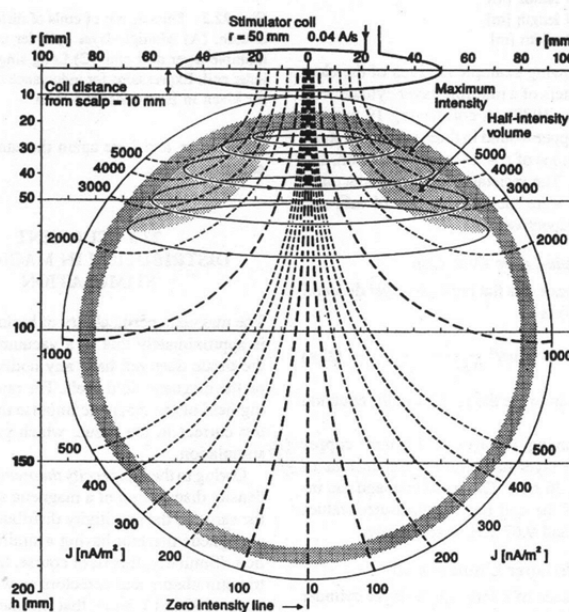


Fig. 2. Current's lines for an influence of low frequency magnetic field using small inductor

4. OPTIMISATION OF PARAMETERS OF SIMPLE DEVICE FOR INFLUENCE OF LOW FREQUENCY MAGNETIC FIELD ON THE HEAD.

The experimental device (Fig.1) has a capacitor construction equaling a capacitance of $4760 \mu F$. This was charged to 90-260 V and then discharged by thyristor through the stimulating coil. The result was a magnetic field pulse of 0.1-0.2 T, 5 mm away from the coil. The length of the magnetic field pulse was of the order of $150-300 \mu s$. The effectiveness of the stimulator with respect to energy transfer is proportional to the square root of the magnetic energy stored in the inductor when the current in the inductor reaches its maximum value [5,6]. A simple model of a nerve fiber is to regard each node as a leaky capacitor that has to be charged. Measurements with electrical stimulation indicate that the time constant of this leaky capacitor is of the order of $150-300 \mu s$. Therefore, for effective stimulation the current pulse into the node should be shorter than this. For a short pulse in the coil less energy is required, but obviously there is a lower limit too.

5. INFLUENCE OF LOW FREQUENCY MAGNETIC FIELD ON EXCITABLE TISSUE

The actual stimulation of excitable tissue by a time-varying magnetic field results from the flow of induced current across membranes. Without such flow a depolarization is not produced and excitation cannot result. Unfortunately, one cannot examine

question in a general sense but rather must look at specific geometries and structures. To date this has been done only for a single nerve fiber in a uniform conducting medium with a stimulating coil whose plane is parallel to the fiber. In the model examined by Roth and Basser, the nerve is assumed to be unmyelinated, infinite in extent, and lying in a uniform unbounded conducting medium, the membrane described by Hodgkin-Huxley equations. The transmembrane voltage V_m is shown to satisfy the equation (1):

$$\lambda^2 \frac{\partial^2 V_m}{\partial x^2} - V_m = \tau \frac{\partial V_m}{\partial t} + \lambda^2 \frac{\partial E_x}{\partial x} \quad (1)$$

where:

V_m is transmembrane voltage;

λ is the membrane space constant;

τ is the membrane time constant;

x is the orientation of the fiber.

E_x is x – component of the magnetically induced electric intensity (proportional to the x component of induced current density)

It is interesting that it is the axial derivative of this field that is the driving force for an induced voltage. For a uniform system in which end effects can be ignored, excitation will arise near the site of maximum changing current and not maximum current itself. In the experimental investigation the coil lies in the xy plane with its center at $x = 0, y = 0$, while the fiber is parallel to the x axis and at $y = 2,5\text{cm}$ and $z = 1,0\text{cm}$. They consider a coil with radius of 2.5 cm wound from 30 turns of wire of 1.0 mm radius. The coil, located at a distance of 1.0 cm from the fiber, is a constituent of an RLC circuit and the time variation is that resulting from a voltage step input. Assuming $C = 200\mu\text{F}$ and $R = 3\Omega$ an overdamped current waveform results. From the resulting stimulation it is found that excitation results at $x = 2.0$ cm (or 2.0 cm, depending on the direction of the magnetic field) which corresponds to the position of maximum $\partial E_x / \partial x$. The threshold applied voltage for excitation is determined to be 30 V. (This results in a peak coil current of around 10 A.) These design conditions could be readily realized.

Stimulators with short risetimes ($< 60\mu\text{s}$) need only half the stored energy of those with longer risetimes ($> 180\mu\text{s}$). The use of a variable field risetime also

enables membrane time constant to be measured and this may contain useful diagnostic information.

6. CONCLUSION

It's possible to do the next conclusions after theoretical and experimental investigations described above:

1. The low frequency pulse magnetic field can be applied for nervous stimulation either centrally or peripherally.
2. The main benefit of application of low frequency magnetic field for influence on the head is that the stimulating current density is not concentrated at the skin, as in electric stimulation, but is more equally distributed within the tissue. This is true especially in transcranial magnetic stimulation of the brain, where the high electric resistivity of the skull does not have any effect on the distribution of the stimulating current.
3. An important advantage of described method is that the stimulator does not have direct skin contact. This is a benefit in the sterile operation theater environment. It may be predicted that the magnetic stimulation can be applied particularly to the stimulation of cortical areas, because in electric stimulation it is difficult to produce concentrated stimulating current density distributions in the cortical region and to avoid high current densities on the scalp.

7. APPENDIX AND ACKNOWLEDGMENTS

The authors would like to thank the Research and Development Sector at the Technical University of Sofia for the financial support.

REFERENCES

- [1] Dimitar Tz. Dimitrov, "Computer simulation of space configuration of low frequency magnetic field in magnetotherapy", Journal Electronics and Electrical Engineering, Lithuania, ISSN 1392 – 1215, No3/59, 2005,p.28-32
- [2] Dimitar Tz. Dimitrov, "Improving the Performance of Program Package for 3D Simulation of Low Frequency Magnetic Field in Medical Therapy" Journal Electronics and Electrical Engineering, Lithuania, ISSN 1392-9631, 2007, No.1(73), p.69-72
- [3] Dimitar Tz. Dimitrov, "Visualization of a Low Frequency Magnetic Field, generated by Girdle Coil in Magnetothe-

- rapy", Journal "Electronics and Electrical Engineering", Litvania, ISSN 1392-1215, 2007, No.6(78), p.57-60
- [4] Dimitar Tz. Dimitrov, Veska Georgieva, "Application of Apparatus for Magneto Therapy in Stomatology and Computer Treatment of X-ray Images before and after Therapy", Journal "Electronics and Electrical Engineering", Litvania, 2009, No.3(91), ISSN1395-1215, pp.39-43
- [5] Dimitar Tz. Dimitrov, "Wireless module for distance measurement of patient's temperature in hospitals", Journal "Electronics and Electrical Engineering", Litvania, 2008, No.2(82), ISSN1395-1215, p.53-58
- [6] Dimitar, Tz. Dimitrov, Simultaneously influence of magnetic and electrical field on the human body, Journal "Electronics and Electrical Engineering", Litvania, 2008, No.7(87), ISSN1395-1215, p.77-80
- [7] Dimitar Tz. Dimitrov, Comparison between application of girdle coil and several local inductors in magnetotherapy, Proceedings of 14th International Conference "Communication, Electromagnetics and Medical Application CEMA'19", ISSN 1314-2100, Sofia, October 17th-19th, 2019, p.40-44
- [8] Dimitar Tz. Dimitrov, Nikola Ralev, Signals and Systems for Electrosleep, journal "Electronics and Electrical Engineering, ISSN 1392-1215, No.5(93), 2009, p.95-98.

AUTHOR INDEX

ALI, R. N.	10
AMPILOVA, N.	27,32,36
ANDREEV, E.	17
ANGELOVA, M.	14
BONEV, B.	46
DIMITROV, A.	72,76
DIMITROV, D.	68
DIMITROV, K.	14
DRAGANOV, I.	52
FRANGOS, P.	27,32
GEORGIEVA-TRIFONOVA, T.	58
GEORGIEVA, V.	22
GUERGOV, S.	72,76
IANTOVICS, B.	22
JASSIM, J. M.	10
JASSIM, K. M.	10
JAWAD, M. K.	10
KALLITSIS, E.	27
KIRECHEV, A.	63
KOTOPOULIS, A.	27,32
MANOLOVA, A.	52
MIRONOV, R.	52
MURENIN, I.	36
NESHOV, N.	52
NIKOLOVA, M.	17
PETROV, P.	22
PLESHKOVA, S.	63
POURAIMIS, G.	27,32
RADEVA, V.	17
SHARBA, A. B.	10
SHOPOV, A.	46
SIMEONOV, I.	58
SIRKOVA, I.	1,6
SYASKO, M.	41
SOLOVIEV, I.	27,32,41
STOYNOVA, A.	46
TRIFONOV, T.	58
VALYUKOV, S.	14